NZE 23-(EQC 1995/197)

Seismotectonics of the Arthur's Pass earthquake of 18 June 1994

R Robinson, R E Abercrombie, T H Webb, P J McGinty, T Arnadottir, J J Mori, R J Beavan, M Reyners, IGNS

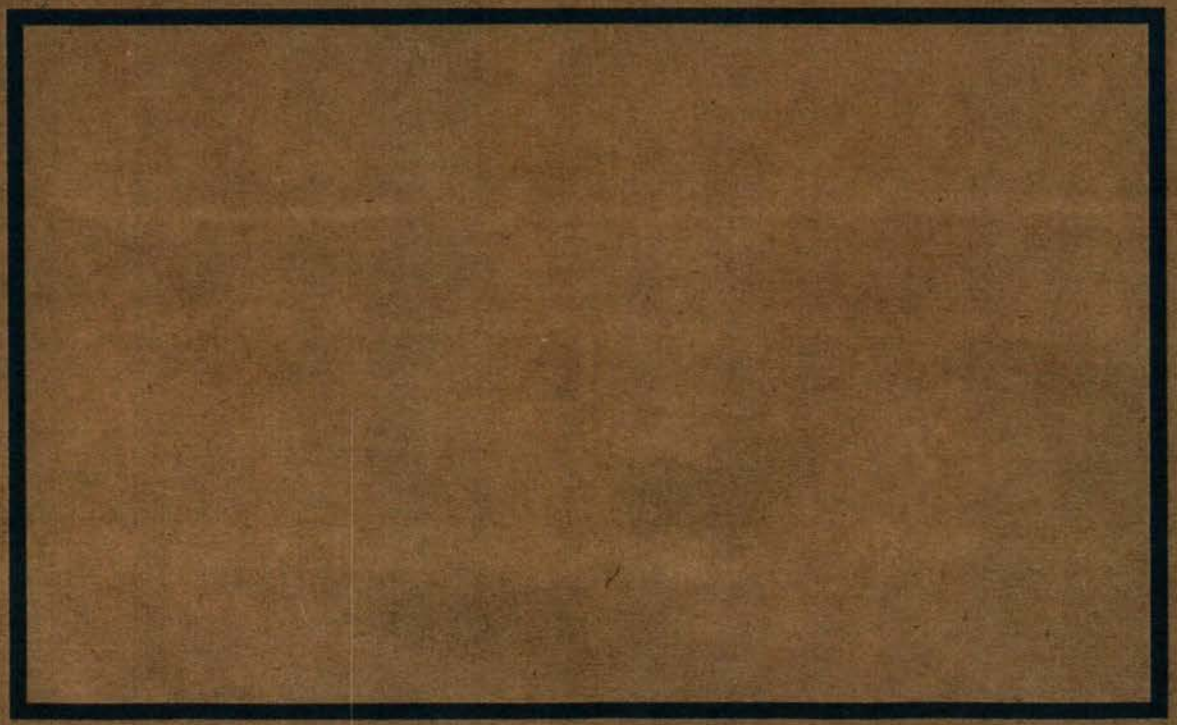

Client Report 42655B

Seismotectonics of the Arthur's Pass Earthquake of 18 June 1994

Prepared for
Earthquake Commission
Research Foundation

by

R Robinson
R E Abercrombie
T H Webb
P J McGinty
T Arnadottir
J J Mori
R J Beavan
M Reyners

July 1998

Institute of
GEOLOGICAL
& NUCLEAR
SCIENCES
Limited

Institute of
GEOLOGICAL
& NUCLEAR
SCIENCES
Limited

SEISMOTECTONICS OF THE ARTHUR'S PASS EARTHQUAKE OF 18 JUNE 1994

Prepared for
THE EARTHQUAKE COMMISION RESEARCH FOUNDATION

By

R. Robinson, R. E. Abercrombie, T. H. Webb, P.J. McGinty,
T. Arnadottir, J. J. Mori, R. J. Beavan and M. Reyners.

July 1998

A STUDY FUNDED BY THE EARTHQUAKE COMMISSION
[RESEARCH PROJECT 95/197] AND THE PUBLIC GOOD SCIENCE FUND

Client Report 42655B

Gracefield Research Centre, 69 Gracefield Road, PO Box 30368, Lower Hutt, New Zealand, Telephone: +64-4-570 1444, Facsimile: +64-4-570 4600

RECOMMENDED BIBLIOGRAPHIC REFERENCE

Robinson, R., Abercrombie, R. E., Webb, T. H., McGinty, P.J., Arnadottir, T., Mori, J. J., Beavan, R. J. and Reyners, M., 1998: Seismotectonics of the Arthurs Pass earthquake of 18 June, 1994. *GNS Client Report 42655B*, July 1998.

TECHNICAL ABSTRACT

The M_W 6.7 Arthur's Pass earthquake of 18 June 1994 is the largest in a recent sequence of earthquakes in the central South Island. Routine methods of obtaining the faulting orientation of this earthquake proved contradictory, so we have used a range of data and techniques to determine the orientation and nature of slip in this event. No surface faulting was observed so that could not be used to define a fault plane. Modelling of the teleseismic mainshock body-waves resulted in a shallow reverse mechanism, striking NE-SW. Both the body-wave modelling and modelling of regional broadband data indicate a simple source process of ~7.5 s duration. The stress drop calculated for the earthquake (9-12 MPa) is high in comparison with other events, even reverse ones.

Aftershocks have been relocated using both 1-D and 3-D velocity inversions to improve location accuracy. The depth range of the aftershocks (1 to 10 km) is in good agreement with the preferred mainshock centroid depth (5 km). The aftershock sequence is typical of a shallow New Zealand earthquake in both size and duration, but aftershocks exhibit a complex spatial distribution. The best located aftershocks define a structure extending SW of the mainshock hypocentre, and dipping towards the NW. This is interpreted to be the fault plane, and its surface projection is within estimated uncertainties of the Red Rock fault. However, aftershocks extend 12 km NNW and 30 km SSE of this fault plane. Most of the $M \geq 5$ aftershocks, including the two largest (M6.0 and 5.7), cluster near the Harper fault at the southern end of the aftershock zone and are consistent with strike-slip motion on this fault or a conjugate. Motion in these southern aftershocks is included in the surface displacements obtained from a GPS resurvey ~2 weeks after the mainshock. Forward modelling of the GPS data suggests that a predominantly reverse slip mainshock, combined with strike-slip faulting in the south, is able to match the observed displacements.

We have used several methods to infer the regional stress field in the region, including geodetic results, earthquake mechanisms, and inversion of P-wave polarity data for the stress tensor orientation. The inversion method is new, and does not require the focal mechanisms of the events used. It also incorporates the Coulomb failure criterion. All results point to a stress field favouring strike-slip faulting, not thrusting, with near horizontal $\sigma 1$ and $\sigma 3$ principal axes striking at 298° and 28°. The fault plane of the mainshock is not well oriented for reverse slip in this stress regime. Using dislocation theory we calculate the stress induced by the Arthur's Pass earthquake, and its largest aftershock (a strike-slip event), and add this to the regional field. Assuming that off-fault aftershocks will occur where the Coulomb Failure Stress (CFS) on optimally oriented planes is highest, we find a fair correspondence between the aftershock distribution and regions of high CFS. However, there are regions of high CFS that are devoid of aftershocks. It appears that earthquake slip in this region of oblique (19°) plate convergence is, as observed elsewhere, partitioned into components parallel and perpendicular to the plate margin. Most of the slip is parallel, as occurs on the nearby dextral Alpine Fault, the boundary between the Pacific and Australian plates. But occasional reverse events, such as the Arthur's Pass earthquake, account for at least some of the perpendicular component of slip, and the uplift that produced the Southern Alps. The M_W 6.2 Cass earthquake of 1995, 30 km to the east, occurred near a peak in the induced CFS for a fault with its observed mechanism (a mix of reverse and strike-slip motion) and so can be classed as a triggered earthquake.

NON-TECHNICAL ABSTRACT

The magnitude 6.7 Arthur's Pass earthquake of 18 June 1994 was the largest shock to occur in the Southern Alps for 65 years. We have used data recorded by the New Zealand National Seismograph Network, overseas seismograph stations, and sixteen portable seismographs installed in the Arthur's Pass region immediately after the earthquake to determine the type of faulting which took place during the mainshock. No surface faulting was observed for this earthquake. The seismological data indicates that the earthquake mainly involved thrusting on a fault oriented northeast-southwest. Such thrusting is broadly consistent with ground movements resulting from the earthquake measured using Global Positioning System (GPS) satellite receivers. This event is thus taking up the convergent component of the relative motion between the Pacific and Australian plates in the central South Island - events such as this contribute to the uplift that has produced the Southern Alps. The thrusting mechanism for the earthquake determined in this study differs significantly from the mechanisms determined by overseas agencies soon after the event. For at least two years following the event it was not known whether it was a thrust or strike-slip event, let alone on which fault it occurred. This fact is worth noting at a time when the determination of the focal mechanisms of moderate sized earthquakes globally is considered fairly routine.

Definition of the fault plane of the Arthur's Pass earthquake was rendered difficult because of the unusual distribution of aftershocks of the event. These extend 12 km north-northwest and 30 km south-southeast of the actual fault plane. We have sought to explain this unusual distribution of aftershocks by calculating the changes in the stress field in the region caused by fault slip during the mainshock and the largest aftershock (a magnitude 6.0 event near the Harper fault). Such stress changes can bring some regions closer to failure (leading to more aftershocks), and move other regions away from failure. To calculate these stress changes we first determine the regional stress field using geodetic results, earthquake mechanisms and a new method which uses P-wave polarity data. All results point to a stress field favouring strike-slip faulting, not thrusting. Thus the thrusting which occurred in the Arthur's Pass earthquake may be relatively rare. When stress changes caused by the mainshock and largest aftershock are added to the regional stress field, we find a fair correspondence between the aftershock distribution and regions where failure stress has increased. In particular, the subsequent magnitude 6.2 Cass earthquake of 24 November 1995, 30 km to the east, appears to have been triggered by the Arthur's Pass earthquake.

CONTENTS

INTRODUCTION

The M_W 6.7 Arthur's Pass earthquake of 18 June 1994 was the largest shock to occur in the Southern Alps for 65 years. The event thus has important implications for long-term seismic hazard in the region, and in particular the seismic hazard of Christchurch. Even though the earthquake was located 105 km to the northwest, most of the $5.3 million in damage claims to EQC were for minor damage to property in the Christchurch area.

The wide range of data recorded on the earthquake provides a unique opportunity for study of its source mechanism. The event fortuitously occurred within a network of geodetic stations that had been surveyed in 1992 using GPS receivers. Reoccupation of 32 of these stations in the three weeks following the earthquake indicates horizontal offsets of up to 0.5 metres. The entire network was reobserved in 1995, and again in 1997. In addition, 16 portable seismographs were installed in the aftershock region immediately after the event, to supplement data from the New Zealand National Seismograph Network. These provide excellent control on the locations and focal mechanisms of the numerous aftershocks recorded (over 13,000 aftershocks occurred in the first week following the mainshock).

This study aims to reconcile these seismological and geodetic data into a self-consistent model of the mainshock rupture and aftershock distribution. Our results have been summarised in the following two companion papers which are to be submitted to the *Journal of Geophysical Research.* The first deals with the determination of the orientation and nature of slip during the mainshock, while the second investigates the unusual aftershock distribution and its relation to the regional and induced stress fields. Also included as an appendix is a progress report on analysis of the GPS data produced by Dr Thora Arnadottir in December 1995, prior to her return to the United States. While this analysis has been superseded by inclusion of subsequent GPS data recorded in 1997 and a better determined aftershock distribution (see paper I), this report gives an indication of the range of models tested in trying to reconcile the seismological and geodetic data.

The Enigma of the Arthur's Pass, New Zealand, Earthquake 1: Reconciling a Variety of Data for an Unusual Earthquake Sequence

Rachel E. Abercrombie, T. H. Webb, R. Robinson, P. J. McGinty, J. J. Mori, and R. J. Beavan

Institute of Geological and Nuclear Sciences

Lower Hutt

email: R.Abercrombie@gns.cri.nz

25 June 1998

For submission to the Journal of Geophysical Research

ABSTRACT

The 1994 Arthur's Pass earthquake (M_w6.7) is the largest in a recent sequence of earthquakes in the central South Island, New Zealand. Routine methods of obtaining the faulting orientation of this earthquake proved contradictory, and despite field reconnaisance no surface faulting was observed and so could not be used to define a fault plane. Therefore we have used a range of data and techniques to determine the orientation and nature of the slip in this event. Modeling of the teleseismic mainshock body-waves resulted in a shallow reverse mechanism, striking NE-SW. There was no evidence of source complexity, or of late subevents. An independent estimate of the source time function was obtained from regional broadband data, using the largest aftershocks as empirical Green's functions. The simple source process was confirmed and the duration (~7.5 s) agreed well with the body-wave modeling. The preferred solution had a centroid depth of 5 km, M_0=1.3×10^{19} Nm, and a strike, dip and rake of 221°, 47°, 112° respectively. The stress drop inferred from this source duration is in the range 9–12 Mpa, somewhat high in comparison with other events wordwide, but not exceedingly so.

We relocated the aftershocks using both 1-D and 3-D velocity inversions to improve the location accuracy. The depth range of the aftershocks (1 to 10 km) was in good agreement with the preferred mainshock depth. The aftershock sequence was typical of a shallow New Zealand earthquake in both size and duration, but exhibited a complex spatial distribution. The aftershock zone was elongated approximately NNW-SSE, perpendicular to the predominant surface fault orientation in the region, but appeared to consist of a series of lineations, parallel to the faults, principally to the south of the mainshock. The best located aftershocks defined a structure extending SW from the mainshock hypocenter, and dipping towards the NW. This was interpreted to be the fault plane, and its surface projection was within estimated uncertainties of the Red Rock fault. This structure, and the Harper fault to the south, appeared to act as boundaries to the aftershock zones trending NNW-SSE.

Most of the $M_L \geq 5$ aftershocks, including the two largest (M_L6.1 and 5.7), clustered near the Harper fault and were consistent with strike-slip motion on this fault or a conjugate. Motion in these southern aftershocks was included in the surface displacements obtained from a GPS resurvey ~2 weeks after the mainshock. Forward modeling of the GPS data suggested that a predominantly reverse slip mainshock, combined with strike-slip faulting in the south was able to match the observed displacements.

The level of seismic hazard in the central South Island must be higher than earlier estimates because shallow crustal earthquakes appear to be more common than previously thought.. The predominantly reverse mechanism for this event is consistent with slip partitioning along the length of the continental collision zone in the South Island.

1. INTRODUCTION

The June 18, 1994 Arthur's Pass earthquake (moment magnitude, M_w, 6.7) was the largest earthquake to occur in the central South Island of New Zealand for 65 years (Fig. 1). The remote location of the earthquake in the Southern Alps, about 10 km from the small township of Arthur's Pass, meant that the structural damage caused was small for a shallow crustal

earthquake of this size. A total of about 70 landslides attributed to the Arthur's Pass earthquake have been mapped, and rock falls blocked the trans-Alpine State Highway 73 for a week (Hancox et al., 1997). An eye witness report from hikers in the epicentral region describes large boulders falling, broken vegetation including snapped trees, and items within a mountain hut being thrown to the floor (Gordon, 1994). The New Zealand Earthquake Commission received $US 3.2 million in damage claims following the earthquake, principally from the city of Christchurch 120 km to the south east.

The epicenter of the Arthur's Pass earthquake is about 25 km SE of the Alpine fault — the primarily strike-slip fault forming the boundary between the Australian and Pacific plates through the South Island (Fig. 1). To the north of the epicentral region, the Alpine fault divides into a number of splays (the Marlborough fault system). The central and northern South Island are dominated by NE-SW striking strike-slip faults, but the oblique convergence of the two plates, and the ongoing uplift of the Southern Alps imply that reverse faulting earthquakes should also be expected. Robinson and McGinty (this volume) discuss the implications of the Arthur's Pass earthquake for the regional tectonics and stress field in more detail.

Since 1881 there have been seven earthquakes of M_L6 and greater in the Arthur's Pass region (Fig. 2). The largest of these was a M_w7.3 strike-slip earthquake in 1888 which produced 30 km of surface rupture on the Hope fault (Cowan 1991). The 1929 Arthur's Pass earthquake (M_w7.0) is also thought to have been a strike-slip event, on the Kakapo fault (Yang, 1992; Doser et al., 1998). The 1946 Lake Coleridge event has been modelled by Doser et al. (1998), who obtained a strike-slip solution with a nodal plane consistent with the strike of nearby faults. More recently, the 1994 Arthur's Pass earthquake forms the second event in a sequence starting with the March 30, 1992 Wilberforce River earthquake (M_L5.2). This earthquake was unfortunately too small to obtain a focal mechanism from body-wave modeling, and the New Zealand National Seismic Network (NZNSN) is too sparse to determine a fault plane solution from the first motions. The Arthur's Pass earthquake had an extensive aftershock sequence, including one M_L6.1 and thirteen other $M_L \geq 5.0$ events. On May 29, 1995 a M_L 6.0 earthquake occurred less than 10 km east of the Arthur's Pass mainshock, but away from the aftershock sequence. It was too poorly recorded to determine a focal mechanism. The last event in this sequence to date, was the November 11, 1995 Cass earthquake (M_w6.2), located 30 km to the east of the Arthur's Pass mainshock. This earthquake and its aftershocks were well recorded by a temporary network deployed in the South Island at the time. It was a shallow, oblique reverse earthquake on a N-S striking fault, and produced no surface rupture (Gledhill et al., 1998).

The initial attempts to determine a focal mechanism, and hence a fault plane, for the Arthur's Pass earthquake were contradictory. Both Harvard University and the NEIC performed routine Centroid Moment Tensor (CMT) solutions. J. Zhang (pers. comm., 1994) also performed a similar CMT inversion using an improved regional velocity structure. The three mechanisms range from oblique strike-slip (Harvard) to almost pure reverse (NEIC), and do not have any nodal planes in common (Fig. 3). All the inversions require a fixed depth for such a shallow earthquake. Initial body-wave inversion for the source mechanism and depth of the Arthur's Pass earthquake (Abercrombie et al. 1996b) favored a very shallow depth (3 km) and a pure reverse mechanism, striking NE-SW (Fig. 3). This is inconsistent with any of

the CMT solutions, and also such a shallow centroid depth seemed unlikely given the absence of substantial surface rupture.

The initial aftershock locations (Robinson et al. 1995) show a complex distribution with some indication of activity on NE-striking structures, as well as the main NNW trending zone which broadens to the north. Robinson et al. (1995) note that the main NNW trend of the aftershocks is consistent with one of the nodal planes of the Harvard CMT solution, and so they suggest that the Arthur's Pass earthquake may have involved strike-slip with a reverse component on a fault striking NNW and dipping steeply to the SW. This hypothesis, however, does not fit either of the other two CMT solutions or the body-wave modeling result.

Field surveys of the broad aftershock zone, both immediately after the earthquake and the following summer, failed to find any evidence of surface rupture (Van Dissen and Berryman, 1995). The mountainous terrain and the large area affected mean that some rupture could have been missed, but it would have to be fairly insignificant (R. Van Dissen, pers. comm. 1997).

The Arthur's Pass earthquake occurred within a network of geodetic stations surveyed in December 1992 using GPS receivers. These sites were reoccupied following the earthquake in 1994 and 1995 and relative displacements of up to 0.5 m were observed (Arnadottir et al., 1995). Preliminary analysis of these data found them impossible to model with uniform slip on a single fault. A reasonable fit to the data was possible with a NNW trending fault divided into two independently slipping parts (Arnadottir et al., 1995). Both parts were mainly strike-slip, but there was significant reverse motion in the northern part.

These seemingly contradictory observations suggest that the Arthur's Pass earthquake may have had a complex source, perhaps with separate subevents of different slip orientation. Alternatively, the trade-offs between depth, duration and dip-slip component in modeling shallow earthquakes teleseismically may be causing the discrepancies between the different mechanisms. The GPS data would not be affected by this, but as the observations are not continuous, they represent the cumulative displacement in the mainshock and aftershocks. Hence large aftershocks and possibly aseismic slip may be affecting the data that are being modeled.

For at least two years following the Arthur's Pass earthquake it was unknown whether it was a reverse or strike-slip event, let alone on which fault it occurred. This fact is worth noting at a time when the focal mechanism determination of moderate sized earthquakes globally is considered fairly routine. The aim of the present paper is to present detailed seismic observations and analysis of the Arthur's Pass earthquake and aftershocks, in order to obtain a source mechanism for the earthquake which is consistent with all the available data, including the GPS observations. First we describe the analysis of the mainshock by teleseismic body-wave modeling and using empirical Green's functions at regional distances. Secondly we relocate the aftershocks using a 1-D and then a 3-D velocity inversion to improve the hypocenter locations. We then combine observations of the distribution of the well located aftershocks with the mainshock modeling results to determine a rupture scenario for the Arthur's Pass earthquake and its aftershock sequence. We then investigate whether this is compatible with the GPS observations and also other geological and geophysical data. Finally we discuss the implications for seismic hazard and the regional tectonics.

2. BODY-WAVE MODELING OF THE MAINSHOCK

To determine the source parameters using teleseismic data we used McCaffrey and Abers' (1988) version of Nabelek's (1984) inversion procedure, which minimizes the misfit between the recorded and synthetic waveforms. We used P and SH long-period waveforms recorded at Global Seismograph Network (GSN) stations at distances between 30° and 80°. To improve the signal to noise ratio the long-period traces were band-pass filtered between 5 and 70 seconds.

Synthetic seismograms were generated by combining direct (P or S) and reflected (pP and sP, or sS) phases from a point source (Langston and Helmberger, 1975). The source structure was a layer over a halfspace, with velocities derived from the 1-D velocity inversion of the aftershocks (see Table 2, Section 5.1). Receiver functions were calculated for a halfspace. Amplitudes were adjusted for geometrical spreading and for attenuation using Futterman's (1962) t* operator, with t*=1 s for P and t*=4 s for SH. Station coverage for the New Zealand region is poor to the east because there are few island stations in the Pacific Ocean. To compensate for this, seismograms were weighted according to azimuthal density (McCaffrey and Abers, 1988). The inversion process (Nabelek, 1984) was then used to adjust the strike, dip, rake, depth and source time function, the latter being described by a series of overlapping triangles of prescribed number and duration. Iterations were continued until a minimum misfit between data and synthetics was found. We used the Harvard Centroid Moment Tensor (CMT) solution (Dziewonski et al., 1981) as a starting solution. We assessed the degree of constraint on the derived source parameters by perturbing each of the strike, dip, rake, second strike, and depth in turn, and repeating the inversion with the perturbed parameter constrained. Our estimated uncertainty for each parameter was the value where the waveform fit deteriorated noticeably compared to the noise in the seismogram.

The waveform inversion converged rapidly to a predominantly reverse mechanism that was well-constrained and fitted the data well. Details are shown in Fig. 4 and Table 1. Stations not used in the inversion due to poor signal-to-noise ratio or being too close (but shown to demonstrate matched first motions) are marked with an asterisk. A very shallow centroid depth of 3.6 km was found by the inversion, but waveform fits were equally acceptable for depths from 3 to 5 km. For an event of this size there is a strong trade-off in the inversion between centroid depth and the duration of the source time function. This was resolved by an independent determination of duration using empirical Green's functions (see below), which suggested that a 5 km depth was the most appropriate. The moment magnitude of 6.7 was the same as both the local magnitude and Harvard CMT M_w value. Regional first motions were examined to try and confirm the body-wave solution. The body-wave solution has the best fit to the first motions with the only polarity violations being due to stations near nodal planes that would fit if the velocity model was adjusted slightly.

The predominantly reverse body-wave solution differs significantly from the CMT solutions obtained by others. In Fig. 5 we show comparisons of waveforms from selected stations for various solutions. Due to the good constraint on the mechanism, the minimum misfit solution is clearly a better fit to the 5 to 70 second body-wave data than any of the CMTs. Solutions with a large component of strike-slip cannot fit the data because many P wave amplitudes are then too small compared to SH waves. This is in contrast to the largest aftershock, for which

a strike-slip solution was obtained (see below). For shallow earthquakes, the CMT method has difficulty resolving the Mxz and Myz moment tensor elements that represent vertical dip-slip (Scott and Kanamori, 1985). There is thus a strong trade-off between depth and the amount of dip-slip for very shallow earthquakes such as this event, which may explain why the CMT solutions, which have depths of at least 15 km, have too small a dip-slip component.

The source time function obtained from the inversion (Fig. 4) was simple, with no indication of significant sub-events. This was consistent with nearby strong-motion data (Cousins, pers. comm., 1998), which showed no aftershocks within 1½ minutes of the mainshock. The duration of the source time function was about 8 s for 3 to 5 km depth solutions, but shorter than that at greater depths.

3. EMPIRICAL GREEN'S FUNCTION ANALYSIS OF THE MAINSHOCK

In order to resolve the inevitable trade-off between source duration, focal mechanism and depth for moderate sized, shallow earthquakes such as Arthur's Pass, an independent estimate of either the depth or duration is required. We therefore used the empirical Green's function technique to obtain an alternative estimate of the shape and duration of the source time function. This method uses the seismogram of a smaller earthquake, located close to and recorded at the same site as the main event as an empirical estimate of the propagation path effects. When the seismogram of the smaller earthquake is deconvolved from that of the main event, the common path effects are removed, resulting in an estimate of the source time function of the main event.

The empirical Green's function technique has been used successfully to determine the source mechanisms of earthquakes over a wide magnitude range using seismograms recorded at local, regional and teleseismic distances. If sufficient recordings are available then the deconvolved source time functions can be inverted to determine the fault plane and slip distribution in the earthquake. Mori and Hartzell (1990) used local P waves to extract the source time function of a M_L4.6 earthquake. Dreger (1994) and Dreger et al. (1995) used local and regional broadband seismograms to determine the slip distributions of M_w6–7 earthquakes, and Ammon et al. (1994) have extended the technique to use teleseismic recordings of large earthquakes. The method has also been used in New Zealand to obtain an estimate of the source duration of the 1995 Cass earthquake (Gledhill et al. 1998). The three basic assumptions of the method are that the smaller, empirical Green's function event is co-located with the main event (so that the propagation effects are identical for both earthquakes), that both events have the same focal mechanisms and that the empirical Green's function event is small enough that its source time function can be considered to be a delta function in comparison to the duration of the main earthquake.

The GSN station SNZO (in Wellington) was the nearest broadband instrument to the Arthur's Pass earthquake, at a distance of 300 km and an azimuth of 52°. The largest aftershocks were approximately an order of magnitude smaller than the mainshock and so were of sufficiently short duration to be used as empirical Green's functions. In order to obtain a reliable estimate of the source time function we used each of the four largest aftershocks as empirical Green's functions (Table 1). These four aftershocks were located about 15 km from the mainshock hypocenter, but this distance was small in comparison with the distance to SNZO, and the

difference in propagation path can be considered insignificant. The focal mechanisms of these aftershocks were not well constrained, but it is likely that they were predominantly strike-slip (previous section and section 5.4) — significantly different to that preferred for the mainshock. This mismatch would severely affect the amplitude of the resulting source time function, but would have a negligible effect on the shape or duration which are the parameters of interest. These departures from the assumptions of the empirical Green's function method would decrease the signal-to-noise ratio of the resulting source time function, but should not systematically bias the duration estimate.

We selected a range of time windows including the S and surface waves and increasing amounts of coda (120 - 260 s) from the vertical and SH components of the mainshock and the four aftershock SNZO records. The corresponding mainshock and aftershock pairs were then deconvolved using the method of Mori and Hartzell (1990). The seismograms and resulting source time function using the largest aftershock (M_L6.1) are shown in Fig. 6a as an example. The source time functions obtained from the different empirical Green's function events and different time windows are remarkably consistent, all consisting of a single simple pulse of 7 to 8 s duration (Fig. 7).

Variation in the source time function duration with azimuth is indicative of rupture directivity and so we applied the empirical Green's function technique to other available regional broadband recordings in Australia and the south Pacific. As these other sites are more distant, only the largest aftershock had sufficient signal to be used as an empirical Green's function event. We used longer time windows (500 s) at these sites to include the principal Love (SH) and Rayleigh (vertical) wave energy. The results for two of the nearest sites, TAU (17.6° epicentral distance) and NWAO (43°) in Australia are shown in Figs. 6b and 7. The source time function at TAU is very similar in duration to that at SNZO, but that at NWAO is longer. This difference cannot be the result of source directivity as the azimuths to TAU and NWAO were almost identical (262° and 265° respectively). Instead, it results from the attenuation along the longer paths limiting the bandwidth of the signal of the smaller event. The highest frequencies recorded above noise from the aftershock were 0.16 Hz and 0.95 Hz at TAU and NWAO respectively, corresponding to minimum resolvable durations of about 6 and 10 s. The other regional stations had similar or lower signal bandwidths than NWAO and so could not be used to resolve the duration of the moderate sized Arthur's Pass earthquake. The duration of the source time function obtained at TAU is also best considered a maximum estimate. The azimuth of SNZO (to the NE) is only 7° off the strike of the preferred fault plane, and TAU (to the WSW) is 33° off the strike in the opposite direction. The similar relative lengths and simple, single pulse shapes of the source time functions at these two stations imply that there was no strong source directivity along strike, nor separate sub-events. The rupture could not have propagated towards SNZO, but it is possible that slip propagated in the opposite direction, within the limits of resolution at TAU.

The duration of the source time function was thus found to be about 7.5 s in the empirical Green's function analysis. Comparison of the source time function determined at SNZO with those obtained at a range of fixed depths from the body-wave modeling enabled us to constrain the depth of the main energy release more accurately. Fig. 8 shows the source time function from SNZO and also the focal mechanisms and source time functions obtained from body-wave modeling at a range of depths between 3 and 12 km. The body-wave goodness of fit decreased with increasing depth, and by 6 km was significantly poor. The source time functions at depths between 3 and 6 km were consistent with that obtained at SNZO, and

those at greater depths were too short. We could thus constrain the depth of the main energy release to be less than 6 km on the basis of the source time function comparison. A depth of 5 km was preferred as this was the limiting depth for the body-wave analysis and was near the center of the aftershock depth range (see section 5). The lack of surface rupture also makes a very shallow centroid depth unlikely. The focal mechanism was therefore constrained to be predominantly reverse, on a plane striking approximately NE-SW, and dipping to either the NW or SE (Table 1). The fault plane and auxiliary plane cannot be distinguished using the available teleseismic and regional mainshock recordings. The simple shape of the source time function obtained at SNZO and also at TAU confirmed the result of the waveform inversion that the earthquake had a simple source with no major subevents.

4. BODY-WAVE MODELING OF THE LARGEST AFTERSHOCK

Only one aftershock in the sequence produced sufficiently large body waves to model. This is partly a reflection on the sparseness of good GSN stations in this part of the world at that time. This event (M_w=5.9, M_L=6.1) occurred on June 19, 1994 and was located near the Harper fault at the SSE end of the aftershock zone. Because the signal-to-noise ratio was poor, we filtered these data more heavily than was necessary for the mainshock, using a filter that effectively emulated a long-period WWSSN response. The velocity model used was the same as for the mainshock (Table 2). It is clear from the signal-to-noise ratio on the P and SH waves that this event has a larger SH to P amplitude ratio than the mainshock, indicating a larger strike-slip component in the mechanism. The results are shown in Fig. 9. Even the filtered P waves are poorly resolved, but the SH waves are clearer and have a good azimuthal coverage. SH waves recorded at stations KIP, RPN, and SPA, although plotted, were not used in the inversion because of the noise level. Travel time residuals for all P waves were less than 2 seconds, while SH residuals of up to 9 seconds were observed at SE azimuths (RPN, PMSA, SPA), consistent with the mainshock and the results of Anderson et al. (1993).

Constraint on the mechanism is reasonable (Table 1) considering the noisy P waves. The solution is within error of the Harvard CMT solution, but differs significantly from the USGS solution due to a greater dip on one nodal plane. Agreement with regional first motions is good, the only violation being at one regional station near a nodal plane.

5. AFTERSHOCK SEQUENCE

The Arthur's Pass earthquake sequence was recorded by NZNSN short period (1 Hz) EARSS seismographs (Gledhill et al., 1991). In addition, 16 portable seismographs were installed in the 5 days following the mainshock and recorded aftershocks until the first week of July 1994 (Fig. 10). One station (CASA) was left in until early August to maintain some depth control on continuing aftershocks. Earthquakes in New Zealand are routinely located using data from the NZNSN and any available temporary stations. Over 13,000 aftershocks were picked in the first week following the Arthur's Pass mainshock, of which over 6,000 could be located. These routine locations are relatively poor, however, as they use a single velocity structure without station terms for almost all of New Zealand, and so they do not resolve well the activated structures or help to distinguish the mainshock fault plane. The epicenters define an area elongated approximately NNW-SSE, with an almost bimodal distribution of large events, one group clustered around the mainshock in the northern half, and the other group to the south (Fig. 10). Previous studies in New Zealand (e.g. Robinson, 1994) and elsewhere

have demonstrated the value of relocating earthquakes using a seismic velocity model developed especially for the local region. We therefore relocated the aftershocks, first using a joint 1-D inversion for velocity structure, station terms, and hypocenters on a subset of the data, followed by a 1-D relocation of all data, and finally a 3-D inversion, to obtain more accurate hypocenters. We used these locations to investigate the structures activated by the sequence.

5.1 1-D Inversion

The 1-D velocity model (Table 2) was derived using the technique of iterative inversion of arrival-time data for both hypocenters and velocity parameters (Crosson, 1976). The specific implementation used is described in detail by Robinson (1986). The P/S velocity ratio was fixed to 1.73, but independent station terms for P and S were determined. The data were the P and S arrival times of 506 events during the time of most dense portable instrument deployment (22 June through 3 July) that were recorded by at least 6 portable stations and of magnitude 2.0 or more. Because of the depth range of the aftershocks, velocities below 15 km depth are constrained mostly by data from the 8 closest (65–240 km) NZNSN stations included in the inversion. In the actual inversion the three thin near surface layers shown in Table 2 were not included, but added later because the focal mechanism determination method used by Robinson and McGinty (this volume) makes use of P/S amplitude ratios. Inclusion of more realistic near surface layers makes that method more self-consistent when using ratios from different components of motion (Z, R, and T). The velocities in the first thick layer (1 to 5 km deep) were adjusted from the inversion result for a layer from 0 to 5 km depth so as to keep the vertical travel-time the same.

The velocity model is consistent with the local geology and with the crustal structure results of Davey et al. (1998) further to the south. The velocity for the underlying half-space, below 35 km depth, is low for the mantle, probably reflecting the deep crustal root under the Southern Alps. The station P and S terms for the portable stations are small (between -0.27 and +0.20 seconds for P) but tend to increase to the SE. The terms for the NZNSN stations are bigger, from -1.08 to +0.5 seconds, indicating that locations without using station terms could have large errors.

Using the 1-D velocity model, all Arthur's Pass aftershocks were relocated using standard procedures. Magnitudes were also recalculated. All relocated events were assigned a quality, A through E, making use of criteria based on number of phases, distance to the nearest station, RMS travel-time residual, and formal location error (see Reyners et al., 1997, for details). Quality A events, plus those with $M_L \geq 5.0$, are plotted in Fig. 11a. These events should have sufficient location accuracy to be used in focal mechanism determinations; lower quality events have less control on depth. All aftershocks before the installation of the portable instruments have C or lower quality because of the relatively large distance to the nearest station.

5.2 Relocations with 3-D velocity model

To improve the accuracy of the earthquake hypocenters, we determined a three-dimensional (3-D) P-wave velocity model in the aftershock region for use in relocating the events. The derived velocity model and associated stations terms improve the travel time calculations, especially for the heterogeneous paths to the portable stations in the aftershock region. We

used the computer program by Eberhart-Phillips (1993) which simultaneously solves for hypocenters, velocities at nodes of a grid, and station terms. Smooth velocity gradients between the node points are used for ray tracing between the events and stations. For the Arthur's Pass region a 7 x 9 grid with 5 km spacing was centered on the aftershock distribution with 7 depth layers at 0, 1, 3, 5, 10 15, and 30 km. To determine the velocity structure, we used 588 well-distributed earthquakes that had 10 or more P arrivals and a starting 1-D velocity model described in the previous section. With the 3-D model there was an 80% variance reduction in the P-wave travel time data for the 588 events, compared to the 1-D model.

The derived 3-D model shows velocities that average slightly slower than for the 1-D model (Table 2) but are generally in agreement. Laterally, the velocities vary over a range of about ±10% in a given depth layer. The 2 to 10 km depth range of the earthquakes means there is little resolution in the model below 10 km. The station terms are also generally similar to those obtained in the 1-D analysis. The 3-D velocity model and station corrections were used to relocate all of the recorded aftershocks. Quality A and B events, plus those with $M_L \geq 5.0$, are shown in Fig. 11b. This represents mainly the time period when the portable stations were operational in June 1994. The relocated distribution of aftershocks appears to be more clustered compared to the locations determined with a 1-D structure, suggesting that there are significant improvements to the hypocenter locations. These locations clarify some spatial patterns of the aftershocks and provide a better basis for interpreting their relation to geological features.

5.3 Temporal Distribution of Foreshocks and Aftershocks

Three small earthquakes (M_L2.4–2.8) were recorded within 25 km of the mainshock epicenter during the 2 weeks prior to the earthquake. This is not a significant increase on the previous year's activity in the same region (25 events). However, the last event (M_L2.6) occurred closest to the mainshock, on the preceding day and so is likely to be an immediate foreshock. The NZNSN has a magnitude completeness threshold of only M_L3.0 in this region and so other foreshocks could easily have occurred. In a recent study in the western United States, Abercrombie and Mori (1996) found foreshock occurrence to be closely related to the hypocentral depth and slip orientation of the mainshock. Their results suggest that roughly 20% of earthquakes with depth and mechanism similar to that of the Arthur's Pass earthquake will have immediate foreshocks ($M_L \geq 2$).

The magnitude distribution and decay rate of the Arthur's Pass aftershocks are well modelled by the Gutenberg-Richter law

$$N(M) = 10^{a-bM}$$

and Omori's law

$$R(t) = (t + c)^{-p}$$

where N is the number of events of magnitude M or more, R is the rate of activity, t is time, and a, b, c, and p are constants. The magnitude completeness threshold is high in the first hours following the mainshock, and at a minimum of M_L2.0 during the period of the portable instrument deployment. For the time period starting 2 hours after the mainshock and extending to the end of 1994, the magnitude completeness threshold is M_L3.3, as judged by a plot of b-value against completeness threshold. If lower thresholds are used then the b-value begins to decrease, indicating incompleteness. Over this threshold and time period the b-value is 1.01 ± 0.04, calculated using the maximum likelihood method (Aki, 1965). The p-value is 1.12 ± 0.07, calculated using a least squares method. These values are typical for aftershock sequences both in New Zealand (Eberhart-Phillips, 1998) and elsewhere (Reasenberg and Jones, 1989).

The rate of aftershocks decayed steadily with time except for small increases following the two largest aftershocks. This increased activity tended to be spread over the whole aftershock zone rather than being localised in the region of the large aftershocks. This effect was also observed by Webb and Lowry (1982) for an earthquake south of New Zealand.

The spatial distribution of the aftershock sequence exhibits some variation with time. Within the first 20 minutes the aftershocks were restricted to the northern half of the area, but within less than an hour, aftershocks were occurring throughout the complete aftershock area. The first $M_L \geq 5$ earthquake (14 minutes after the mainshock, M_L5.1) was the only one to occur in the northern half of the area. All but one of the other $M_L \geq 5$ events were located in the southern half of the area, concentrated on 18 June (1.5 to 3.5 hours after the mainshock), 19 and 21 June (Table 1, Fig. 12). Activity was initially higher in the north, around the mainshock, but became higher in the south once the major aftershocks had started to occur.

5.4 Spatial Distribution of Aftershocks

The Arthur's Pass aftershock sequence does not look out of the ordinary in terms of the magnitude distribution and temporal decay of the earthquakes, but it has a complex and unusual spatial distribution. The best located aftershocks from the 3-D inversion are shown in map and cross-sectional view in Figs. 12–15. The aftershocks delineate a region elongated in a NNW-SSE direction, extending approximately 35 km to the south of the mainshock but only about 12 km to the north. In map view, many sub-parallel and conjugate lineations can be traced forming a complex pattern, suggesting activation of the Harper and Bruce faults. The depth range (see Fig. 13) of the aftershocks is quite shallow, extending from about 1 to 10 km. Little variation in aftershock depth is seen throughout the zone, although the maximum depth appears to decrease north of the mainshock (Fig. 13). The lack of very shallow aftershocks is only partly due to the requirement for depths to be greater than 2/3 the distance to the nearest seismograph for the quality to be sufficient for the event to be plotted. If this requirement is relaxed, section AA' only shows 4 events shallower than 1 km and 48 shallower than 2 km out of a total of about 2,000.

We have considered the aftershock pattern in two parts; first the region around the mainshock hypocenter in an attempt to identify the fault plane, and second the extensive activity extending to the south.

The aftershocks do not delineate a clear fault plane. Usually the earliest aftershocks in a sequence are the best for constraining a fault plane, but for this event they occurred before the installation of the portable recorders, so they are mostly too poorly located to be of use. Fig.

14 shows cross-sections approximately perpendicular to the strike of the nodal planes of the preferred mainshock focal mechanism. The aftershocks within 3 km of the mainshock epicenter define a possible plane, dipping to the NW (Fig. 14a). The dip is in good agreement with the dip of the SW striking nodal plane of the mainshock focal mechanism. Parallel cross sections to the SW of the mainshock show this feature becoming less distinct, and then being present more as the northern limit to the seismicity extending to the south. In Fig. 15 we have plotted all quality A and B events within 2 km of the fault plane inferred from the body-wave focal mechanism. There is a noticeable lack of activity immediately below the hypocentre, and a patch of lower activity 5 km SW of the hypocentre (seen more clearly in Fig. 11b). These areas of lower activity may correspond to areas of maximum slip.

Cross sections perpendicular to the main trend of the aftershock sequence reveal activity on a number of subparallel faults, steeply dipping to the WNW. One of these is the Harper fault and a second is likely to be an extension of the Bruce fault. Detailed geological mapping of the region reveals a number of active faults subparallel to these (Cave 1987). It is also possible to identify two en-echelon (right stepping) lineations of aftershocks approximately perpendicular to the Harper and Bruce faults, suggesting conjugate faulting occurred. These structures appear close to vertical and are bounded by the hypothesized mainshock fault plane in the north and the Harper fault in the south (Figs. 12–14).

The largest aftershocks are all located close to the Harper fault, and so may involve slip on this, or nearby, active structures. Both east and west dipping thrust faults have been mapped here (Chamberlain 1996), one of which is the Harper fault. Using regional data, a focal mechanism can only be calculated for the one of the M_L5 aftershocks ($M_L5.1$, 29 June, Table 1) which occurred during the portable station deployment (Robinson and McGinty, this volume). It is well located on the extension of the Bruce fault and has a strike-slip mechanism consistent with slip on the Bruce fault or a conjugate (Fig. 12). A composite first motion mechanism of the seven $M_L \geq 5$ earthquakes closest to the Harper fault (Table 1) has 80 observations, only 5 of which are inconsistent with a strike-slip mechanism, similar to that of the 29 June aftershock, and the teleseismic mechanism derived for the $M_w5.9$ aftershock (Fig. 9). If they ruptured the Harper fault, the sense of motion would disagree with that mapped by Chamberlain (1996), while the rupture of a conjugate fault might not.

Robinson and McGinty (this volume) determined focal mechanisms for 78 aftershocks. They found that the area around the mainshock includes a mixture of reverse and strike-slip faulting, typical of the aftershocks of a reverse earthquake. The southern half of the aftershock zone, however, is dominated by strike-slip faulting with mechanisms similar to that of the largest aftershock shown in Fig. 9.

In summary, the aftershocks around the mainshock hypocenter appear to define a plane dipping to the NW which is probably the fault plane of the Arthur's Pass earthquake. We discuss its implications for mainshock rupture in the next section. The Harper fault forms a southern boundary to the NNW-SSE trending seismicity. The aftershocks south of the mainshock fault plane appear to result from activation of subparallel ENE-WSW faults (including the Bruce fault and perhaps the Harper fault) and their conjugates. The focal mechanisms of the largest aftershocks suggest strike-slip motion on these faults or their conjugates.

6. RESULTS AND DISCUSSION

6.1 Mainshock Source Parameters

The analysis of teleseismic and regional recordings of the mainshock constrains the Arthur's Pass earthquake to be a shallow, predominantly reverse faulting event. The depth range of the aftershocks (~ 1 to 10 km) is in good agreement with a centroid depth of about 5 km. The shallow depth is consistent with a thin seismogenic zone in this region caused by high heatflow associated with the rapid uplift of the Southern Alps (Allis and Shi, 1995).

The well located aftershocks near the epicenter define a plane dipping to the NW, at an angle consistent with the preferred mainshock focal mechanism (Table 1). The mainshock hypocenter is relocated at the NE end of the fault zone defined by the aftershocks, near the base of the aftershock zone. Large crustal earthquakes typically nucleate near the base of the aftershock zone (Sibson, 1982). It is likely, therefore, that the Arthur's Pass earthquake ruptured upwards and unilaterally towards the SW. The lack of aftershocks 5 km to the SW of the epicenter (Fig. 11b) is consistent with this being the location of the main energy release. Such a unilateral rupture is also within the constraints of the empirical Green's function analysis.

In many studies mainshock fault planes have been clearly delineated by high quality relocated aftershocks (e.g. the 1990 Weber earthquake, Robinson, 1994). However, there are some examples of dip-slip earthquakes where many aftershocks occurred in the hanging wall (e.g. 1987 Edgecumbe, New Zealand, Robinson, 1989; 1983 Coalinga, California, Eberhart-Phillips, 1989), or ceased to delineate a rupture plane away from the hypocentre (1994 Northridge, Hauksson et al., 1995).

The source duration and the extent of the aftershock zone around the mainshock can be used to estimate the dimensions of the area of rupture. The source had a rise time of 5–6 s (Fig. 8), which with a rupture velocity of 0.8 V_s, implies a fault dimension of 13–16 km. While the rupture is assumed to be predominantly unilateral to the SW, the aftershocks do extend about 3 km to the NE from the mainshock epicentre (Fig. 11b), giving an overall rupture length of 16–19 km. A fault width of 12 km is obtained from the fault plane dip (50°, Table 1) and the aftershock depth range (Fig. 15). These dimensions yield a relatively high average stress drop of 9–12 MPa (Eshelby, 1957). These values are high in comparison with other earthquakes, even reverse ones. The 1994 Northridge event was about 7.4 MPa (Wald et al. 1996), while 1983 Coalinga and 1972 San Fernando were around 5 MPa. The 1995 Cass, New Zealand, earthquake was an oblique reverse event (Gledhill et al., 1998) and also had a fairly high average stress drop (5 to 10 MPa). Although high, the stress drop of the Arthur's Pass earthquake is still within the range of crustal earthquakes (Kanamori, 1994; Abercrombie et al. 1995).

The rupture length derived from aftershock data alone would be 15 km (Fig. 11b), which is slightly shorter than that derived from the source time function rise time. The rupture could have extended further than the aftershock zone (i.e. the aftershocks do not extend over the full area of co-seismic slip), as was observed for the Landers earthquake (Hauksson et al., 1993). It is more common, however, for the aftershock area to be larger than that of the mainshock slip. A few aftershocks do occur beyond the ends of the fault plane defined above. They could indicate a longer fault length, but are more likely to be occurring in the regions of

increased static stress at either end of the mainshock rupture (Robinson and McGinty, this volume).

The alternative possibility that the Arthur's Pass earthquake was primarily a strike-slip event on a fault striking along the backbone of the aftershock zone, would allow a longer rupture length and hence a lower stress drop. This scenario is, however, completely inconsistent with the body-wave modeling and also a more detailed look at the aftershocks. In addition, forward modeling of the SAR interferometric pattern produced by the earthquake (Pearson et al., 1997) shows that these data cannot be matched by a strike-slip event and are well matched using the body-wave solution given in Table 1. The region of maximum damage, including landslides, is also restricted to the northern half of the aftershock region, consistent with the preferred reverse faulting mainshock. The spatial distribution of aftershocks extending so far to the south is certainly unusual, but as shown by Robinson and McGinty (this volume), it is in excellent agreement with the areas where increased static stress is predicted following a reverse mainshock, given the regional stress field. Aftershock occurrence has been found to correlate well with areas of predicted increased static stress following large earthquakes both in New Zealand (McGinty et al., 1997), and elsewhere (King et al., 1994).

In the introduction the discrepancies between the three different CMT solutions for the Arthur's Pass earthquake were mentioned (Fig. 3). The preferred reverse mechanism for the earthquake is in poor agreement with all three. It is a shallow event, however, (aftershock depth ~1–10 km) and all three CMT solutions have fixed depths which are substantially deeper (e. g. 15 km for the Harvard solution). As mentioned in Section 2, there is a strong trade-off between centroid depth and the dip-slip component in the CMT inversion of shallow earthquakes. It is probable, therefore, that the three CMT solutions are all underestimating the dip-slip component by fixing the centroid at too great a depth and so are poor representations of the source process of the Arthur's Pass earthquake.

6.2 The Red Rock Fault

No surface rupture has been observed following the Arthur's Pass earthquake and so this could not be used to help identify the fault which slipped. The area around the epicenter has previously been mapped in some detail (Cave, 1987). The Red Rock fault has approximately the right orientation and location (just 3 km NE of the surface projection of our hypothesized fault plane, i.e. within location and mechanism errors) to be the mainshock fault plane. Less than 10 km to the NE of the epicenter the Red Rock fault dips to the NW (M. Cave, pers. comm., 1997). It seems quite possible, therefore, that the Arthur's Pass earthquake ruptured the Red Rock fault. The mountainous terrain and early uncertainty of the expected location of surface faulting meant that the part of the Red Rock fault near the rupture zone has not been examined in detail since the earthquake. No fresh displacement was observed 10 km to the NE of the rupture zone, where the fault crosses a river terrace (Berryman, pers. comm., 1998).

6.3 GPS Compatibility

A GPS survey was carried out around Arthur's Pass in 1992, and the area was resurveyed following the earthquake in 1994 and again in 1995. Arnadottir et al. (1995) inverted the displacements observed between 1992 and 1994, assuming slip on a single fault. They could

not match the data well assuming uniform slip, and so allowed the fault to have two parts with independent slip on each. They found that a NNW-SSE striking fault with about 5 m of sinistral-reverse motion on the northern part and about 0.6 m of sinistral motion in the south best matched the data.

This single fault model is clearly incompatible with the fault model derived from the seismic recordings, but then a single fault rupture is not a good model of the cumulative seismicity between the GPS surveys. The observed GPS displacements include both the mainshock and most of the aftershocks. The total moment of the large aftershocks ($M_L \geq 5$) is only about 15% of that of the mainshock, but they are located about 15 km from the epicenter, and close to the two GPS stations with the largest (southward) displacements. Also, the large aftershocks have very different focal mechanisms to that of the mainshock, being predominantly strike-slip.

The GPS data alone, with about 20 points in the near-field of the earthquake, are not sufficient to constrain reliably a two-fault inversion, since each fault requires nine parameters to describe it. Arnadottir (1995) therefore performed a two-fault inversion with the strike, dip and rake of one fault constrained to those of the 3 km depth body-wave modeling solution (strike, dip and rake 213°, 47° and 90°, respectively), and all the other parameters allowed to vary. The best-fitting model with these constraints has the second fault very similar to the southern part of the single-fault model, with almost pure sinistral motion. This is consistent with the focal mechanism of the largest aftershocks (Fig. 12). However, the GPS model has a combined moment of 1.9×10^{19} Nm, with the two faults contributing approximately half each. This is clearly incompatible with the distribution of seismic moment between the mainshock and largest aftershocks, and has lead to speculation that significant aseismic slip may be required in the south (Abercrombie et al., 1996a).

Since the work of Arnadottir et al. (1995) and Arnadottir (1995), we have reanalysed the 1992, 1994 and 1995 GPS data, and have collected and analysed data from 1997 (Beavan and others, in prep., 1998). The 1995–1997 data allow us to estimate an interseismic deformation correction from the GPS data, rather than the linear model used by Arnadottir et al. (1995). The new analyses and corrections do not significantly alter the coseismic data inverted in the two Arnadottir studies. However, there is evidence of postseismic deformation in the 1995–97 data in the region at the northwestern edge of the aftershock zone, which adds to evidence discussed earlier in this paper that the mainshock rupture plane dips to the northwest. The coseismic deformation patterns estimated from the 1992–1994 and 1992–1995 data are very similar. We have performed forward dislocation modeling on both sets of data in a spirit similar to that of Arnadottir (1995). Arnadottir searched rigorously for the best fitting two-fault model with the mainshock fault constrained to have the strike, dip and rake estimated from body-wave modeling. We allow the mainshock fault plane parameters to vary modestly from the body-wave values and search for a second, predominantly strike-slip, subsidiary fault with as small a moment as possible that still adequately fits the GPS data. We have not done this search rigorously, but it appears possible to find a combination of faults such that the slip on the subsidiary fault is less than about 0.5 m, and its moment is about 25–30% of the main shock moment. This is larger than the 15% moment ratio estimated for the aftershocks, but not unduly so. Given that the aftershocks south of the mainshock fault plane appear to result from activation of subparallel ENE-WSW faults and their conjugates, we expect that a model that allowed slip on all these structures could be constructed to fit the GPS data with a moment ratio close to 15% without the necessity for invoking significant aseismic slip. Unfortunately, the complexity of the earthquake and the number of structures

activated means that this supposition cannot be rigorously tested with the limited GPS data available.

A further note of caution in interpreting the GPS data is that the relatively large moment inferred for the subsidiary fault is dependent to some extent on the displacements at just two stations, one of which may have been very close to the rupture. Inspection of these sites after the earthquake revealed no evidence for local ground instability, but field evidence of displaced boulders indicated that accelerations in excess of 1 g occurred in the near field. It thus remains a possibility that some of the closer GPS stations did suffer local disturbance as well as recording the regional deformation field from the earthquake.

6.4 Implications for Seismic Hazard and Regional Tectonics

The central South Island was historically considered to have a low rate of seismicity, located between Eiby's *Main Seismic Region* to the north, and the Fiordland activity to the south (Eiby, 1971). More recent studies (e.g. Anderson and Webb, 1994) show a relatively high rate of small earthquakes in the region over the period 1990–1993, now that the magnitude threshold for the region is about 3.0, rather than the previous 4+, following the upgrade of the NZNSN in 1990. A natural question to ask is whether this higher rate of recent activity is simply a function of better detectability, or whether it is a temporal variation. The answer is both. An improved network has meant that many intermediate depth (particularly 30–50 km) earthquakes along both subduction zones that were previously assigned a shallow depth are now located within the subducting plates. The rate of true crustal activity above the subduction zones is thus lower than what used to be thought. Hence parts of the central South Island can be considered to be as active as many other regions in New Zealand in terms of crustal activity (see Anderson and Webb, 1994, Fig. 8). There also appears to have been a temporal increase. Of the 5 events greater than magnitude 6.0 since 1943, 4 occurred in the interval 1992–1995. However, these 4 comprise the Arthur's Pass mainshock, 2 aftershocks, and the triggered Cass event (Robinson and McGinty, this volume) so, although there has been more activity in this period, it is inter-related. Given that it is the shallow crustal earthquakes that are most damaging, the seismic hazard in the central South Island must be higher than previously thought, relative to other parts of the country.

Anderson et al. (1993) showed that for earthquakes in the northern South Island, the plate tectonic motion was accommodated through strike-slip motion, with slip vectors not quite in agreement with plate motion in the east, and reverse faulting in the Buller region to the west. The slip vectors in each region were of the correct orientation to sum to the plate motion, although rates of activity were too poorly constrained to show that this sum balanced. They noted that slip vectors derived from strike-slip events further to the south showed a similar deviation from the plate motion direction, but they found no corresponding reverse events in the period 1964–1992. More recently, Doser et al. (1998) have modeled large historical South Island events. They found the same discrepancy as Anderson et al. (1993) between slip vectors of strike-slip earthquakes and plate motion, and also found that the 1947 Jackson's Bay earthquake in the southern South Island was a reverse event with the same orientation as events in the Buller region, and the 1994 Arthur's Pass earthquake studied here. This suggests that the plate tectonic motion is partitioned into strike-slip and reverse components along the length of continental collision in the South Island, and that the mechanisms of the reverse events are remarkably similar. The similarity in some regions may be due to the

reverse events occurring on reactivated normal faults, but that is unlikely to be true in the Arthur's Pass region.

7. CONCLUSIONS

Teleseismic body-wave modelling shows that the Arthur's Pass earthquake was a shallow, reverse faulting event. An empirical Green's function analysis confirmed that the source time function was simple and that the source duration was 7.5 s. The combined body-wave and empirical Green's function data suggest a centroid depth of 5 km. We suggest that the disagreement with CMT solutions is due to the shallow source depth where the CMT method has difficulty resolving vertical dip-slip and centroid depth. We have determined a relatively high stress drop of 9–12 MPa from the source rise time and aftershock distribution.

The aftershocks have an unusual spatial distribution. They only clearly define the fault plane at one end, rapidly becoming diffuse away from that region. There is extensive aftershock activity orthogonal to the fault plane on what we consider to be ENE-WSW faults or their conjugates. Aftershock activity was limited to the NW for the first 20 minutes of the sequence. The spatial distribution can be explained in terms of regional and induced stresses (Robinson and McGinty, this volume). The aftershock depth range of 1 to 10 km agrees well with the centroid depth. The rupture probably occurred on the Red Rock fault, although no fresh surface trace has yet been found.

Both body-wave modeling of the largest aftershock and a composite mechanism for the events with $M_L \geq 5.0$ result in strike-slip solutions. Individual focal mechanisms of smaller aftershocks near the mainshock fault plane show more reverse mechanisms (Robinson and McGinty, this volume).

Forward modeling of the GPS data suggests that a predominantly reverse slip mainshock, combined with strike-slip faulting in the south is able to match the observed surface displacements.

The spatial distribution of aftershocks of the Arthur's Pass earthquake is unusual. The fact that such aftershock distributions are possible, and can be predicted from modeling of the static stress changes (Robinson and McGinty, this volume), renders caution necessary in picking fault planes from poorly recorded and located aftershock sequences.

Shallow crustal earthquakes appear to be more common in the central South Island than previously thought. Consequently, the level of seismic hazard in the region must be higher than previously estimated relative to other parts of New Zealand. The predominantly reverse mechanism for this event is consistent with slip partitioning along the length of the continental collision zone in South Island.

Acknowledgments

We would like to thank Kelvin Berryman, Murray Cave, and Russ Van Dissen for useful discussions relating to the geology, Graham Hancox and Nick Perrin on landslides, and Ken Gledhill and Goran Ekstrom on seismology. Jim Cousins kindly provided the strong motion data. Martin Reyners, Michael Kopeykin, Ray Maunder, and Alan Cresswell assisted with

the microearthquake fieldwork. All of the aftershocks were analyzed by staff associated with the Seismological Observatory program. Funding was provided by the Earthquake Commission and the Foundation for Research, Science and Technology.

REFERENCES

Abercrombie, R.E., I.G. Main, A. Douglas and P.W. Burton, 1995, The nucleation and rupture process of the 1981 Gulf of Corinth earthquakes from deconvolved broad-band data, *Geophys. J. Int.*,120, 393–405, 1995.

Abercrombie, R. E. and J. J. Mori, Occurrence patterns of foreshocks to large earthquakes in the western United States, *Nature*, 381, 303–307, 1996.

Abercrombie, R. E., Webb, T. H., Robinson, R., Beavan, J. and Arnadottir, T., The 1994 Arthur's Pass earthquake: evidence for aseismic slip?, *EOS*, **77** (supplement), F740, 1996a.

Abercrombie, R. E., Webb, T. H., Bannister, S., Robinson, R., Beavan, J. and Arnadottir, T., The enigma of the Arthur's Pass earthquake, *EOS*, **77** (supplement), W90, 1996b.

Abercrombie, R. E., Robinson, R., Webb, T. H., McGinty, P. J., Beavan, J., The 1994 M_w6.7 Arthur's Pass earthquake, *Geol. Soc. NZ. Misc. Pub.* 95A, 1, 1997.

Aki, K., Maximum likelihood estimate of b in the formula Log N = a - bM and its confidence limits, *Bull. Earth. Res. Inst.*, 45, 237–239, 1965.

Allis, R.G. and Y. Shi, New insights into temperature and pressure beneath the central Southern Alps, New Zealand, *NZ J. Geol. & Geophys.*,38, 585–592, 1995.

Ammon, C., T. Lay, A. A. Velasco and J. E. Vidale, Routine estimation of earthquake complexity: the 18 October 1992 Columbian earthquake, *Bull. Seism. Soc. Am.*, 84, 1266–1271, 1994.

Anderson, H., T. Webb, and J. Jackson, Focal mechanisms of large earthquakes in the South Island, New Zealand: implications for the accommodation of Pacific–Australia plate motion, *Geophys. J. Int.*, 115, 1032–1054, 1993.

Anderson, H. and T. Webb, New Zealand seismicity: patterns revealed by the upgraded National Seismograph Network, *NZ J. Geol. & Geophys.*, 37, 477–493, 1994.

Arnadottir, T., J. Beavan, and C. Pearson, Deformation associated with the 18 June 1994 Arthur's Pass earthquake, New Zealand, *NZ J. Geol. & Geophys.*,38, 553–558, 1995.

Arnadottir, T., Seismotectonics of the Arthur's Pass earthquake of 18 June, 1994, *Progress report from analysis of GPS data for the Earthquake Commision,* 1995.

Cave, M., Geology of Arthur's Pass National Park, *New Zealand National Parks Scientific Series*, 7, 1987.

Chamberlain, C.G., Seismic hazard from cross-faulting in North Canterbury: broader implications from the Arthur's Pass earthquake sequence of 18 June 1994, *Unpublished Engineering Geology MSc (Hons) thesis, University of Canterbury, New Zealand,* 1996.

Cowan, H.A., The North Canterbury earthquake of September 1, 1888, *J. Roy. Soc. N.Z.*, 21, 1–12.

Crosson, R.S., Crustal structure modelling of earthquake data, 1, Simultaneous least squares estimation of hypocentres and velocity parameters. *J. Geophys. Res.*, 81, 3036–3046, 1976.

Davey, F.J. et al., Preliminary results from a geophysical study across a modern, continetal–continental collision plate boundary — the Southern Alps, New Zealand, *Tectonophysics,* 288, 221–235, 1998.

DeMets, C., R.G.Gordon, D. F.Argus, and S. Stein, Current plate motions, *Geophys. J. Int.*, 101, 425–478, 1990.

Doser, D.I., T.H. Webb, & D.E. Maunder, Source parameters of large historic (1918–1962) earthquakes, South Island, New Zealand, (in prep.), 1998.

Dreger, D. S., Empirical Green's function study of the January 17, 1994 Northridge, California earthquake, *Geophys. Res. Lett.*, 21, 2633–2636, 1994.

Dreger, D. S., J. Ritsema and M. Pasyanos, Broadband analysis of the 21 September, 1993, Klamath Falls earthquake sequence, *Geophys. Res. Lett.*, 22, 997–1000, 1995.

Dziewonski, A. M., Chou, T. A. & Woodhouse, J. H., Determination of earthquake source parameters from waveform data for studies of global and regional seismicity, *J. Geophys. Res.*, 86, 2825–2852, 1981.

Eberhart-Phillips, D., Active faulting and deformation of the Coalinga Anticline as interpreted from three-dimensional velocity structure and seismicity: *J. Geophys. Res.*, 94, 15565–15586, 1989.

Eberhart-Phillips, D. , Local earthquake tomography: earthquake source regions, in Seismic Tomography: Theory and Practice, edited by H.M. Iyer and K. Hirahara, Chapman and Hall, London, 613–643, 1993.

Eberhart-Phillips, D., Examination of seismicity in the central Alpine fault region, South Island, New Zealand, *N. Z. J. Geol. Geophys.*, 38, 571–578, 1995.

Eberhart-Phillips, D., Aftershock sequences in New Zealand, *Bull. Seism. Soc. Am*, 1998 (in Press).

Eiby, G.A., Seismic regions of New Zealand, *Recent Crustal Movements, Roy. Soc. N.Z. Bull.*, 9, 153–160, 1971.

Eshelby, J. D., The determination of the elastic field of an ellipsoidal inclusion and related problems, *Proc. R. Soc. London A, 241*, 376–396, 1957.

Futterman, W. I., Dispersive body waves, *J. Geophys. Res.*, 67, 5279–5291, 1962.

Gledhill, K.R., M.J. Randall, & M.P. Chadwick, The EARSS digital seismograph: system description and field trials, *Bull. Sesim. Soc. Am.*, 81, 1380–1390, 1991.

Gledhill, K., R. Robinson, T. Webb, R. Abercrombie, D. Eberhart-Phillips, J. Beavan and J. Cousins, The M_w6.2 Cass, New Zealand, earthquake of 24 November, 1995: reverse faulting in a strike-slip region, in prep. 1998.

Gordon, R. Eye witness at epicentre: The Arthur's Pass earthquake at close quarters, *NZ Geophys. Soc. Newsletter*, 39, 40–41, 1994.

Hancox, G.T., N.D. Perrin and G.D. Dellow, Earthquake-Induced Landsliding in New Zealand and Implications for MM Intensity and Seismic Hazard Assessment, *Inst. Geol. Nuc. Sci. Client Report*, 43601B, 1997.

Hauksson, E., L. Jones, and K. Hutton, The 1994 Northridge earthquake sequence in California: seismological and tectonic aspects, *J. Geophys. Res.*, 100, 12335–12355, 1995.

Hauksson, E., L. Jones, K. Hutton and D. Eberhart-Phillips, The 1992 Landers earthquake sequence: seismological observations, *J. Geophys. Res.*, 98, 19835–19858, 1993.

Kanamori, H., Mechanics of earthquakes, *Ann. Rev. Earth Planet Sci.*, 22, 207–237, 1994.

King, G.C.P., R. Stein and J. Lin, Static stress changes and the triggering of earthquakes, *Bull. Seism. Soc. Am.*, 84, 935–953, 1994.

Langston, C. A. & Helmberger, D. V., A procedure for modelling shallow dislocation sources, *Geophys. J. R. astr. Soc.*, 42, 117–130, 1975.

McGinty, P., R. Robinson, J. Taber, and M. Reyners, The 1990 Lake Tennyson earthquake sequence, Marlborough, New Zealand, *NZ J. Geol. & Geophys.*, 40, 521–535, 1997.

McCaffrey, R. & Abers, G., SYN3: a program for inversion of teleseismic body waveforms on microcomputers, *Air Force Geophysics Laboratory Technical Report*, AFGL-TR-88-0099, Air Force Geophysics Laboratory, Hanscom AFB, MA, 1988.

Mori, J. and S. Hartzell, Source inversion of the 1988 Upland, California, earthquake: determination of a fault place for a small event, *Bull. Seism. Soc. Am.*, 80, 507–518, 1990.

Nabelek, J. L., Determination of earthquake source parameters from inversion of body waves, Ph.D. thesis, MIT, MA, 1984.

Pearson, C., D. Massonnet and N. Pourthie, SAR study of the Arthur's Pass earthquake of 18 June 1994: implications for the tectonics of west-central Canterbury, *Geol. Soc. NZ. Misc. Pub.* 95A, 139, 1997.

Reasenburg, P.A. and L.M. Jones, Earthquake hazard after a mainshock in California, *Science*, 243, 1173–1176, 1989.

Reyners, M., P. McGinty, J. Ansell, and B. Ferris, The Tikokino earthquake of 11 April 1993: Movement at the plate interface in southern Hawkes Bay, *Bull. NZ Nat. Soc. Earth. Eng.*, 30, 242–251, 1997.

Robinson, R. and P.J. McGinty, The enigma of the Arthur's Pass, New Zealand, earthquake, 2: The aftershock distribution and its relation to regional and induced stress fields, *This volume*.

Robinson, R., M. Reyners, T. Webb, T. Arnadottir, J. Beavan, J. Cousins, R. Van Dissen and C. Pearson, The M_w6.7 Arthur's Pass earthquake in the Southern Alps, New Zealand, June 18, 1994, *Seism. Res. Letts.*, 66, 11–12, 1995.

Robinson, R., Seismicity, structure, and tectonics of the Wellington region, New Zealand. *Geophys. J. Roy. Astron. Soc.*, 87, 379–409, 1986.

Robinson, R., Aftershocks of the 1987 Edgecumbe earthquake, New Zealand: seismological and structural studies using portable seismographs in the epicentral region, *NZ J. Geol. & Geophys.*,32, 61–72, 1989.

Robinson, R., Shallow subduction tectonics and fault interaction: The Weber, New Zealand, earthquake sequence of 1990–1992, *J. Geophys. Res.*, 99, 9663–9679, 1994.

Scott, D.R. & H. Kanamori, On the consistency of moment tensor source mechanisms with first motion data, *Phys. Earth. Planet. Int.*, 37, 97–107, 1985.

Sibson, R. H., Fault zone models, heat flow, and the depth distribution of earthquakes in the continental crust of the United States, *Bull. Seism. Soc. Am*, 72, 151–163, 1982.

Van Dissen, R. and K. Berryman, The Arthur's Pass (Avoca River) earthquake of 18 June 1994: an overdue note regarding landslide damage and the search for surface rupture, *Geol.Soc. N. Z. Newsletter*, 28–33, 1995.

Wald, D. J., T. H. Heaton and K. W. Hudnut, The slip history of the 1994 Northridge, California, earthquake determined from strong motion, teleseismic, GPS and leveling data, *Bull. Seism. Soc. Am.*, 86, S49–70, 1996.

Webb, T.H. and M.A. Lowry, The Puysegur Bank earthquake of 1979 October 12, *NZ J. Geol. & Geophys.*, 25, 383–395, 1982.

Yang, J.S., Landslide mapping and major earthquakes on the Kakapo fault, South Island, New Zealand, *J. Roy. Soc. N.Z.*, 22, 205–212, 1992.

Table 1. Hypocentral Parameters (from the 3-D inversion) of the 15 largest earthquakes ($M_L \geq 5$) in the 1994 Arthur's Pass Sequence, and the preferred source parameters of the mainshock and principal aftershock.

* events used in the empirical Green's function analysis

$^+$ events with relatively well constrained depths (see text).

^{f} aftershocks used in the composite focal mechanism (Fig. 12).

Date	Time	M_L	Latitude (°S)	Longitude (°E)	Depth (km)	Centroid Source Parameters
6/18/94	03:25	6.7	42.975	171.483	9	strike = 221+5/-10°, dip = 47±5° rake = 112+5/-10°, depth = 5±1 km Mo = (1.3+0.4/-0.2)×10^{19} Nm
6/18/94	03:39	5.1	43.036	171.402	9	
6/18/94^f	05:04	5.1	43.140	171.491	5	
6/18/94*^{f}	07:03	5.3	43.149	171.487	7	
6/18/94	07:05	5.2	43.170	171.430	10	
6/18/94*^{f}	14:37	5.3	43.167	171.507	8	
6/19/94*^{f}	13:43	6.1	43.163	171.518	8	strike = 253±15°, dip = 87+5/-10° rake = 178+10/-20°, depth = 8+1/-4 km Mo = (5.8+0.4/-1.3)×10^{17} Nm
6/19/94	13:45	5.0	43.175	171.452	6	
6/19/94^f	21:54	5.2	43.161	171.520	10	
6/21/94*^{f}	02:18	5.7	43.180	171.525	4	
6/21/94^f	08:31	5.3	43.172	171.489	6$^+$	
6/29/94	05:38	5.1	43.099	171.483	10$^+$	
8/15/94	05:02	5.3	43.241	171.533	9	
8/23/94	01:12	5.0	42.940	171.404	10	
9/15/94	15:09	5.2	43.170	171.467	7	

Table 2. Velocity structure (a) from the 1-D inversion,

Depth to top of layer (km)	V_P (km/s)	V_S (km/s)
0	2.00	1.16
0.1	3.50	2.02
0.1	4.98	2.88
1.0	5.45	3.15
5.0	5.99	3.46
10.0	6.26	3.62
15.0	6.53	3.77
25.0	7.08	4.09
35.0 (Halfspace)	7.68	4.40

(b) from the 3-D inversion,

Node Depth (km)	V_P (km/s)
Surface (0)	4.68 ± 10%
1.0	5.34 ± 10%
3.0	5.59 ± 12%
5.0	5.80 ± 8%
10.0	6.04 ± 7%
15.0	6.29 ± 6%
30.0	7.06 ± 6%
Halfspace	8.10

(c) used in the mainshock body-wave modeling.

Depth to top of Layer (km)	V_P (km/s)	V_S (km/s)	Density (kg/m^3)
0	5.44	3.14	2600
3 (Halfspace)	6.03	3.49	2800

Figure Captions

Figure 1: Map of the New Zealand region showing the epicenter of the Arthur's Pass earthquake (star), the plate boundary, and principal faults. The stations of the NZNSN (triangles) and the GSN broadband station, SNZO (spot) are also marked. Arrows show Pacific-Australia plate velocity according to a Nuvel-1 model (DeMets et al., 1990).

Figure 2. The Arthur's Pass region showing historical and recent seismicity, and mapped faults. Unlabeled open circles show background seismicity with $M_L \geq 3.5$ for the 10 years preceding the Arthur's Pass mainshock. Unlabeled solid circles show aftershocks with $M_L \geq 3.5$ for both the Arthur's Pass and Cass events.

Figure 3. Equal area, lower hemisphere projections of focal mechanisms obtained by (a) Harvard (solid lines), NEIC (dashed lines), and (b) Zhang (solid lines), this study (dashed

lines). First motions are also plotted, with large symbols for teleseismic stations too close to be modeled, and small circles for regional stations.

Figure 4. Body-wave solution for the Arthur's Pass earthquake. The sub-title contains the strike, dip, and rake in degrees, depth in km, and scalar moment in N-m. Each waveform is labeled with the station code, identification letter. The "d" signifies digital data. Solid lines are the data, while dashed lines are the synthetic. Short vertical bars mark the time window used in the inversion, and a vertical scale is shown, all waveforms being normalised to that of an instrument with a gain of 3000 at a distance of 40°. The source time function, its time scale, and the waveform time scale (immediately below) are also shown. The upper circle shows the P wave nodal planes on an equal area projection of the lower focal hemisphere, with the P-axis marked with a solid circle and the T-axis an open circle. The lower circle shows the SH wave nodal planes. An asterisk below a station name indicates that this station had zero weight in the inversion.

Figure 5. A comparison of waveforms at a selected set of stations. The Harvard solution is shown in the top row. Row 2 is that solution, but with a free depth. Row 3 has the depth fixed at the Harvard depth and free strike, dip, and rake. Row 4 is the solution of Zhang (pers. comm., 1994. Row 5 is the NEIC solution. Row 6 is our minimum misfit solution. Crosses mark waveforms where the fit is judged to be poorer than the best fit for that station.

Figure 6. Mainshock (top) and largest aftershock (middle) seismograms recorded at (a) SNZO and (b) TAU and rotated to SH, and resulting deconvolved source time functions (bottom).

Figure 7. Comparison of the source time functions derived from GSN stations SNZO, TAU and NWAO. Station azimuths from are given in brackets.

Figure 8. Comparison of the results of the body-wave modeling at a range of fixed depths with the source time function determined using the empirical Green's function method at SNZO. The duration of the SNZO source time function is in consistent with a depth of 4–6 km.

Figure 9. Body-wave solution for the largest aftershock. Details are the same as for Fig. 4.

Figure 10. Routine locations of aftershocks with $M_L \geq 3.5$. Triangles denote portable seismographs deployed to record aftershocks.

Figure 11. Comparison of the locations of the ~2000 highest quality aftershocks located using (a) the 1-D inversion (quality A and $M_L \geq 5.0$ events) and (b) the 3-D inversion (quality A, B and $M_L \geq 5.0$ events). The mainshock focal mechanism is shown in both.

Figure 12. Map view of 3-D aftershock locations (quality A, B and $M_L \geq 5.0$ events) and the location of cross sections shown in subsequent figures. Also shown are the mainshock focal mechanism and a composite mechanism derived from first motions from all $M_L \geq 5.0$ aftershocks.

Figure 13. Cross section AA' through the 3-D locations and $M_L \geq 5.0$ events.

Figure 14. Parallel cross sections through the mainshock fault plane. Note the NW-SE sense from left to right.

Figure 15. Aftershock distribution (3-D quality A and B plus mainshock) over the fault plane derived from body-wave modeling and the aftershock distribution, viewed from the NW and above.

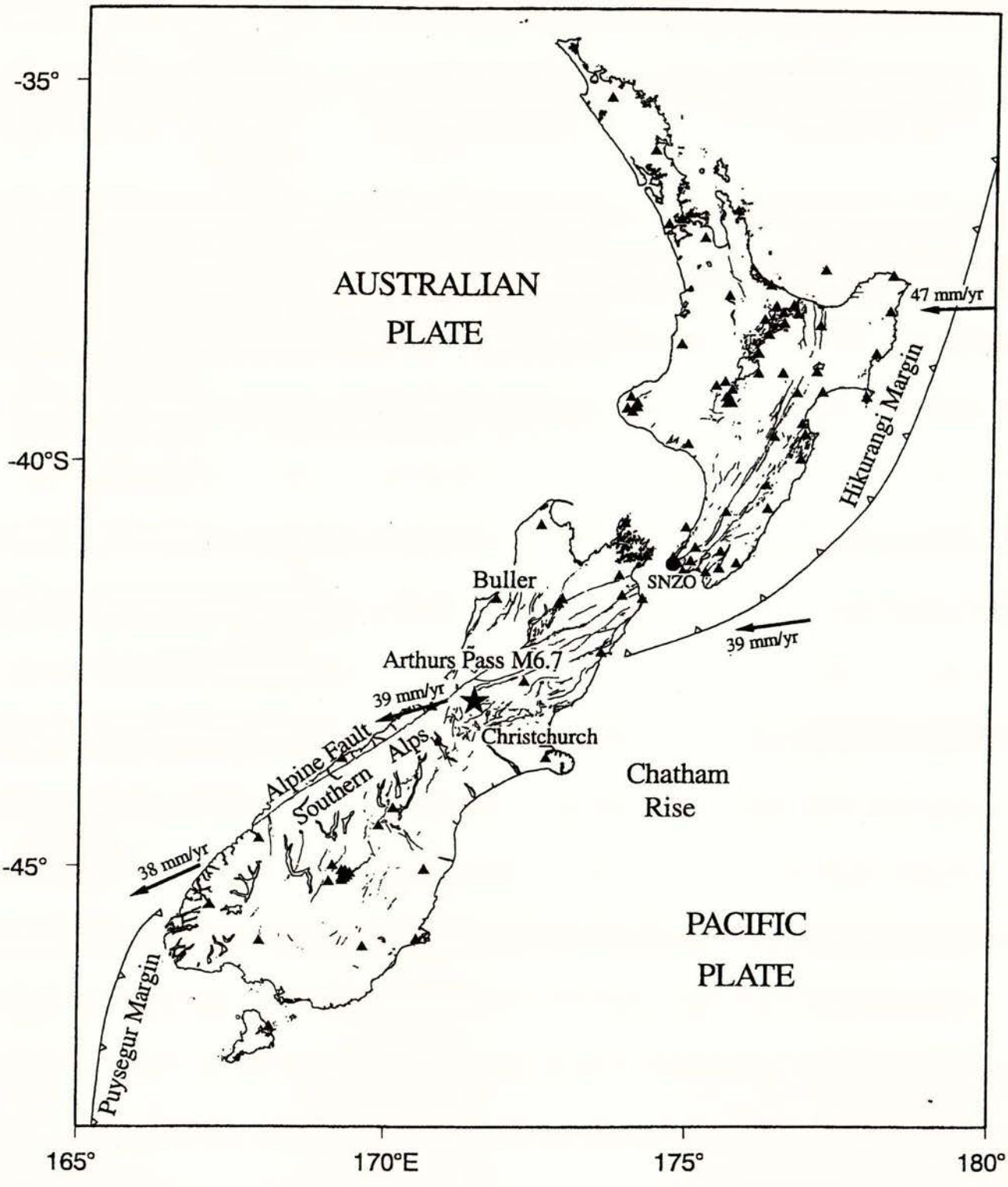
-35°
-40°S
-45°
165°
170°E
175°
180°
AUSTRALIAN
PLATE
PACIFIC
PLATE
47 mm/yr
Hikurangi Margin
39 mm/yr
SNZO
Buller
Arthurs Pass M6.7
39 mm/yr
Alpine Fault
Southern Alps
Christchurch
Chatham
Rise
38 mm/yr
Puysegur Margin

Figure 1

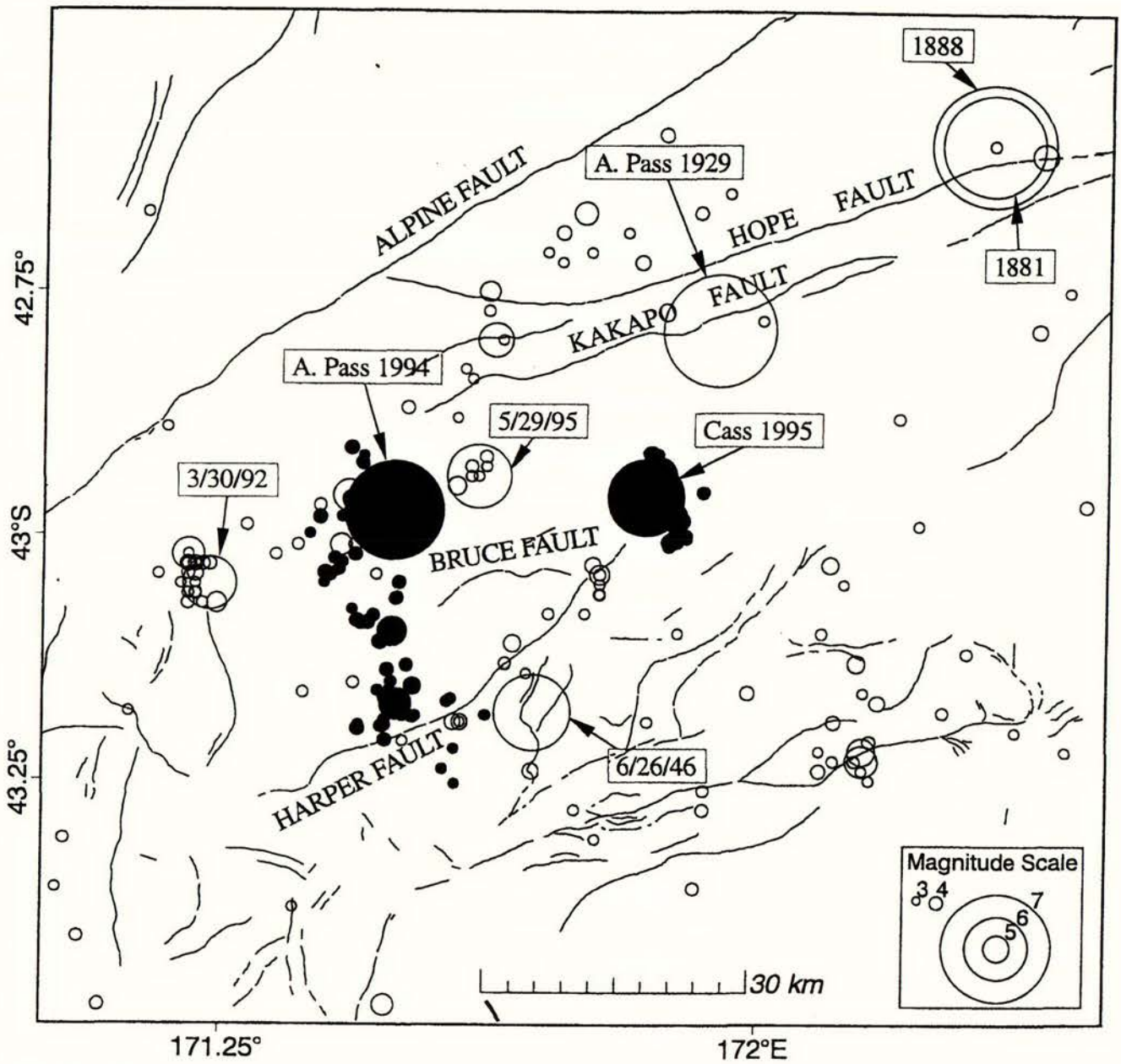
1888
A. Pass 1929
ALPINE FAULT
HOPE FAULT
1881
KAKAPO FAULT
A. Pass 1994
5/29/95
Cass 1995
3/30/92
BRUCE FAULT
HARPER FAULT
6/26/46
Magnitude Scale
3
4
5
6
7
30 km
42.75°
43°S
43.25°
171.25°
172°E

Figure 2

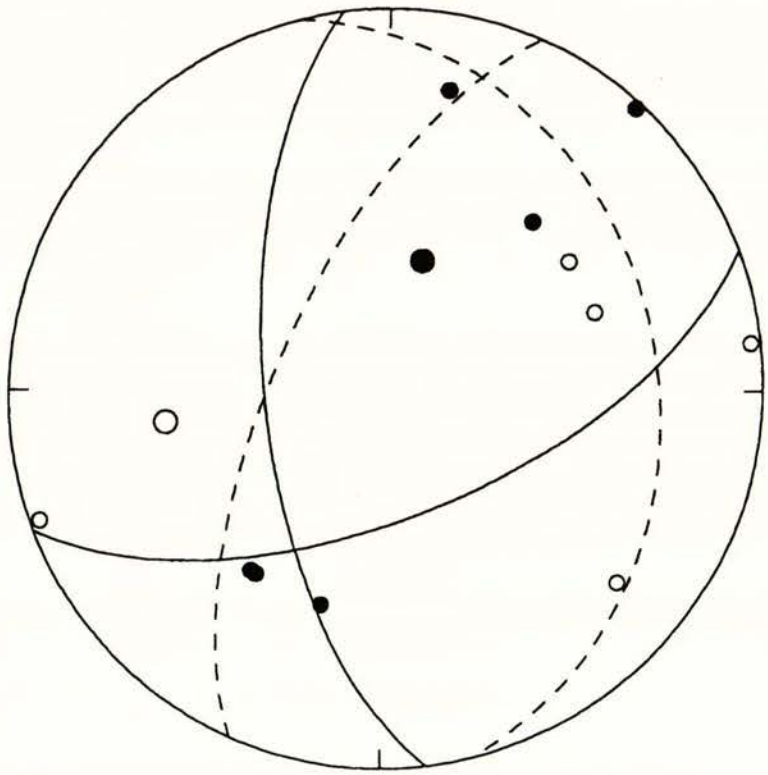

—— Strike, dip, rake = 173 64 31 (Harvard)

----- Strike. dip, rake = 346 29 56 (NEIC)

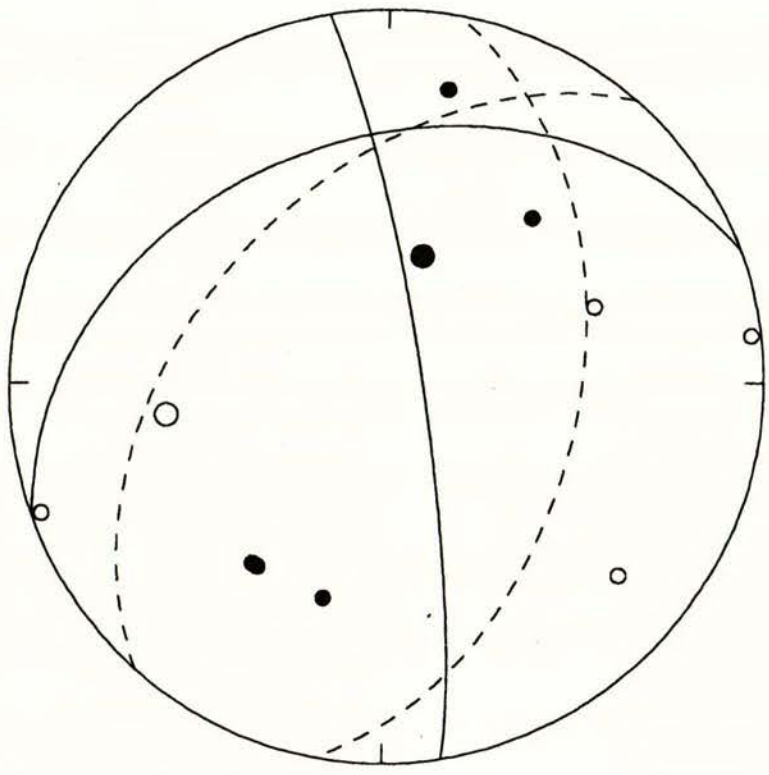

—— Strike, dip, rake = 351 82 56 (Zhang)

----- Strike. dip, rake = 221 47 112 (This study)

Figure 3

Arthurs Pass 94.06.18 Mw=6.7

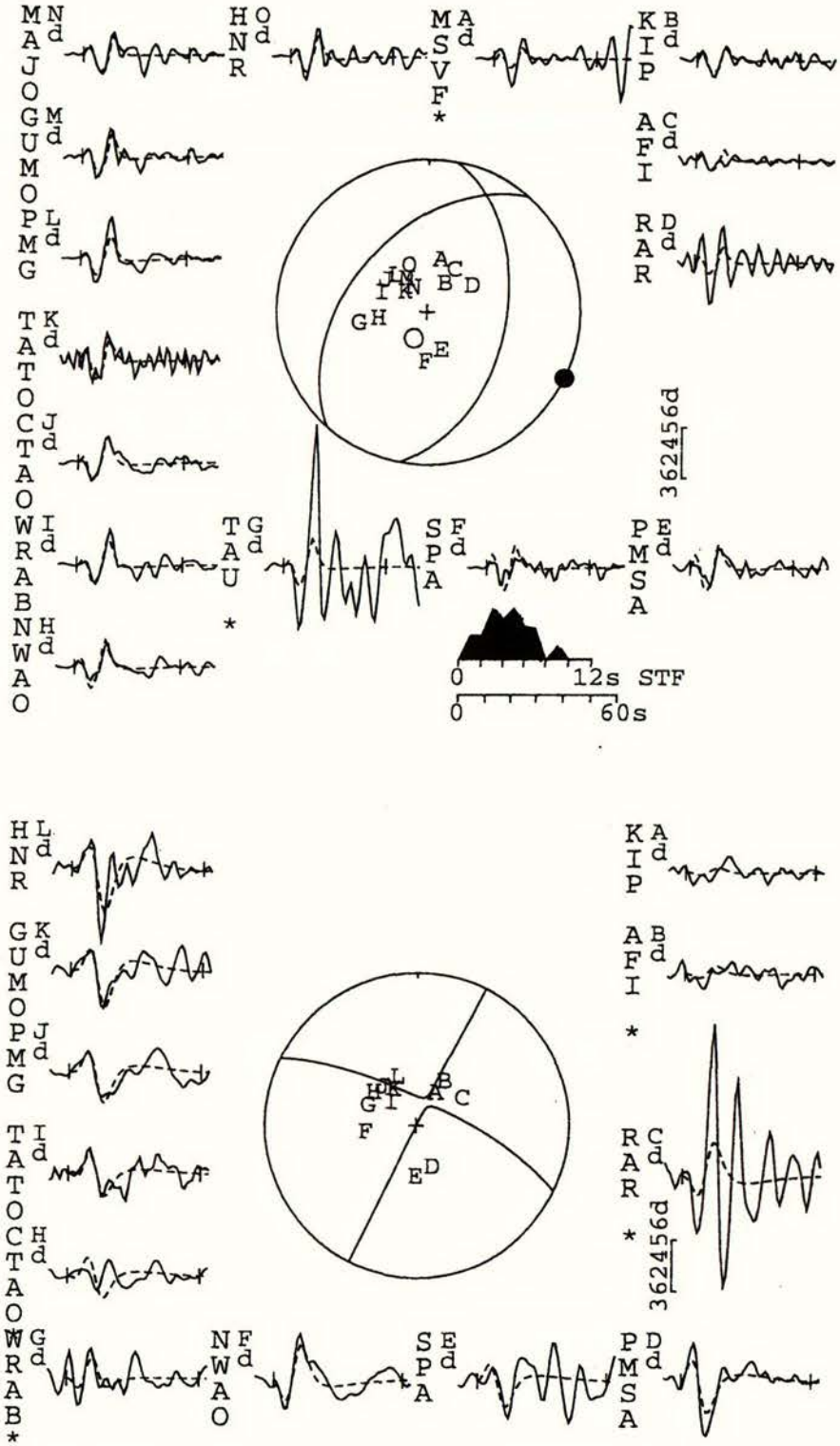

Figure 4

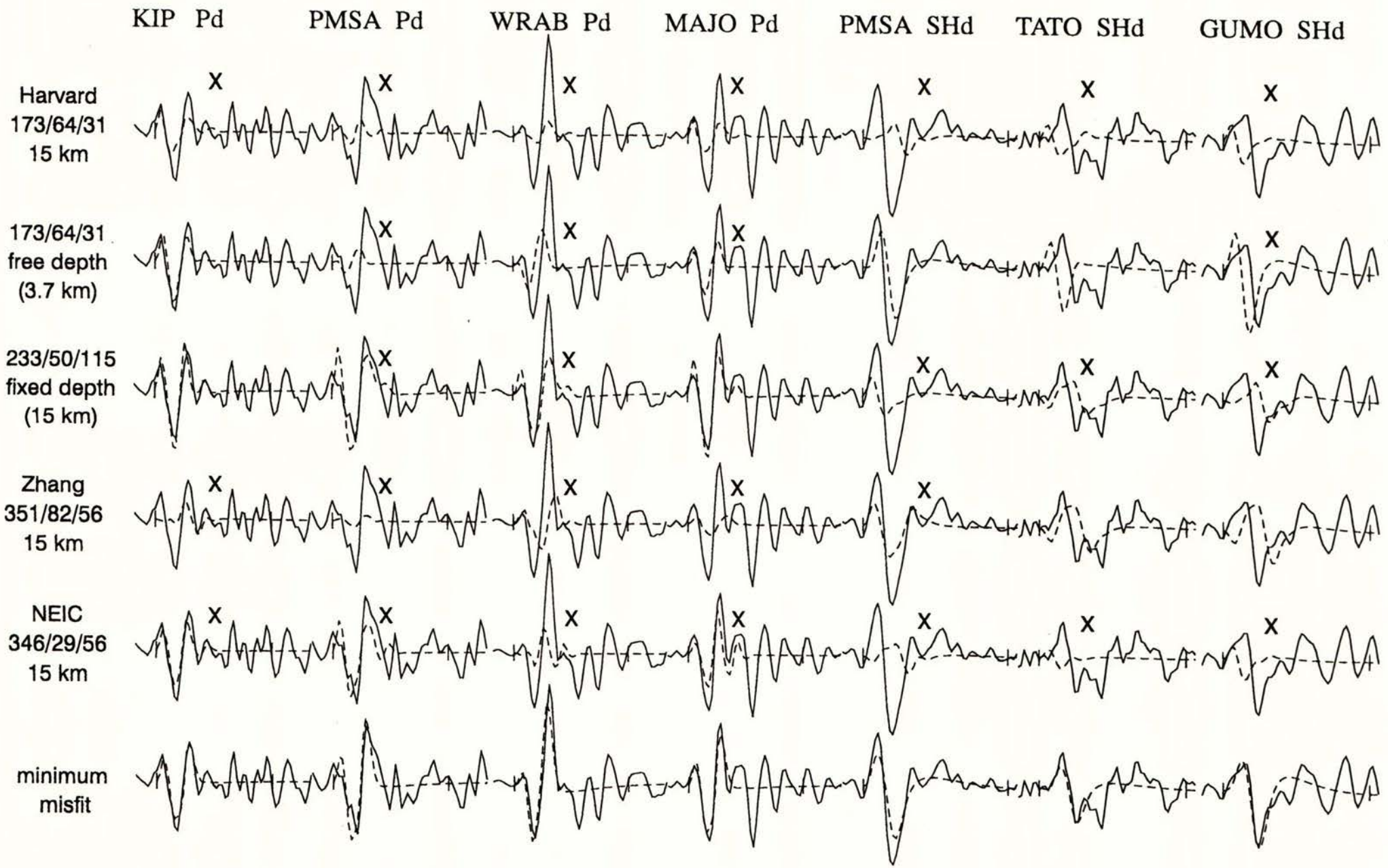
KIP Pd
PMSA Pd
WRAB Pd
MAJO Pd
PMSA SHd
TATO SHd
GUMO SHd
Harvard
173/64/31
15 km
173/64/31
free depth
(3.7 km)
233/50/115
fixed depth
(15 km)
Zhang
351/82/56
15 km
NEIC
346/29/56
15 km
minimum
misfit

Figure 5

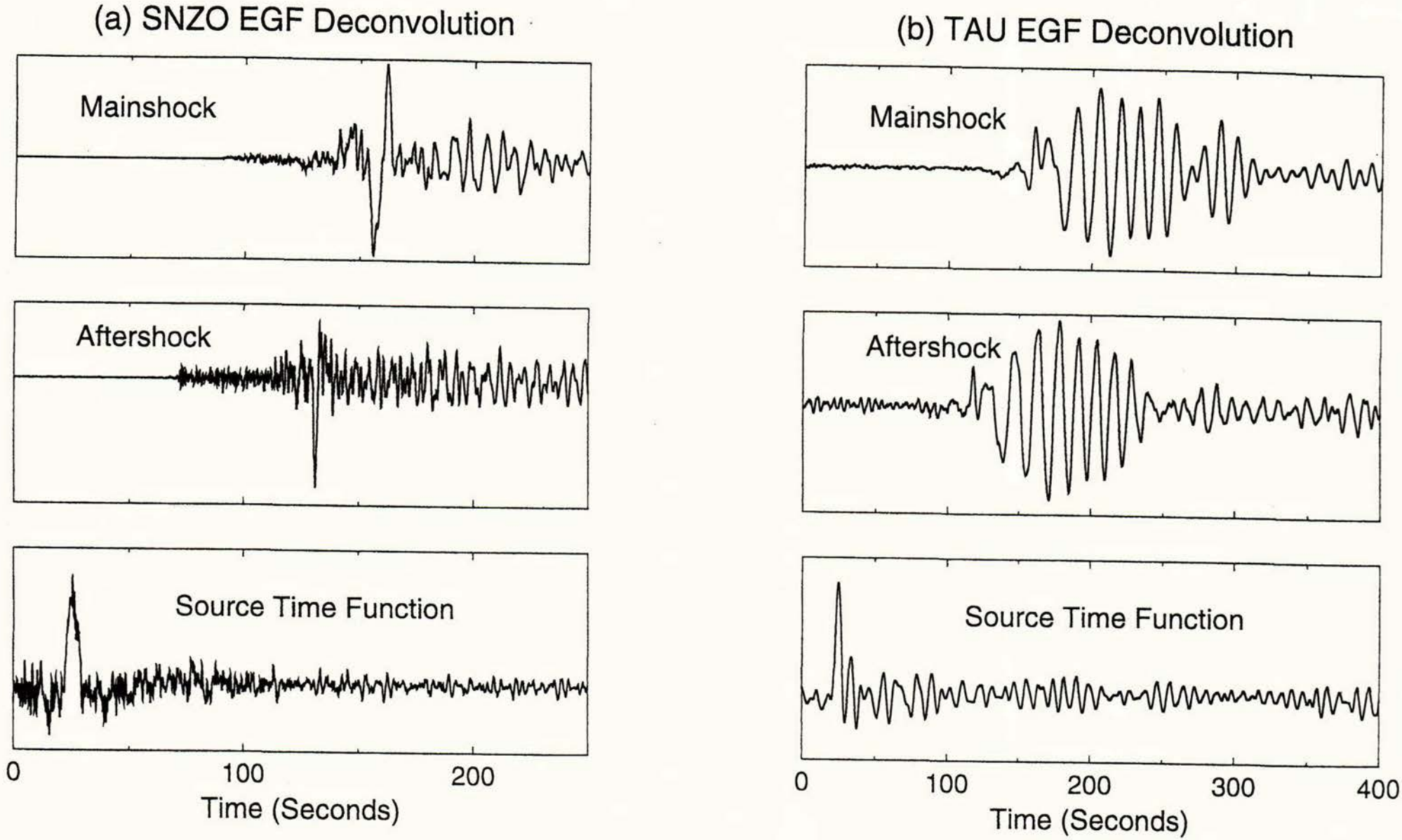
(a) SNZO EGF Deconvolution
Mainshock
Aftershock
Source Time Function
0
100
200
Time (Seconds)
(b) TAU EGF Deconvolution
Mainshock
Aftershock
Source Time Function
0
100
200
300
400
Time (Seconds)

Figure 6

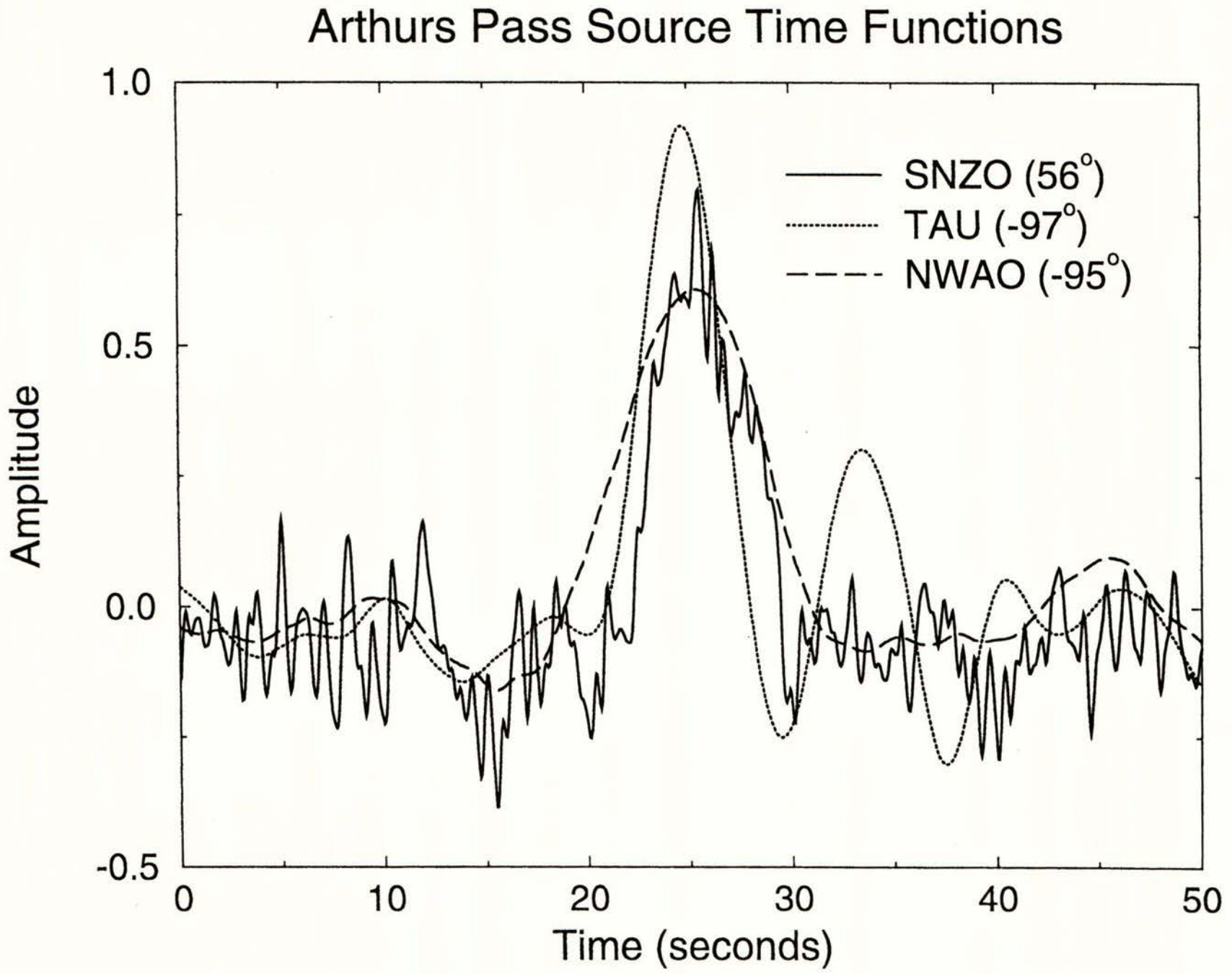
Arthurs Pass Source Time Functions
1.0
0.5
0.0
-0.5
Amplitude
0
10
20
30
40
50
Time (seconds)
SNZO (56°)
TAU (-97°)
NWAO (-95°)

Figure 7

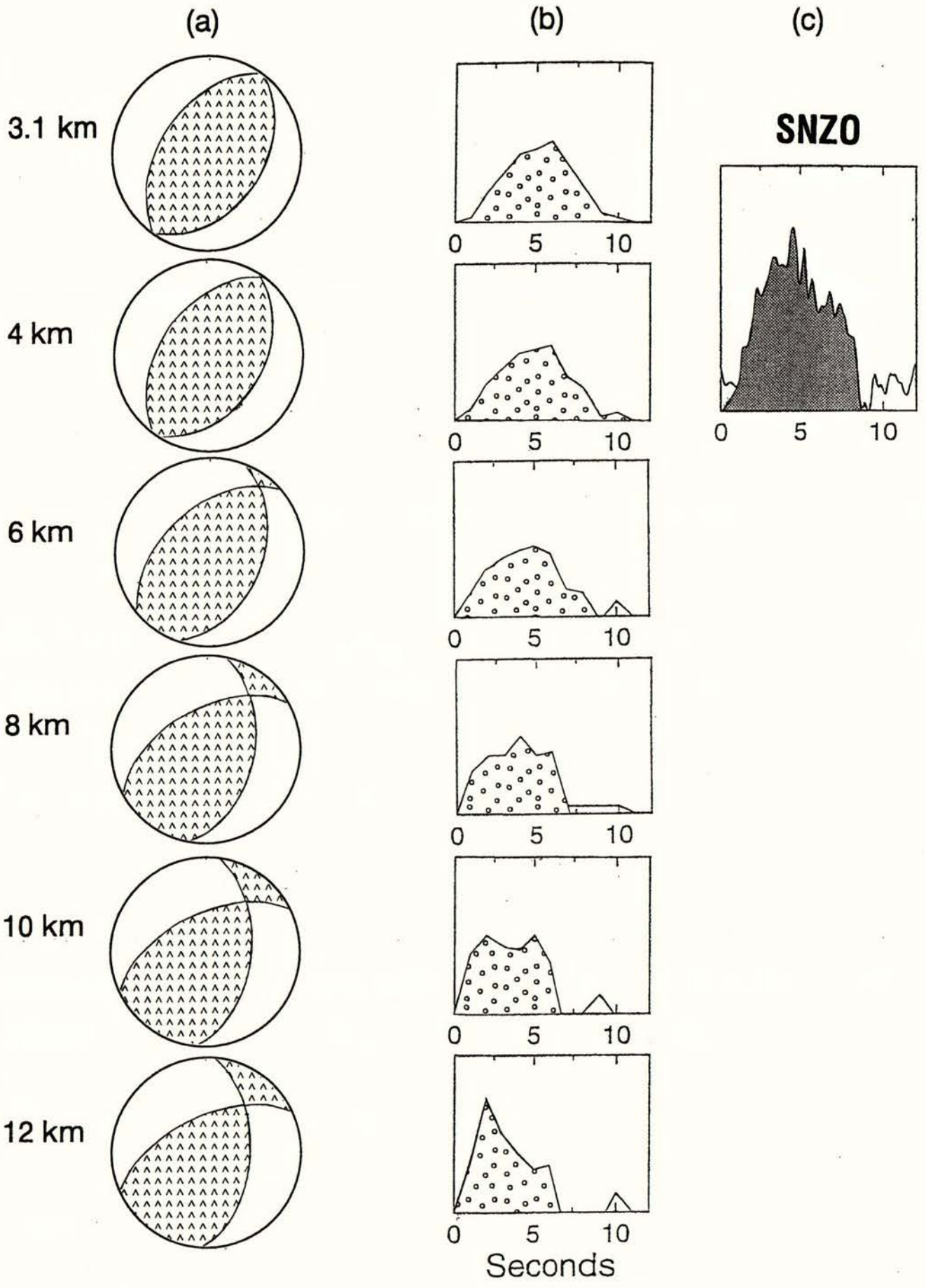

Figure 8

Arthurs Pass 94.06.19 Mw=5.9

253/87/178/8/5.798E17

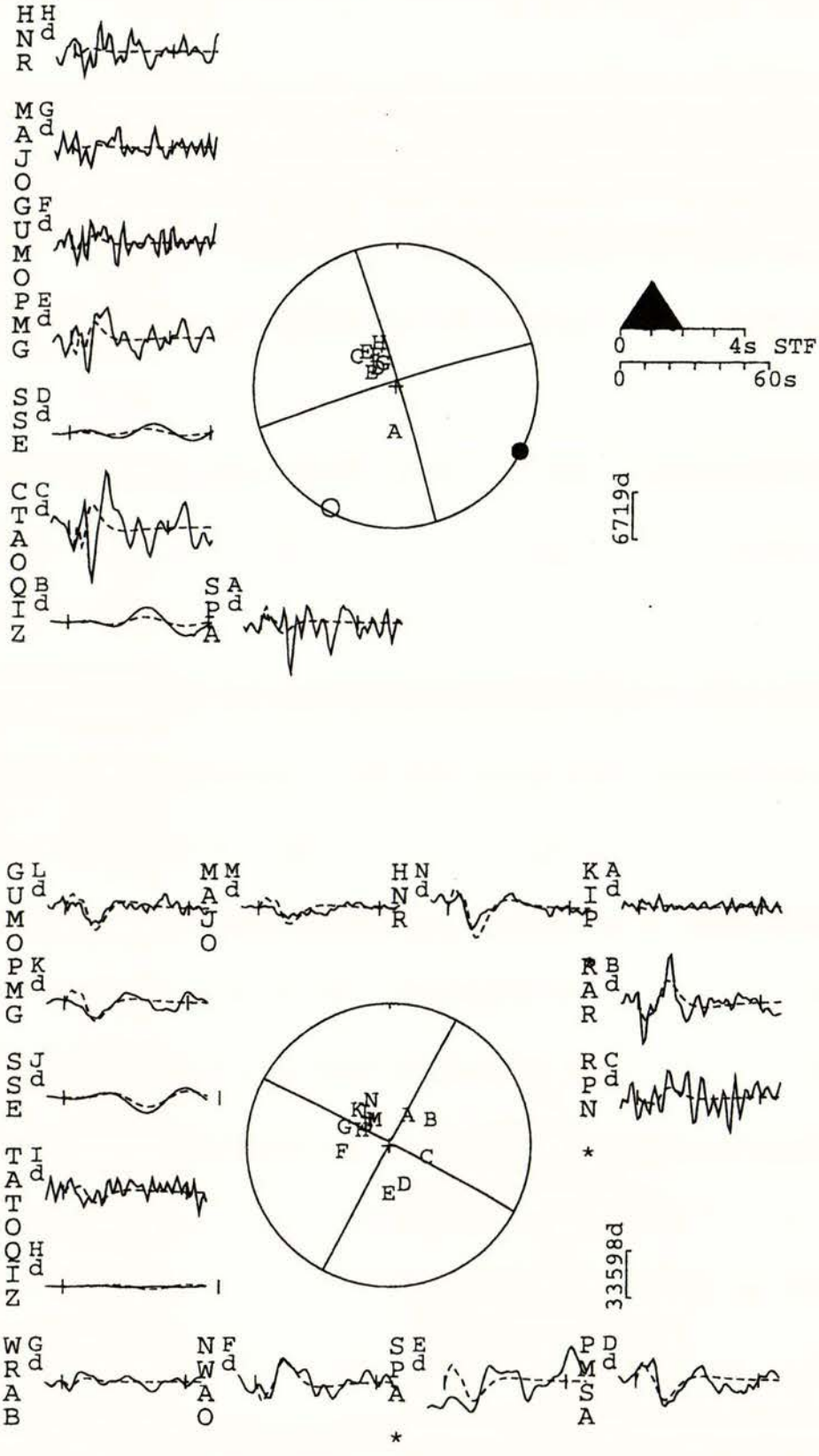

Figure 9

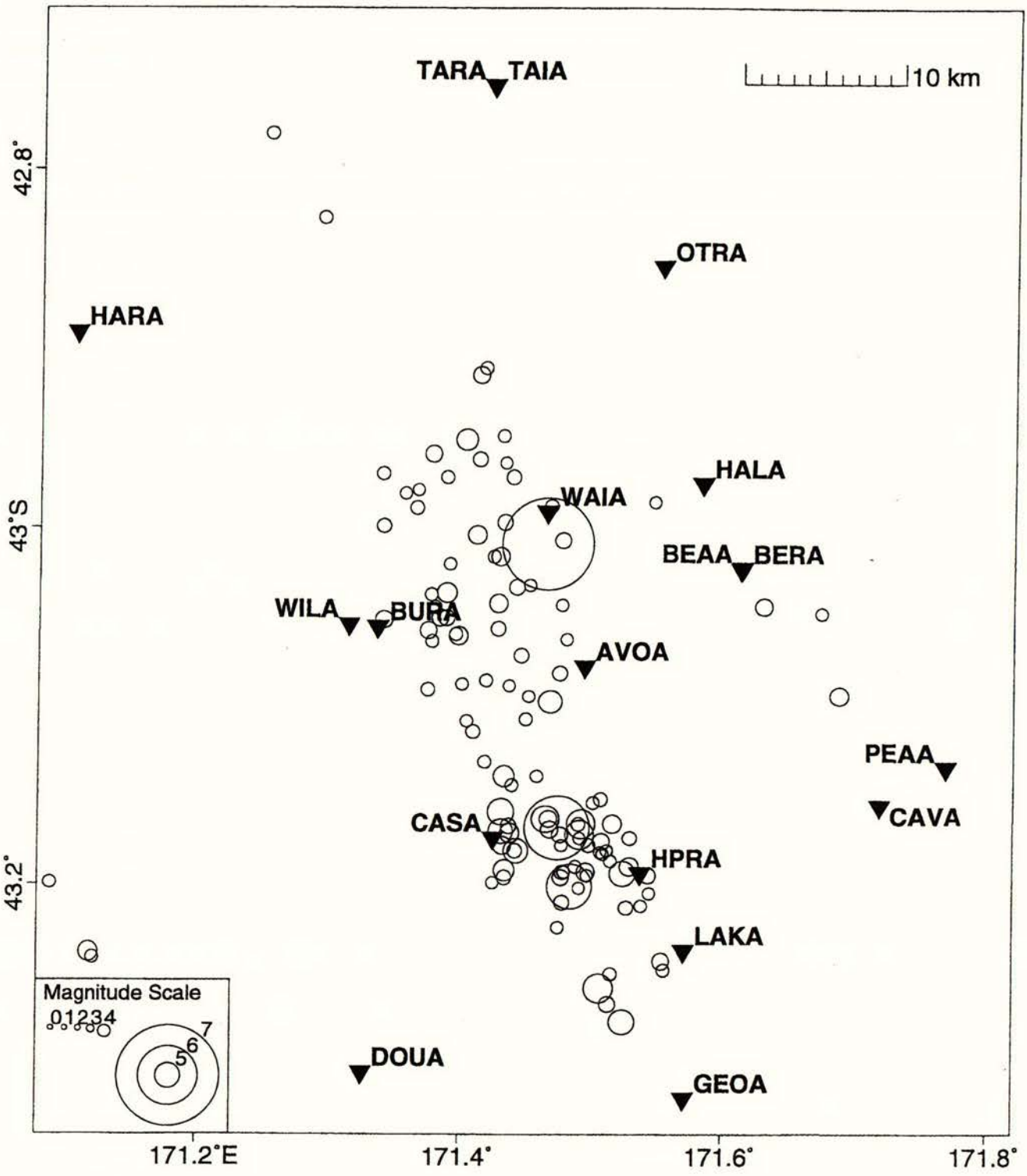
TARA
TAIA
10 km
42.8°
OTRA
HARA
HALA
WAIA
43°S
BEAA
BERA
WILA
BURA
AVOA
PEAA
CAVA
CASA
HPRA
43.2°
LAKA
Magnitude Scale
0 1 2 3 4
7
6
5
DOUA
GEOA
171.2°E
171.4°
171.6°
171.8°

Figure 10

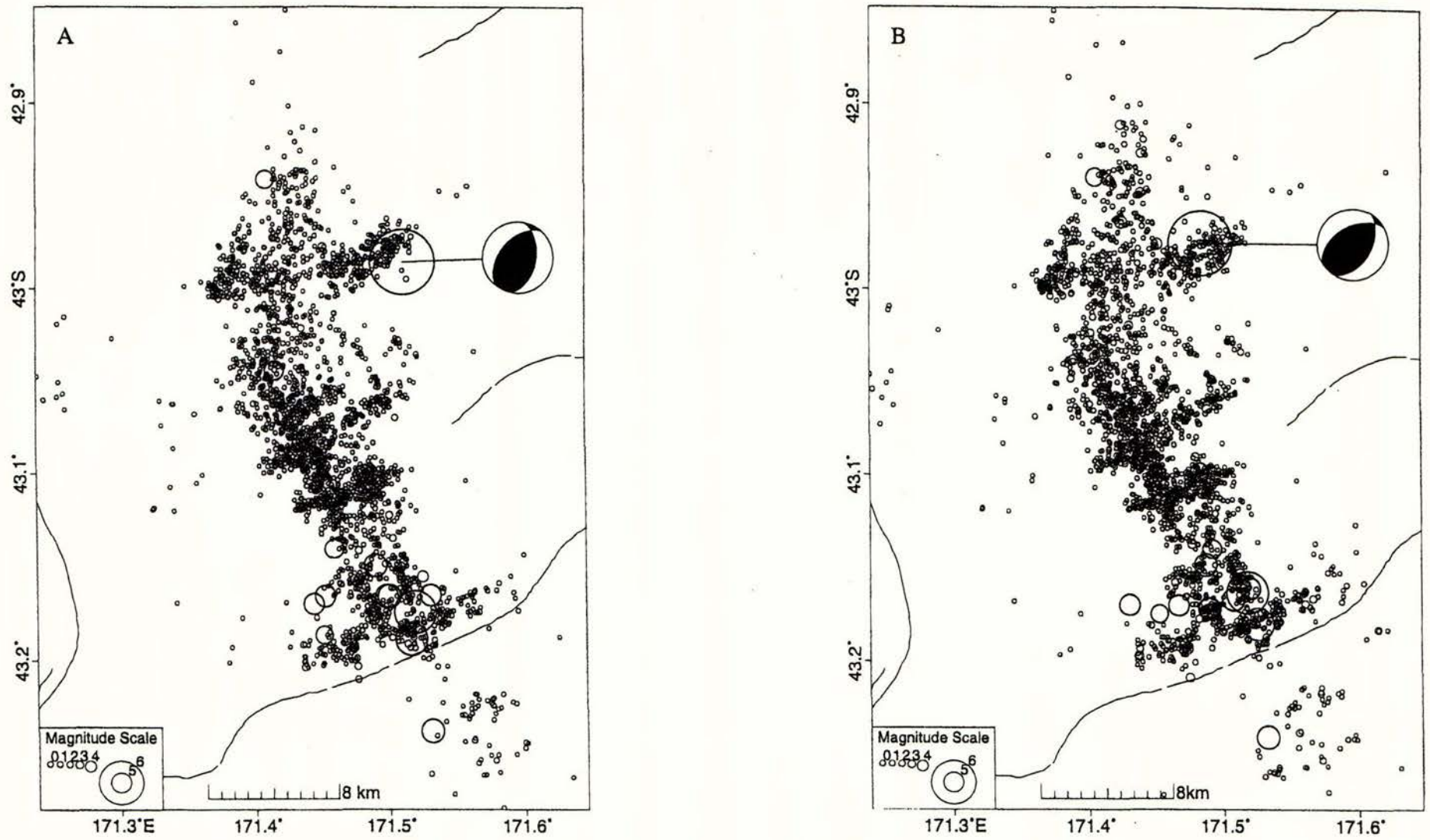
A
42.9°
43°S
43.1°
43.2°
Magnitude Scale
0 1 2 3 4
5
6
8 km
171.3°E
171.4°
171.5°
171.6°
B
42.9°
43°S
43.1°
43.2°
Magnitude Scale
0 1 2 3 4
5
6
8km
171.3°E
171.4°
171.5°
171.6°

Figure 11

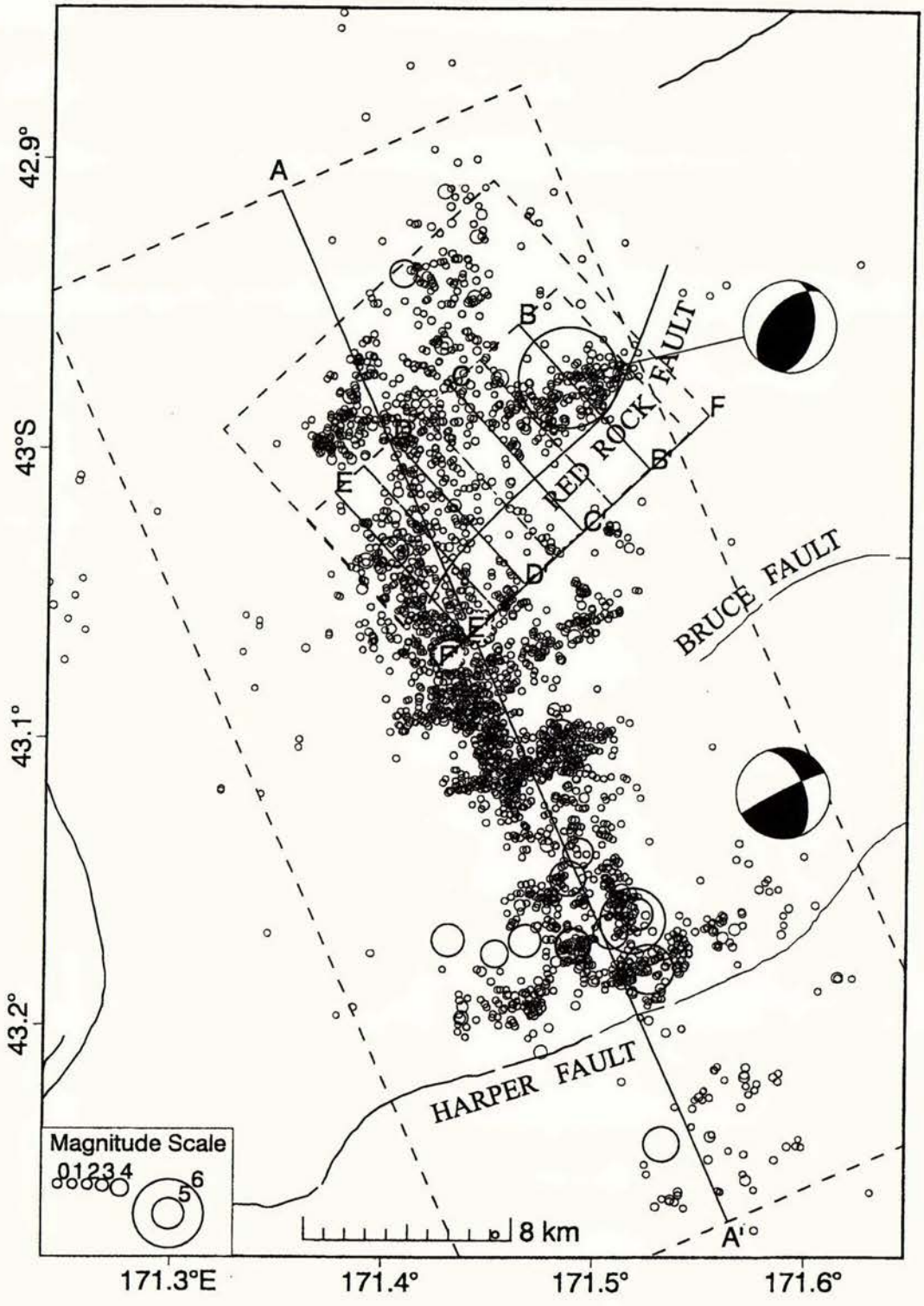
42.9°
43°S
43.1°
43.2°
171.3°E
171.4°
171.5°
171.6°
A
A'
B
C
D
E
F
RED ROCK FAULT
BRUCE FAULT
HARPER FAULT
Magnitude Scale
0 1 2 3 4
5
6
8 km

Figure 12

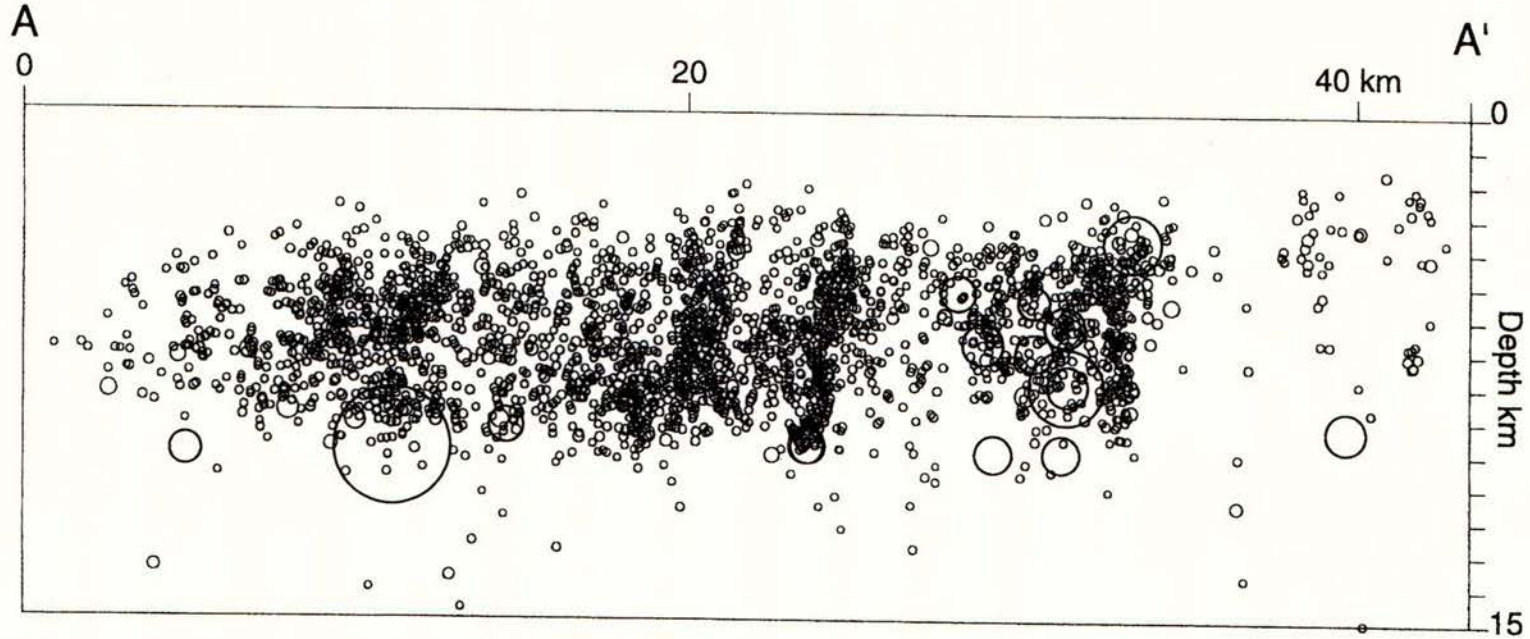

Figure 13

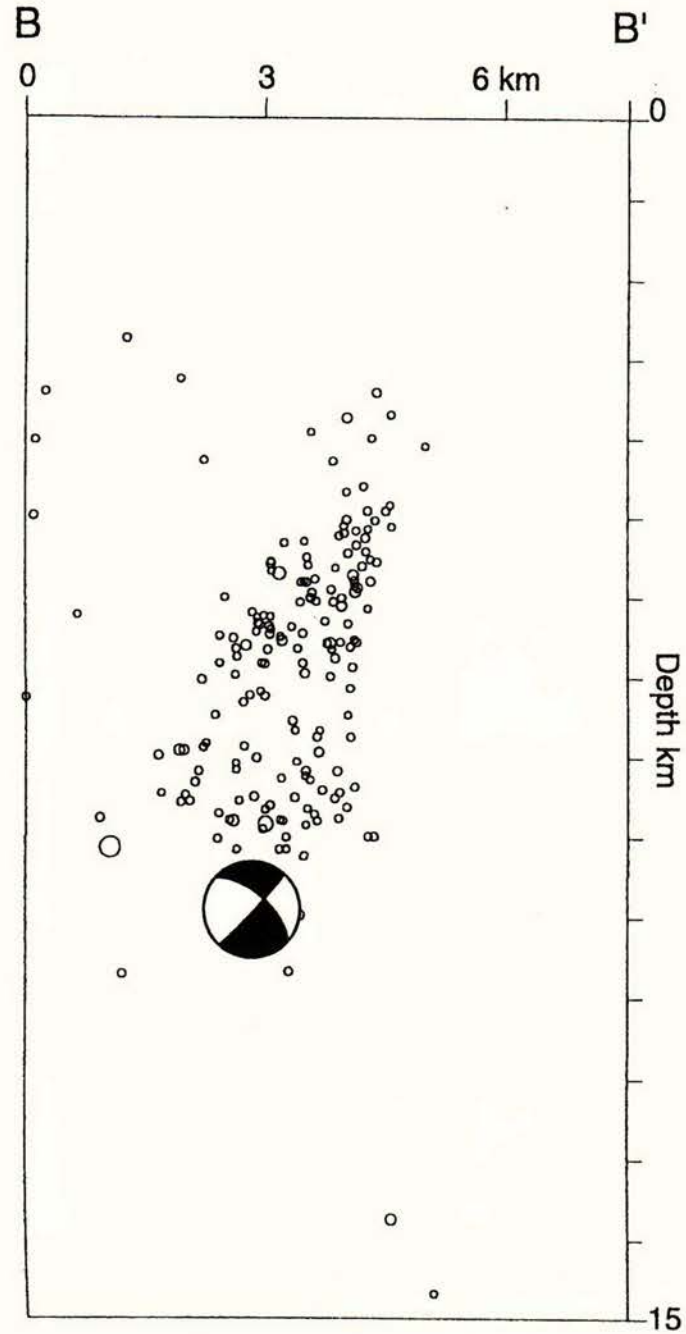

Figure 14a

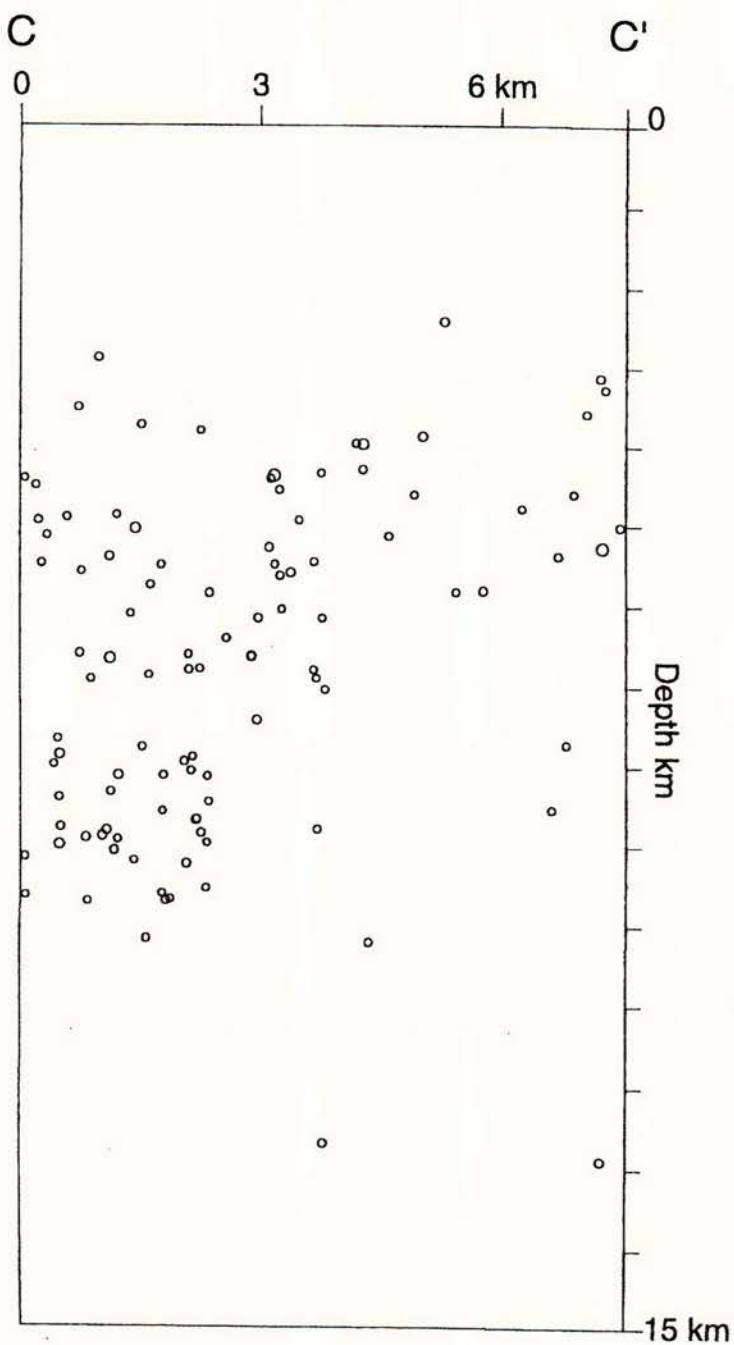

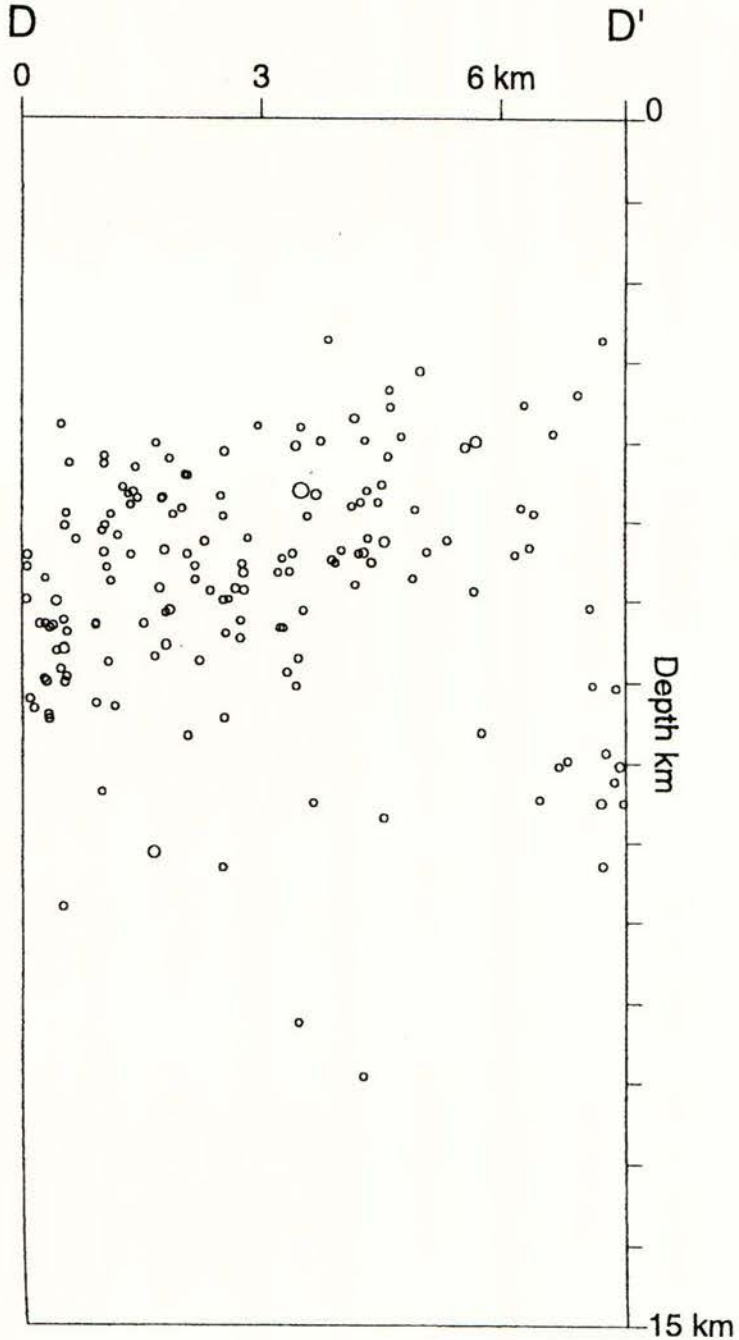

Figure 14b

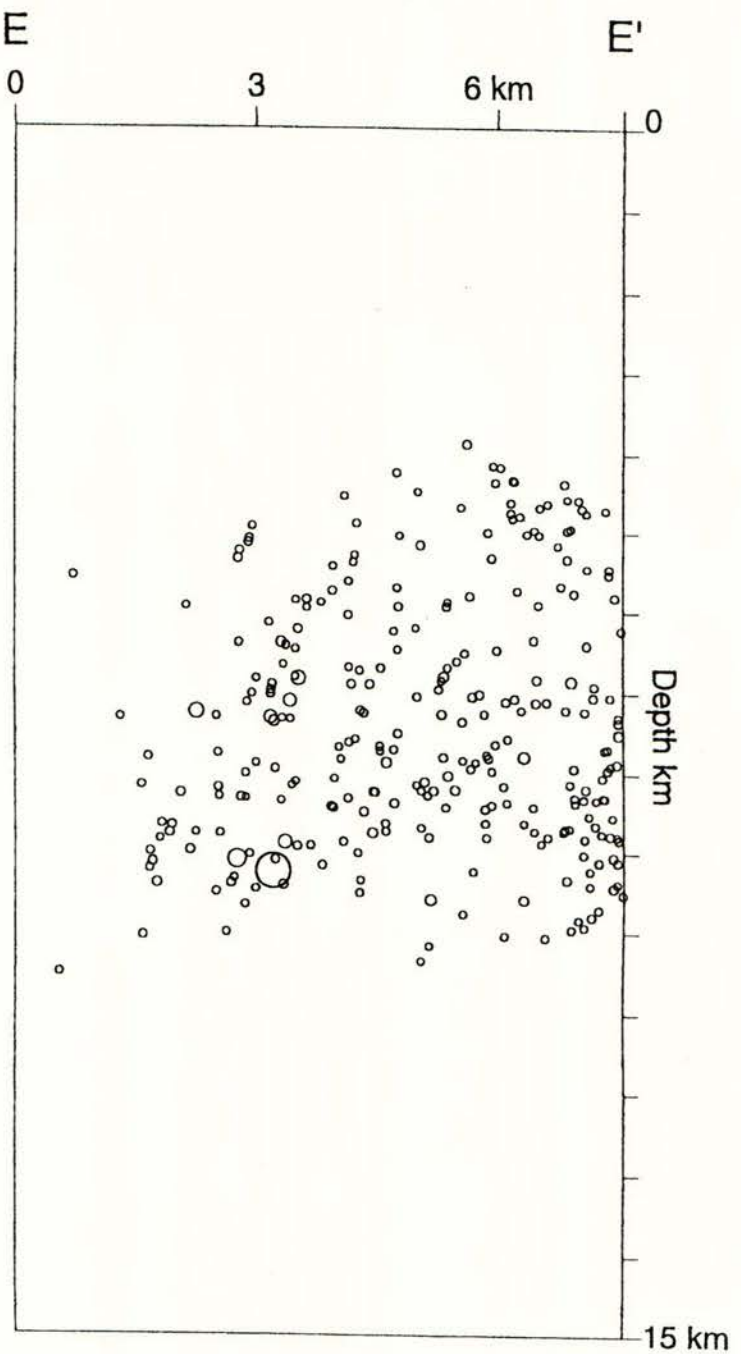

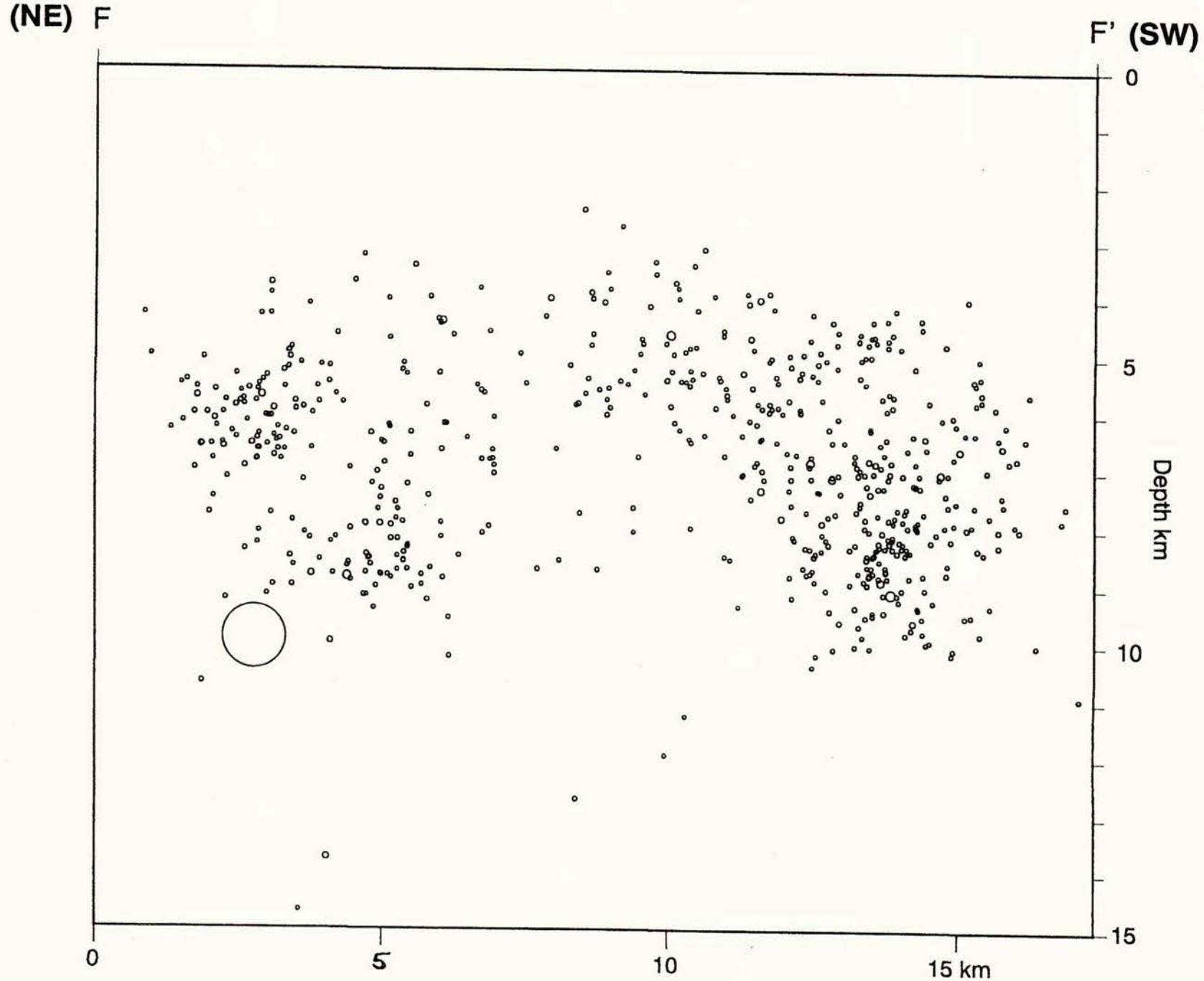

Figure 15

The Enigma of the Arthur's Pass, New Zealand, Earthquake, 2: The Aftershock Distribution and its Relation to Regional and Induced Stress Fields

Russell Robinson and Peter J. McGinty
Institute of Geological & Nuclear Sciences
Wellington, New Zealand

Abstract

The aftershock distribution of the 1994 Arthur's Pass earthquake, Mw 6.7, is unusual for a reverse faulting event in that it extends 12 km NNW and 30 km SSE of the actual fault plane, which strikes NE-SW. This is in marked contrast to the aftershocks of another reverse faulting event of much the same magnitude, the Northridge, California, earthquake. We have used several methods to infer the regional stress field in the region, including geodetic results, earthquake mechanisms, and inversion of P-wave polarity data for the stress tensor orientation. The inversion method is new, and does not require the focal mechanisms of the events used. It also incorporates the Coulomb failure criterion. All results point to a stress field favoring strike-slip faulting, not thrusting, with near horizontal $\sigma 1$ and $\sigma 3$ principal axes striking at 298° and 28°. The fault plane of the mainshock is not well oriented for reverse slip in this stress regime. Using dislocation theory we calculate the stress induced by the Arthur's Pass earthquake, and its largest aftershock (a strike-slip event), and add this to the regional field. Assuming that off-fault aftershocks will occur where the Coulomb Failure Stress (CFS) on optimally oriented planes is highest, we find a fair correspondence between the aftershock distribution and regions of high CFS. However, there are regions of high CFS that are devoid of aftershocks. It appears that earthquake slip in this region of oblique (19°) plate convergence is, as observed elsewhere, partitioned into components parallel and perpendicular to the plate margin. Most of the slip is parallel, as occurs on the nearby dextral Alpine Fault, the boundary between the Pacific and Australian plates. But occasional reverse events, such as the Arthur's Pass earthquake, account for at least some of the perpendicular component of slip, and the uplift that produced the Southern Alps. The 1995 Cass earthquake, Mw 6.2, 30 km to the east occurred near a peak in the induced CFS for a fault with its observed mechanism, a mix of reverse and strike-slip motion, and so can be classed as a triggered earthquake.

Introduction

The Arthur's Pass earthquake, Mw 6.7, 18 June 1994, occurred in the Southern Alps, South Island, New Zealand, a region of oblique continental collision. Although aftershocks range in depth from about 1 to 10 km, there was no surface rupture. The aftershocks have an unusual spatial distribution with respect to the mainshock fault plane and mechanism. The mainshock was primarily a reverse event centered at about 6 km depth on a fault striking NE-SW. However, the numerous aftershocks (largest M_L6.0) define an elongate region extending about 12 km NNW and 30 km SSE of the mainshock epicentre (Figure 1), well away from the presumed mainshock fault plane which is not well defined by the aftershocks. This is in contrast to the case for some other reverse events of similar size, such as the Northridge,

California, event of 1994, Mw 6.7. For the Northridge event most aftershocks fall within a few kilometres of the fault plane, although there is significant diffuse activity in the hanging wall (Mori et al., 1995). It is the purpose of this study to explain why the Arthur's Pass aftershocks are distributed as they are. The answer probably has significant implications for the local tectonics.

Details of the mainshock mechanism, modelling of GPS geodetic data, aftershock locations and statistics, and implications for seismic hazard estimation in New Zealand are discussed in a companion paper (Abercrombie et al., this volume).

Our approach to understanding the Arthur's Pass aftershock distribution is similar to that in several other studies (e.g., King et al., 1994). In the area around the Arthur's Pass event, there will have existed a "regional stress" beforehand, due to tectonic loading. Since the stress drop in a large earthquake is thought to be only about 10% or less (e.g., Scholz, 1990) the induced changes in stress due to the mainshock will not greatly alter the orientation of the regional stress except very near the fault plane. Aftershocks someway off the fault plane will preferentially occur in regions where the stresses induced by the mainshock have increased the Coulomb failure stress (CFS) on small faults optimally oriented in the combined regional (large) and induced (small) stress field. The reasoning is that in tectonically active regions there are numerous small faults with a wide range of orientations. Given some small change in stress due to slip in the mainshock, there will usually exist some faults oriented such that the maximum potential CFS is realized, and they will fail in preference to other less favourably oriented faults. Aftershocks on the mainshock fault plane will mostly have mechanisms similar to the mainshock, and arise due to variations in the amount of slip during the mainshock. A clear example of this situation is that of the on- and off-fault aftershocks of the 1984 Morgan Hill earthquake in California (Oppenheimer et al., 1988).

So if we wish to explain the distribution of off fault aftershocks for the Arthur's Pass earthquake we first need to know the orientations of the regional stress principal axes. The data from background seismicity in the region are not sufficient to infer the regional stress via inversion of focal mechanisms, so we use instead geodetic results and mechanisms or P-wave polarities for off-fault aftershocks to infer the regional stress tensor. The latter assumes that the stress perturbations due to the mainshock are small and variable in orientation throughout the region of the off-fault aftershocks. Once the regional stress tensor is defined, we then add the induced stress changes due to the Arthur's Pass mainshock, calculated using dislocation theory, and compare the spatial distribution of the aftershocks with the regions experiencing increased CFS on optimally oriented faults. We also calculate the CFS induced by the Arthur's Pass event on the fault plane of the Mw 6.2 1995 Cass earthquake (Gledhill et al., in preparation), 30 km to the west to see if the Arthur's Pass event could have acted as a trigger.

Regional Stress Tensor

Geodetic Results

Pearson et al. (1995) report on analyses of geodetic results along a 60 km profile across the central South Island that passes through the Arthur's Pass region. Their data consist of GPS observations made in 1992 and first-order triangulation/trilateration data from about 1978. The

azimuth (degrees east of north) of the axis of maximum horizontal contraction in the western and eastern halves of the profile are 287 +/- 6 and 296 +/- 9. The Arthur's Pass earthquake lies near the boundary, so we take 291.5° as an appropriate value. This is very close to the value (290°) they obtain from a dislocation model in which the NUVEL-1A plate convergence velocity is resolved onto a 50° dipping Alpine Fault locked to a depth of 12 km and freely slipping below that. The Alpine fault, 25 km to the NW of the Arthur's Pass epicentre, is the dominant active fault in the South Island, with cumulative strike-slip offsets of about 480 km and paleoseismic evidence of large earthquakes within the last 500 years (Berryman et al., 1992; Bull, 1998).

If we assume, as is commonly done, that one principal axis of stress is vertical and the other two horizontal, and take the azimuth of the most compressive principal axis of stress ($\sigma 1$) to be the same as that for the axis of maximum horizontal contraction (291.5°), then the stress tensor orientation is still ambiguous: the vertical principal axis could be either $\sigma 2$ or $\sigma 3$. Most of the active faults in the region, including the Alpine Fault, are dominantly strike-slip. suggesting $\sigma 2$ is vertical. On the other hand, the presence of the Southern Alps suggests uplift by reverse faulting, implying that $\sigma 3$ is vertical as would be appropriate for a reverse event such as the Arthur's Pass earthquake.

Aftershock Focal Mechanisms

All aftershock data used in this study are from the relocation of the Arthur's Pass aftershocks using a 3-dimensional (3D) velocity model, as described in Abercrombie et al. (this volume). Because the permanent New Zealand National Seismograph Network is sparse, we only consider events during the period of best coverage with temporary portable stations, 22 June through 2 July, 1994. Focal mechanisms of all such events with magnitudes 3.1 or more and location quality A or B (78 events) were obtained (Figure 2). The quality criteria are explained in Abercrombie et al. (this volume). The method used to obtain mechanisms makes use of P-wave polarities and the amplitude ratios of low-pass filtered P and S envelopes as described in Robinson & Webb (1996) and Reyners et al. (1997), making use of the original idea of Schwartz (1995). The use of amplitude ratios can often resolve ambiguities in mechanisms based on polarities when the number of observations is small, as is the case here (the average number of polarity observations for the events used is 13.3). An example is shown in Figure 3. All P-wave polarities were rechecked, and a few new readings added.

Considering the 57 events more than 2 km away from the inferred fault plane, there are a wide variety of aftershock mechanisms. But there are regularities (Figure 4): the P axes tend to be sub-horizontal and strike ESE or WNW and the T axes tend to be sub-horizontal and strike NNE or SSW. This pattern implies predominantly strike-slip faulting. We can be more quantitative if we consider the P and T axes as vectors rather than lines so that spherical means can be calculated (Davis, 1986). To do this we choose as the vector that end point of the axis which has an azimuth closest to 300° (for P) and 30° (for T). For example, a point in Figure 4a with azimuth 100° and dip 80° would be converted to the equivalent point with azimuth 280° and dip 100°. The mean direction of P then corresponds to an azimuth (clockwise from North) of 297.7° and dip (from the upward vertical) of 82.2°. The mean direction for T corresponds to an azimuth of 21.1° and dip of 84.4°. The standard deviations for P and T are 24.0° and 23.1°. Alternatively, we can find the lines around which the moments of inertia of the set of P or T axes are minimum: this requires no "flipping" as before. These lines have azimuths and dips of 293.6° , 82.6° for P, and 21.8°, 83.8° for T.

The average P axis azimuth is very close to that of the $\sigma 1$ stress axis inferred from geodetic results. Although the P, B, and T axes of an individual focal mechanism are not equivalent to the stress principal axes, when averaged over many diverse events they should be similar. This suggests that a regional stress tensor with a horizontal $\sigma 1$ axis, azimuth 295°, a horizontal $\sigma 3$ axis, azimuth 25°, and a vertical $\sigma 2$ axis would be appropriate (all σ must be orthogonal).

Inversion of Polarity Data

There are several methods of inverting focal mechanisms for the stress tensor (e.g., Gephart & Forsyth, 1984; Michael, 1984; Rivera & Cisternas, 1990; Horiuchi et al., 1995). For several reasons we have used our own inversion method, described below. The first reason is that none of the above methods invoke the Coulomb failure criterion, which will be the underpinning assumption we use later to (hopefully) explain the distribution of aftershocks. The second has to do with the estimation of confidence limits. We originally intended to use the method (and computer code) of Horiuchi et al. (1995), but that method does not give estimates of the confidence limits. Zhao et al. (1997) used this method but added the resampling technique (Michael, 1987) to estimate the confidence limits. However, the amount of computer time is excessive, especially if fine resolution of the parameters and 95% confidence limits are desired. The method is essentially a grid search procedure over the orientation of the principal axes of stress (3 parameters), and the shape of the stress ellipsoid as defined by $R=(\sigma 1-\sigma 2)/(\sigma 1-\sigma 3)$, under the requirement that slip direction in the fault plane be parallel to the direction of maximum shear stress.. The quantity minimized is the number of incorrect P-wave polarities. One inversion of 57 mechanisms, with 5° resolution in the stress axes orientation, takes about 18 hours on the fastest computer available to us. We estimate that at least 500 resamples would be required to obtain stable confidence limits at the 95% level, over a year of computer time. Finally, the method of Horiuchi et al. (1995) works best when the polarity data are sufficient to closely constrain the nodal planes. Although our individual event mechanisms are well constrained when using the combined polarity and amplitude ratio data, some are not well constrained using polarity data alone.

For these reasons we have developed our own inversion method. In our method we consider all polarity observations together, regardless of whether or not they are sufficient to define single event focal mechanisms. We search over a range of stress axes orientations defined by $\sigma 1$ azimuth and dip, and $\sigma 3$ azimuth. These parameters are sufficient to define the two planes with maximum Coulomb failure stress and the direction of maximum shear stress on them, assuming a coefficient of friction. These planes are independent of the shape of the stress ellipsoid (Harmsen & Rogers, 1986) and of the pore pressure. We assume that the aftershocks will occur mostly on faults with orientations clustered about one or other of these optimal planes and that slip will be in the direction of maximum shear stress. For all events together, we simply count the number of polarities for which observation and prediction are the same, and take as the best stress orientation that which maximizes this count. The search procedure is done in two steps, the first with a coarse resolution (10°) and the second with a finer resolution (2°) centered around the result of the first step and with a maximum deviation in the $\sigma 1$ and $\sigma 3$ azimuths and dips of +/-20°. During the first coarse search we retain in memory the correctness of each polarity for all possible stress tensors (about 6.5 Mbyte/1000 observations). We then do all the coarse search resampling and store the lists of observations used, and the results, in a (large) disk file. Because of the data stored in memory this is

relatively quick. Then memory is cleared and all the fine searches are done referring to the data on disk, but this is relatively slow because each resample searches over a different set of stress axes and it does little good to save anything in memory. Error estimates (95% confidence limits) for our inversion technique are obtained by the resampling method. We find that for a data set of 1000 or more polarities, that 500 resamples are sufficient for the confidence limits to be stable to within 2 degrees (see below). This number of resamples consumes about 6 hours of computer time for 1000 observations.

As mentioned above, it is necessary to assume a coefficient of friction, μ, which defines the angle between the principal compressive stress $\sigma 1$ and the two planes with maximum CFS. But μ cannot be included as a parameter in the inversion because as μ becomes large the compression (or dilation) quadrants of the two possible focal mechanisms have less and less area in common (i.e., it becomes more likely that if a polarity cannot be reproduced by one focal plane than it will be reproduced by the other). So if μ is included in the inversion then large values are unreasonably favoured. In all our work we have taken μ as 0.75, midway between the value of 0.7 in the KTB ultra-deep borehole (Brudy et al., 1997) and the value of 0.8 found from induced seismicity studies in Colorado (Raleigh et al, 1972). Oppenheimer et al. (1988) also used a value of 0.75 to explain the aftershock distribution of the Morgan Hill, California, earthquake.

It might seem that our inversion method is little more than the old practice of "composite mechanisms", but it differs in that we are solving for the stress axes (not strain), that the Coulomb failure criterion is incorporated, and that the two fault planes are non-orthogonal. If μ were taken as 0.0, then the methods would be essentially the same, but that seems unreasonable (recall μ is the dry coefficient of friction, and a possibly high pore pressure leading to a low effective coefficient does not enter into the calculations).

The ability of our method to retrieve the regional stress tensor has been tested in several ways with sets of artificial data. We set the "real" regional $\sigma 1$ azimuth and dip to 296° and 80°; the $\sigma 3$ azimuth and dip were 26° and 90°. Given these, the two optimal fault planes, and rakes, are determined for a coefficient of friction of 0.75. For realism, all sets of test data make use of real Arthur's Pass hypocentres, station locations, and which station recorded a polarity for which event. There were 460 events and 4012 polarities. For all tests the fault plane for a given event was one of the two optimal planes, chosen randomly, and the expected polarities calculated from that. The test was then to see if the inversion method could find the correct $\sigma 1$ and $\sigma 3$ orientations for this noise free data. The result (Table 1) was that it could, with no error. All resamples produced the same "best" $\sigma 1$ and $\sigma 3$ axes. The second test was to add three types of noise: 1) fault planes deviate from the optimal (deviations in strike, dip, and rake chosen randomly from a Gaussian distribution with zero mean and 15° standard deviation); 2) events could be mislocated, resulting in incorrect azimuths and take-off angles (latitude and longitude errors chosen randomly from a Gaussian distribution with standard deviation 0.5 km; similarly for depth but with a standard deviation of 1.0 km); and 3) 5% of the polarities were reversed. The distribution of event mechanism P and T axes for this artificial data (Figure 5) is similar to that for the 57 real focal mechanisms, except that the few real axes with dips tending towards vertical are not reproduced. The retrieved $\sigma 1$ and $\sigma 3$ axes for this noisy artificial data (Table 1) were quite close to the "real" $\sigma 1$ and $\sigma 3$ axes. The best result explains 90.6% of the polarities; the worst explains 48.4%.

The next test was to assume an incorrect coefficient of friction (0.60 rather than 0.75) in the

inversion of the noisy data. Again (Table 1) the retrieved parameters are close to the "real" values. The next test was to use a regional stress that varied from north to south, the σ1 and σ3 azimuths rotating 20° clockwise from 15 km north of the mainshock epicentre to 30 km south of it. Other noise sources were introduced as above, except that the coefficient of friction was correct. The result is again quite good (Table 1).

Table 1: Tests of the stress tensor inversion method.

	σ_1 azimuth	σ_1 dip	σ_3 azimuth	σ_3 dip	% correct
real	296	80	26	90	-
noise free	296 +/-0	80 +/-0	26 +/-0	90 +/-0	100.0
noisy data	298 +4 -0	84 +2 -12	28 +4 -0	90 +0 -0	90.6
noisy data; wrong μ	298 +4 -4	80 +6 -10	28 +4 -4	90 +11 -8	88.9
noisy data; σ variable	300 +4 -4	78 +14 -8	30 +4 -4	90 +14 -6	91.7

Errors (95% confidence limits) are based on 500 resamples of the 4012 observations.

We have also redone the "noisy data" test for smaller numbers of data, taking the first 250, 500, 1000, 2000, and 3000 observations. The results (Figure 6, Table 2) indicate that about 500 observations are required for a minimally useful result, one that distinguishes between stress tensors for predominantly reverse, normal, or strike-slip faulting. We expect that this result depends on a fairly good distribution in azimuth and take-off angle. In Figure 6 the 95% confidence limits are indicted by plotting the σ1 and σ3 axes resulting from the 95% best resamples (best = closest to the original result); they are usually not symetric about the original result. The number of resamples for a stable (within 2°) 95% confidence estimate is about 500 for 1000 or more observations, but increases for fewer observations. For 500 observations the number is about 1000. For 250 observations it doesn't seem possible to get a stable estimate of the confidence limits; those shown in Figure 6 are from 1000 resamples.

Table2: Test results with varyiung numbers of observations.

Number of Observations	σ1 azimuth	σ1 dip	σ3 azimuth	σ3 dip
(real values)	296	80	26	90
3000	298 +4 -2	84 +12 -12	28 +4 -2	90 + 14 - 11
2000	298 +8 -6	74 + 24 -12	28 + 6 - 8	90 + 20 - 14
1000	298 + 9 -12	82 +24 -28	28 +10 -12	90 +26 -14
500	292 +18 -12	96 +42 -40	22 +16 -18	90 + 45 -26
250	298 +46 -28	68 +98 -28	30 +88 -86	85 +76 -65

To apply our inversion method to the real data we have used P-wave polarities for aftershocks during the period of best coverage with portable instruments, restricting the events to quality A locations (see Abercrombie et al. (this volume) for information on quality assessment) with 8 or more polarity observations. We have excluded events within 2 km of the inferred mainshock fault plane. This results in 3808 observations from 385 events. The results (Figure 7, Table 3) indicate horizontal, or nearly so, σ1 and σ3 axes. The best stress tensor explains 93.4% of the polarity observations, while the worst explains 41.7%. This orientation of the regional stress tensor is quite close to that inferred above from geodetic and focal mechanism data.

Table 3: Results of the stress tensor inversion.

	Azimuth, deg.	**Dip, deg.**
σ1	298.0	80.0
σ3	28.0	90.0

Magnitude of the Stresses

In addition to the orientation of the stress tensor we also need to know the magnitude of the deviatoric stress, at least roughly. This determines how much the stresses induced by the mainshock can alter the regional stress tensor orientation. One way to estimate this would be to calculate the deviatoric stress required for slip in the mainshock, given the orientation. This requires estimates of the lithostatic and pore pressures as well. Taking reasonable values for these (from a density of 2.65 x 10^3 kg/m^3 and a hydrostatic pore pressure) we get a value of 1490 MPa (14,900 bars) at 5 km depth, and that seems much too high. This is because the mainshock fault plane is poorly oriented for reverse slip in the regional stress field (a point we will discuss more later). Instead we have adopted values observed in the KTB ultra-deep borehole, i.e., 100 MPa (1000 bars) at 5 km depth (Brudy et al., 1997). This is close to the theoretical value assuming the crust is at a near critical level of stress. It is sufficiently high that the strike, dip, or rake of optimally oriented fault planes are rotated by only about 5° to 10° at a distance of 2 km from the Arthur's Pass fault plane.

Induced Changes in Coulomb Failure Stress

We have used the method of Okada (1992) to calculate the strains, and their derivatives, in a homogeneous half-space due to slip on a rectangular fault. These strains can be converted to stresses (using a rigidity of 2.68 x 10^{10} Nm^{-2}) and rotated to whatever coordinate system required. Once the induced stresses are known, we can add them to the regional stress tensor. Then we calculate the optimally oriented fault planes in that combined stress field. Then we can rotate the induced stress onto those faults, calculate the induced Coulomb failure stress, and examine its spatial variations. The induced Coulomb failure stress, δCFS, is given by

$$\delta CFS = \delta\tau_{shear} + \mu(\delta\tau_n + \delta P) \qquad (1)$$

where μ is the coefficient of friction, $\delta\tau_{shear}$ is the induced change in shear stress, $\delta\tau_n$ is the induced change in normal stress, and δP is the induced change in pore pressure. The last is given by

$$\delta P = -\frac{\beta}{3}\Sigma\delta\tau_{ii} \qquad (2)$$

where β is Skempton's coefficient. Our sign convention is that tensile stresses are positive, but we retain the common usage of "pressure" (compression is positive). The change in shear stress is positive if its direction is within +/- 90° of the rake in an "optimum event", otherwise negative. Also, we weight it by the cosine of the difference between the optimum rake and the direction of the induced shear stress. This avoids sharp positive to negative transitions. In some studies equation (1) is replaced by

$$\delta CFS = \delta\tau_{shear} + \tilde{\mu}(\delta\tau_n) \quad (3)$$

where $\tilde{\mu} = \mu(1 - \beta)$. This assumes that τ_{ii} is the same for all i, which may be the case very near major faults like the San Andreas (Rice, 1992). However we do not believe it is appropriate for the small faults responsible for most of the Arthur's Pass aftershocks and retain equation (1). In all our work we take $\mu = 0.75$ and β=0.5; the patterns of induced δCFS are fairly insensitive to these parameters.

The mainshock moment was taken as that given in Abercrombie et al (this volume), i.e. 1.3×10^{19} N-m (Mw 6.7). The average slip was calculated from this and the fault dimensions. Instead of taking a uniform slip distribution, we applied a linear taper from a maximum at the center to zero at the edges. This was done by subdividing the fault into 20 x 20 equally sized patches. There is no information available on the actual slip distribution. The average slip over the fault plane is 2.85 m, as implied by the moment, and the maximum is 3.80 m. These are somewhat high for an event of magnitude 6.7, but we cannot reasonably take the fault plane any larger. The implication is that the stress drop is high, as is often the case in New Zealand (E. Smith, pers.comm.).

The mainshock fault plane orientation and sense of slip used were those adopted in Abercrombie et al. (this volume), i.e. strike 221°, dip 47°, rake 112°. Because the largest aftershock was fairly large (M6.0), situated in the southern part of the aftershock zone, and occurred before the installation of portable seismographs, we have also included its induced stress field using the mechanism determined by inversion of teleseismic body waves (Abercrombie et al., this volume). It was a strike-slip event (more consistent with the regional stress field than the mainshock itself), and we have chosen the ENE striking nodal plane as the fault plane. The fault plane was taken as 8 x 8 km.

The regional stress field used was that obtained by our inversion method, as given in Table 3.

The distribution of induced changes in CFS (Figure 8) is computed at 5 km depth. The aftershocks superimposed are those that fall within the 4-6 km depth range and are 2 or more km away from the mainshock fault plane. Most of the off-fault aftershocks occurred in regions of positive induced CFS and few in negative regions. The exception is a cluster of events west of the center of the fault, some of which lie near the edge the lobe of negative induced CFS. Varying the distribution of slip might remedy this because of the proximity to the fault plane. Still, at longer distances the region of aftershocks SSE of the mainshock fault plane are well explained, as well as those to the north.

We have also calculated the induced δCFS on the fault plane of the 1995 Cass earthquake, M6.2, 30 km east of the Arthur's Pass event. We have used the Cass focal mechanism given in Gledhill et al. (in preparation): strike 176°, dip 46°, rake 44°. The results (Figure 9) show that the Cass hypocentre was close to a relative maximum in δCFS.

Discussion

We think that the unusual distribution of aftershocks for the Arthur's Pass earthquake can be

explained by the combination of the mainshock mechanism and the regional stress field. One remaining question is why the orientation of the mainshock fault plane and slip direction are inconsistent with the regional stress field. Aside from the observation that alps are created by vertical motion, it is often observed in regions of oblique plate convergence that seismic slip is partitioned into events with slip parallel to the plate boundary and with slip perpendicular to that (e.g., Yu et al., 1993). The resultant total slip is in the direction of convergence. This is the case for the subduction margin of the east coast of the North Island, New Zealand (Webb & Anderson, in press). Pearson et al. (1995) attempted to model their geodetic observations in the central Southern Alps with a dislocation model in which the NUVEL-1A plate convergence velocity is resolved onto a 50° dipping Alpine Fault locked to a depth of 12 km and freely slipping below that. They found that the predicted shear strain parallel to the Alpine fault agreed with their observations, but that the predicted shear strain perpendicular to the fault did not agree, even roughly. They inferred that the Alpine Fault takes up a large fraction of the component of plate convergence parallel to the plate boundary (i.e., to the Alpine Fault), but that the component normal to the boundary must be taken up elsewhere. It seems that the fault responsible for the Arthur's Pass earthquake is part of that "elsewhere". Since the obliqueness is not large (18°), we would expect earthquakes like the Arthur's Pass event to be relatively rare. We do not fully understand the mechanism of slip partitioning, and are somewhat reluctant to assume that the Arthur's Pass event is the rare event we just happened to observe by chance, but have no better explanation.

Another question is why the mainshock fault plane is not well defined by aftershocks. One explanation is that the stress drop was both high (as observed) and quite smooth, with little residual slip heterogeneity. It is often assumed that aftershocks on or very near the mainshock fault plane are due to variations in the amount of mainshock slip, leading to residual stresses favouring aftershocks with mechanisms similar to the mainshock (e.g., Oppenheimer et al., 1988).

The near equivalence of the average P and T axes of the individual event focal mechanisms with the $\sigma 1$ and $\sigma 3$ stress axes derived via our inversion method is consistent with the assumptions in that method, i.e. that slip will occur on either of the two optimally oriented planes chosen more-or-less randomly and with random deviations. The two optimal planes are symmetric about the $\sigma 1$ axis, so an average P axis would be expected to be close to the $\sigma 1$ axis.

It reasonable to say that the Cass earthquake was triggered by the Arthur's Pass event (Figure 9). The maximum induced δCFS was about 0.025 MPa (0.25 bars), which seems small in relation to the stress drop (about 5 MPa or 50 bars), but changes in δCFS as small as 0.1 bar have been found to produce observable changes in low level seismicity (Reasenberg & Simpson, 1992) and to effect aftershock distributions (King et al., 1994). But this does not mean that the Cass earthquake could have been forecast, since the δCFS depends on the fault orientation and sense of slip, which were not known ahead of time. Also, the pre-existing stress would have had to be fairly high for such a small change to act as a trigger. If the mechanism of future events is assumed, then it is possible to calculate the cumulative effect of the stresses induced by large past earthquakes (if their mechanisms are known) and look for regions where the CFS is high. This approach has produced good results in southern California, at least in retrospect (Deng & Sykes, 1997), and we hope to apply it the the Arthur's Pass and other New Zealand regions in future work.

Acknowledgements

We thank S. Horiuchi and Y. Okada for making their computer programs available to us. Martin Reyners, Terry Webb, John Beavan, and Kathleen Hodgkinson have reviewed the text and made useful suggestions for improving it.

References

Abercrombie, R., T. Webb, R. Robinson, P.J. McGinty, J.J. Mori, M.E. Reyners, and R.J. Beavan, 1998. The enigma of the Arthur's Pass, New Zealand, earthquake, 1: Reconciliation of incompatible geophysical observations. This volume.

Berryman, KR., S. Beanland, A.F. Cooper, H.N. Cutten, R.J. Norris, and P.R. Wood, 1992 The Alpine fault, New Zealand: variation in Quaternary structural style and geomorphic expression. Annales Tectonicae, Supplement to Volume VI, 126-163.

Brudy, M., M.D. Zoback, K. Fuchs, F. Rummel, and J. Baumgartner, 1997. Estimation of the complete stress tensor to 8 km depth in the KTB scientific drill holes: Implications for crustal strength. Jl. Geophys. Res., 102, 18453-18475.

Bull, W....1998. (paper in Jan 98 GSA Bulletin)

Davis, J.C., 1986. Statistics and Data Analysis in Geology. J. Wiley & Sons, Inc.

Deng, J. and L.R. Sykes, 1997. Evolution of the stress field in southern California and triggering of moderate-size earthquakes: A 200-year perspective. Jl. Geophys. Res., 102, 9859-9886.

Gephart, J.W., 1985. Principal stress directions and the ambiguity in fault plane identification from focal mechanisms. Bull. Seis. Soc. Am., 75, 621-626.

Gephart, J.W. and D.W. Forsyth, 1984. An improved method for determining the regional stress tensor using earthquake focal mechanism data: Application to the San Fernando earthquake sequence. Jl. Geophys. Res., 89, 9305-9320.

Gledhill, K, R. Robinson, T.Webb, Rachel Abercrombie, D. Eberhart-Phillips, J. Beavan, and J. Cousins, in preparation. The Mw6.2 Cass, New Zealand, earthquake of 24 November, 1995: Reverse faulting in a strike-slip environment.

Harmsen, S.C. and A.M. Rogers, 1986. Inferences about the local stress field from focal mechanisms: Applications to earthquakes in the southern Great Basin of Nevada. Bull. Seis. Soc. Am., 76, 1560-1572.

Horiuchi, S., G. Russo, and A. Hasegawa, 1995. Discrimination of fault planes from auxiliary planes based on simultaneous determination of stress tensor and a large number of fault plane solutions. Jl. Geophys. Res., 100, 8327-8338.

King, G.C.P, R. Stein, andf J. Lin, 1994. Static stress changes and the triggering of earthquakes. Bull. Seiss. Soc. Am., 84, 935-953.

Michael, A.J., 1984. Determination of stress from slip data, folds, and faults. Jl. Geophys. Res, 89, 11517-11526.

Michael, A.J., 1987. Use of focal mechanisms to determine stress: A control study. Jl. Geophys. Res., 92, 357-368.

Mori, J.J., D. Wald, and R. Wesson, 1995. Overlapping Fault Planes of the 1971 San Fernando and 1994 Northridge, California, earthquakes. Geophys. Res. Lett., 22, 1033-1036.

Okada, Y., 1992. Internal deformation due to shear and tensile faults in a half-space. Bull. Seis. Soc. Am., 82, 1018-1040.

Oppenheimer, D.H., P.A. Reasenberg, and R.W. Simpson, 1988. Fault plane solutions for the 1984 Morgan Hill, California, earthquake sequence: Evidence for the state of stress on the Calaveras Fault. Jl. Geophys. Res., 93, 9007-9026.

Pearson, C.F., J. Beavan, D.J. Darby, G.H. Blick, and R.I. Walcott, 1995. Strain distribution across the Australian-Pacific plate boundary in the central South Island, New Zealand, from 1992 GPS and earlier terrestrial observations. Jl. Geophys. Res., 100, 22,071-22,081.

Raleigh, C.B., J.H. Healy, and J.D. Bredehoeft., 1972. Faulting and crustal strength at Rangely, Colorado. In: Flow and Fracture of Rock, Geophysical Monograph 16, American Geophysical Union, 275-284.

Reasenberg, P.A., and R.W. Simpson, 1992. Response of regional seismicity to the static stress changes produced by the Loma Prieta earthquake. Science, 255, 1687-1690.

Reyners, M.E., R. Robinson, and P.J. McGinty, 1997. Plate coupling in the northern South Island and souternmost North Island, New Zealand, as illuminated by earthquake focal mechanisms. Jl. Geophys. Res., 102, 15197-15210.

Rice, J.R., 1992. Fault stress states, pore pressure distributions, and the weakness of the San Andrea fault. In: Eavans, B. and T.F. Wong, editors, Fault Mechanisc and Transport Properties of Rock; a Festschrift in Honor of W.F. Brace. Academic Press, London. pp 475-503.

Rivera, L. and A. Cisternas, 1990. Stress tensor and fault plane solutions for a population of earthquakes. Bull. Seis. Soc. Am., 80, 600-614.

Robinson, R. and T. Webb, 1996. AMPRAT and MECHTOOL: programs for determining focal mechanisms of local earthquakes. Institute of Geological & Nuclear Sciences Science Report, 96/7.

Schwartz, S.Y., 1995. Source parameters of aftershocks of the 1991 Costa Rica and 1992

Cape Mendocino, California, earthquakes from inversion of local amplitudes rations and broadband waveforms. Bull. Seis. Soc. Am., 85, 1560-1575.

Scholz, C., 1990. The Mechanics of Earthquakes and Faulting. Cambridge University Press, Cambridge.

Webb, T. and H. Anderson, in press. Focal mechanisms of large earthquakes in the North Island of New Zealand: Slip partitioning at an oblique active margin. Jl. Geophys. Res.

Yu, G., S.G. Wesnousky, and G. Ekstrom, 1993. Slip partitioning along major convergent plate boundaries. Pure and Applied Geophysics, 140, 183-210.

Zhao, D., H. Kanamori, and D. Wiens, 1997. State of stress before and after the 1994 Northridge earthquake. Geophys. Res. Lett., 24, 519-522.

Figure Captions

1) Map view of aftershock locations for the Arthur's Pass earthquake, quality A and B solutions. The rectangle represents the surface projection of the mainshock fault plane.

2) Focal mechanisms for the Arthur's Pass aftershocks. All events, quality A or B, of magnitude 3.1 or more during the period of good coverage with portable seismographs (22 June - 2 July, 1994) are included.

3) An example of the use of P/S amplitude ratio in constraining a focal mechanism when there a few P-wave polarity observations. Left: Allowable P (crosses) and T (circles) axes for mechanisms that satisfy all the polarity observations. The nodal planes shown are those that are maximally distant from the observations. Center: P and T axes for mechanisms that fit all the polarity *and* fit the amplitude rations fairly well. The nodal planes are those that fit all polarity observations and best fit the amplitude rations. Right: The nodal planes from the center figure plus the actual polarity observations (solid circles = compression, open circles = dilation)

4) P (left) and T (right) axes for the mechanisms in Figure 2, if the event is more than 2 km from the mainshock fault plane.

5) P (left) and T (right) axes of the 4012 earthquakes used to test our stress inversion method.

6) Confidence limits (95%) for the $\sigma 1$ (crosses) and $\sigma 3$ (circles) axes from noisy test data. A: Using all 4012 observations. B: Using 3000 observations. C: Using 2000 observations. D: Using 1000 observations. E: Using 500 observations. F: Using 250 observations.

7) $\sigma 1$ (crosses) and $\sigma 3$ (circles) axes from the inversion of 3808 polarities from 385 events, quality A and with 8 or more polarity observations. 95% confidence limits are indicated by the areas defined by the symbols, with the actual result being bolder stars. The "beachballs" show the focal mechanisms corresponding to the two optimal faults, the asterisk indicating that the upper mechanism is the preferred mechanism, but not by very much.

8) Changes in Coulomb Failure Stress (δCFS) at 5 km depth, on planes with optimal orientations in the regional plus induced stress field. The fault orientations and slip directions were picked to give the best (by eye) correlation, while remaining within the error bars. White rectangles are the surface projections of the faults. White crosses are higher quality aftershock epicentres for events in the 4 - 6 km depth range. Note that the colors saturate well below the their maximum/minimum values.

9) δCFS on faults with the same orientation and sense of slip as the 1995 Cass earthquake, M6.2, 30 km east of the Arthur's Pass earthquake, at 5 km depth. The cross marks the location of the Cass earthquke. Note the CFS scale change from Figure 8. One corner of the Arthur's Pass fault plane can be seen on the left.

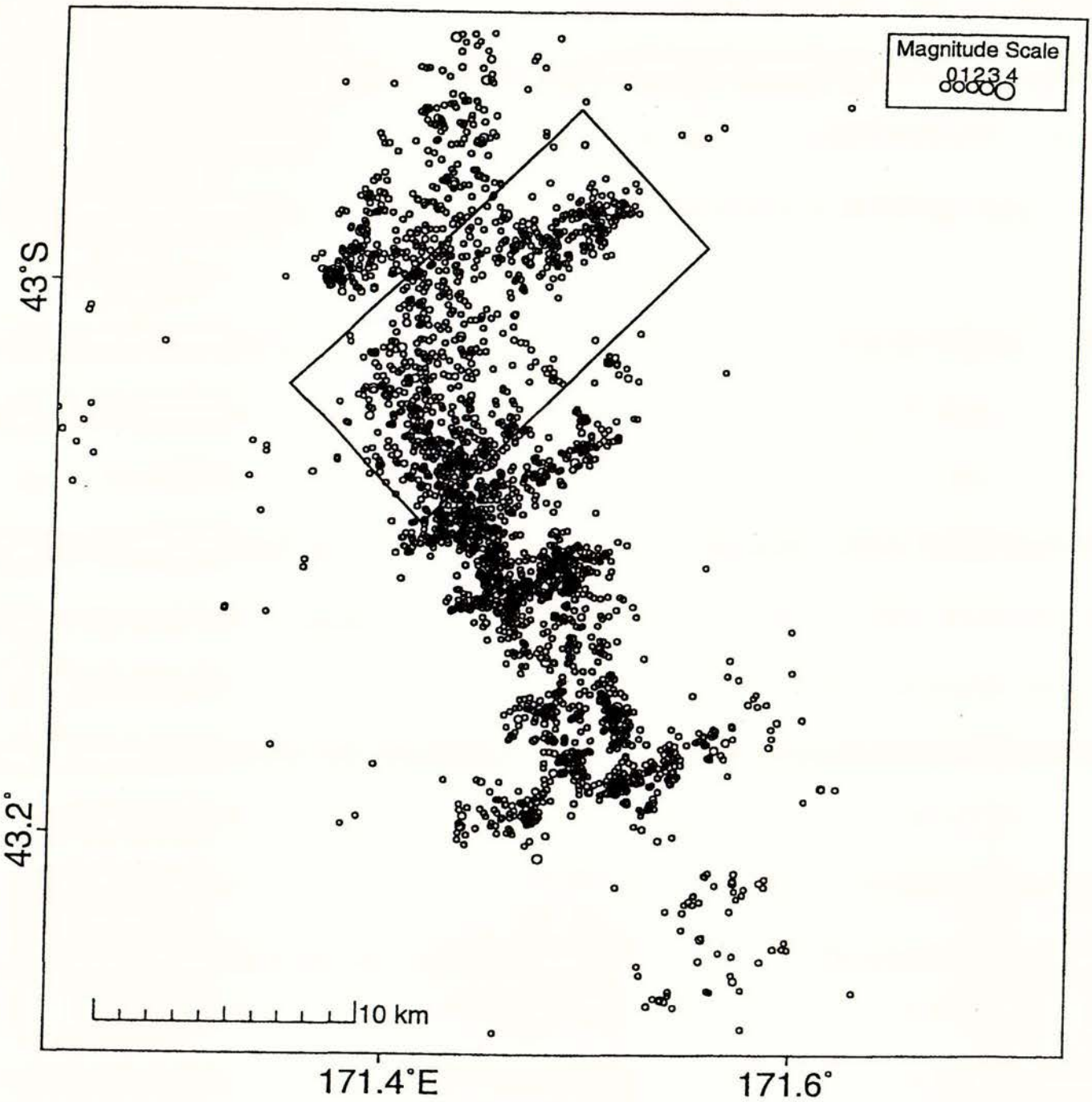

Figure 1

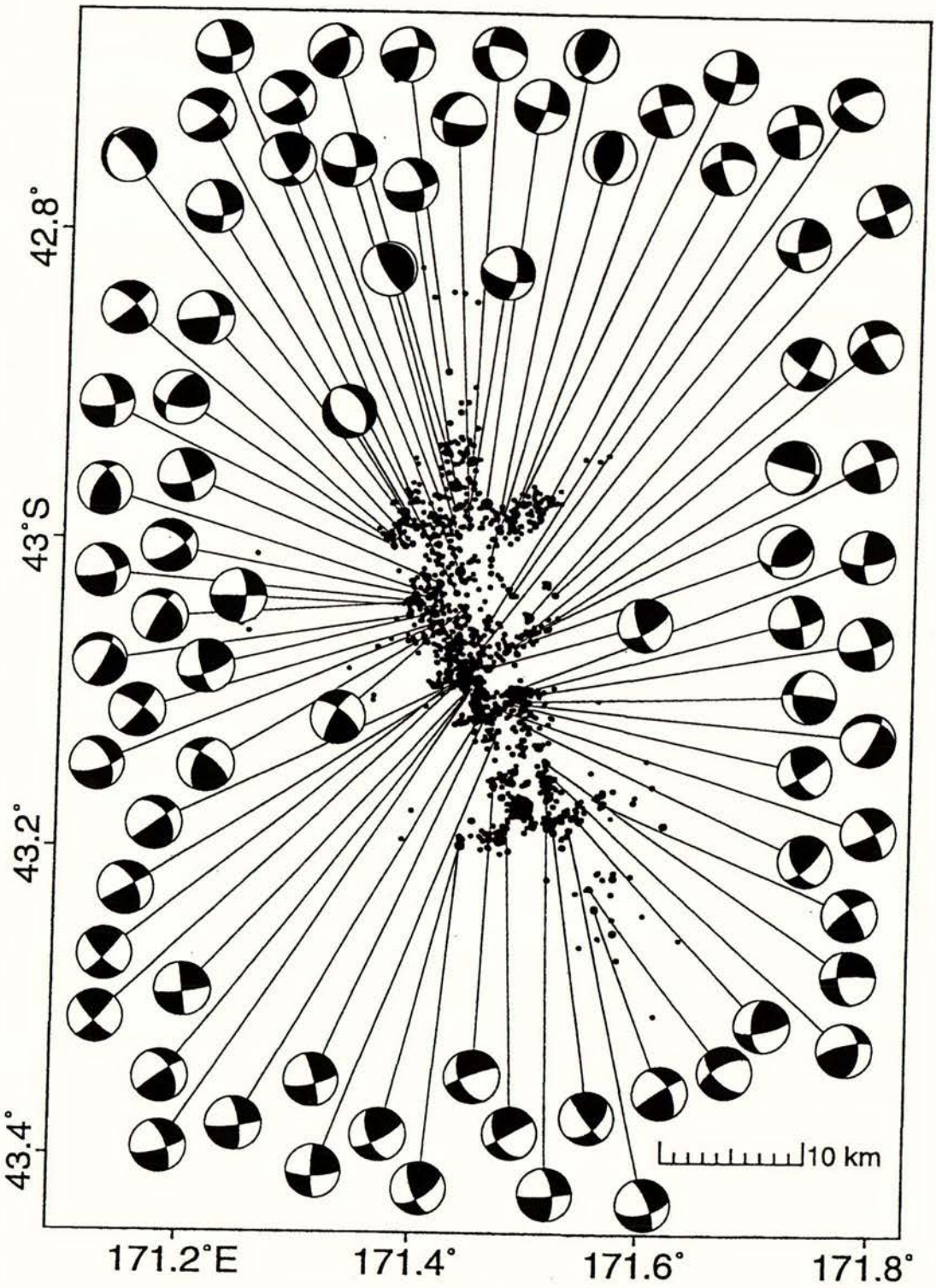

Figure 2

FIRST MOTIONS

FIRST MOTIONS + AMPLITUDES

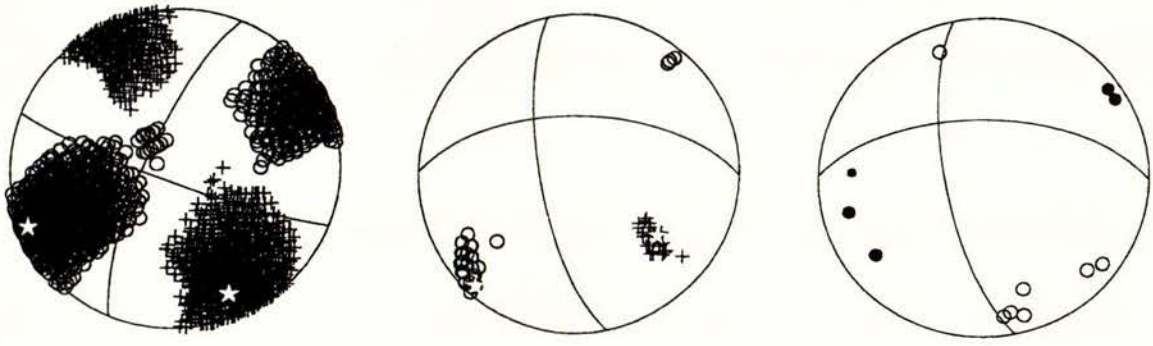

Figure 3

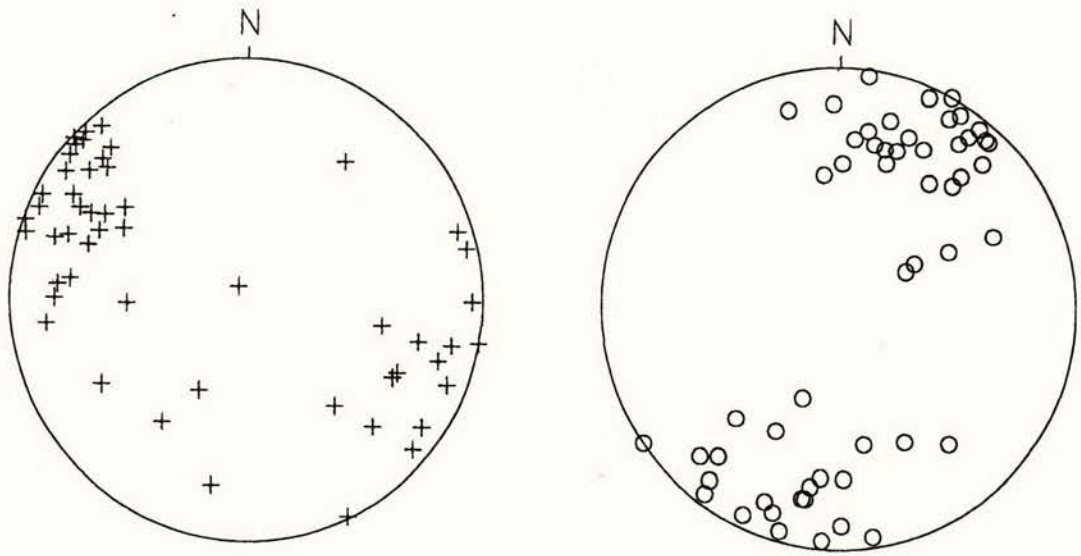

Figure 4

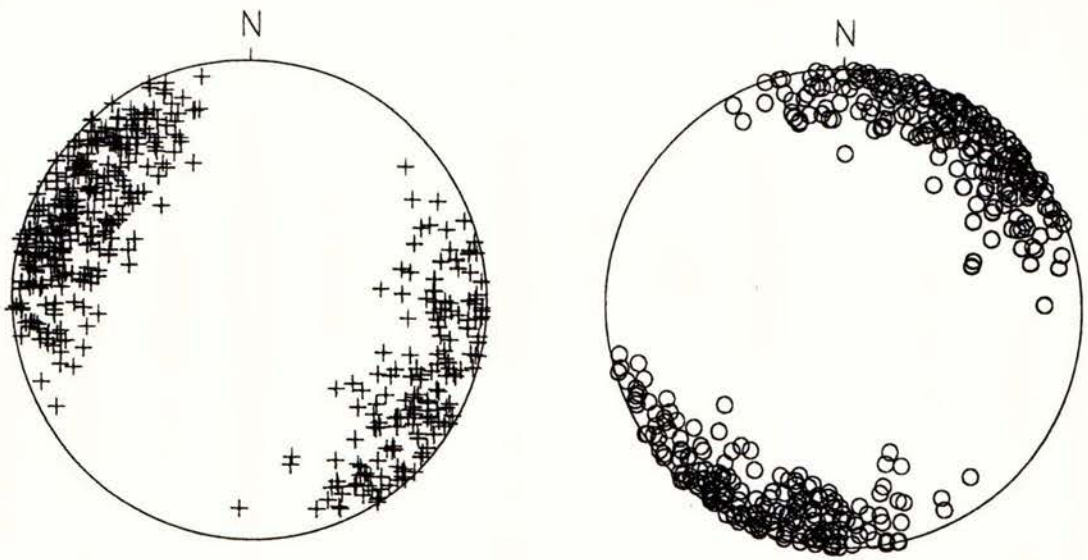

Figure 5

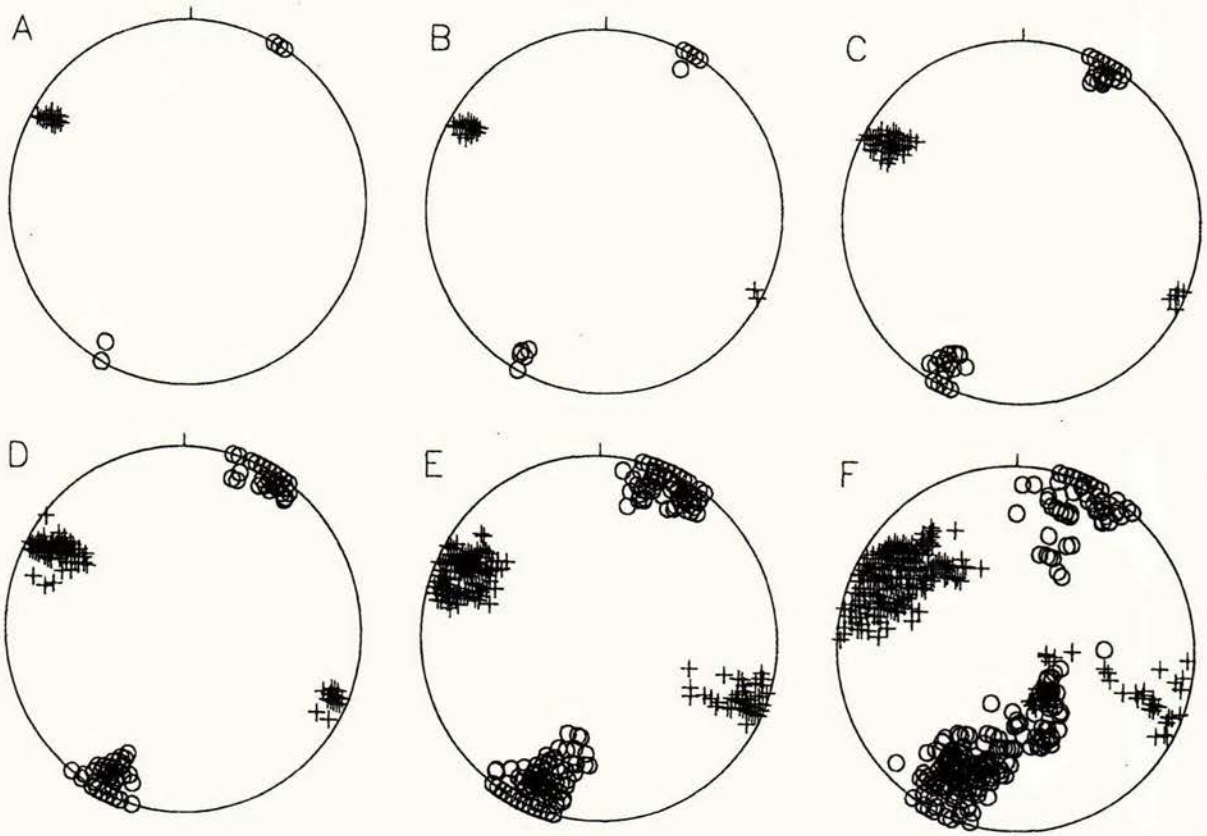

Figure 6

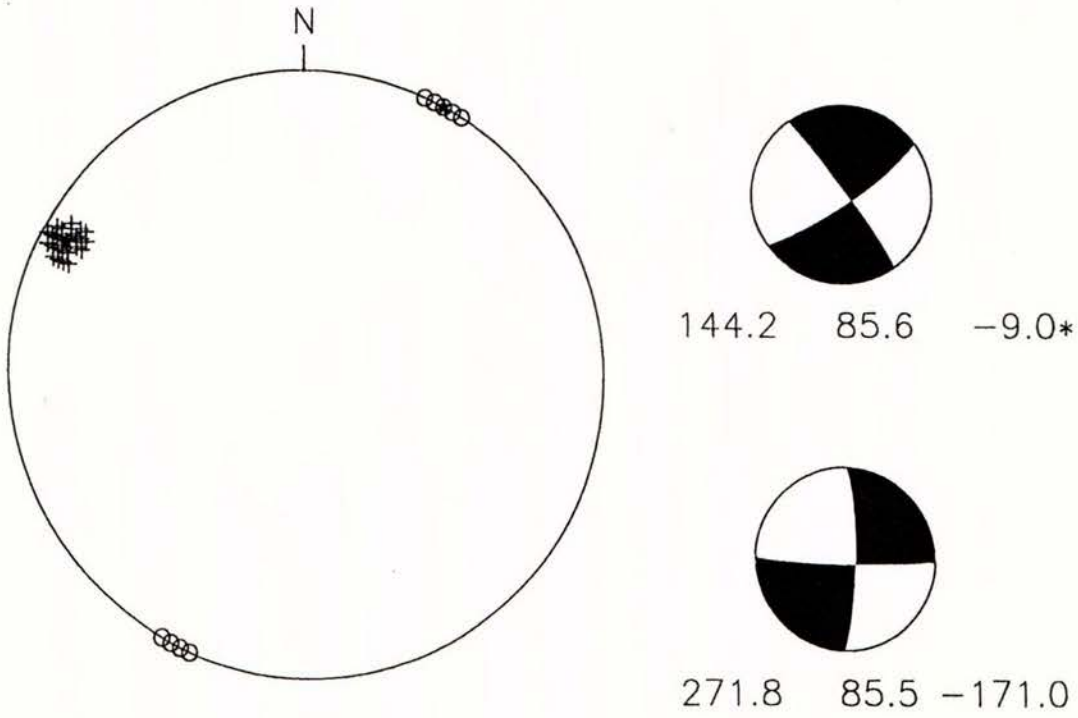

Pazi= 298.0 Pdip= 80.0 Tazi= 28.0 Tdip= 90.0

best score= 93.4% of 3297; worst= 41.7%

confidence limit= 95.0%

Figure 7

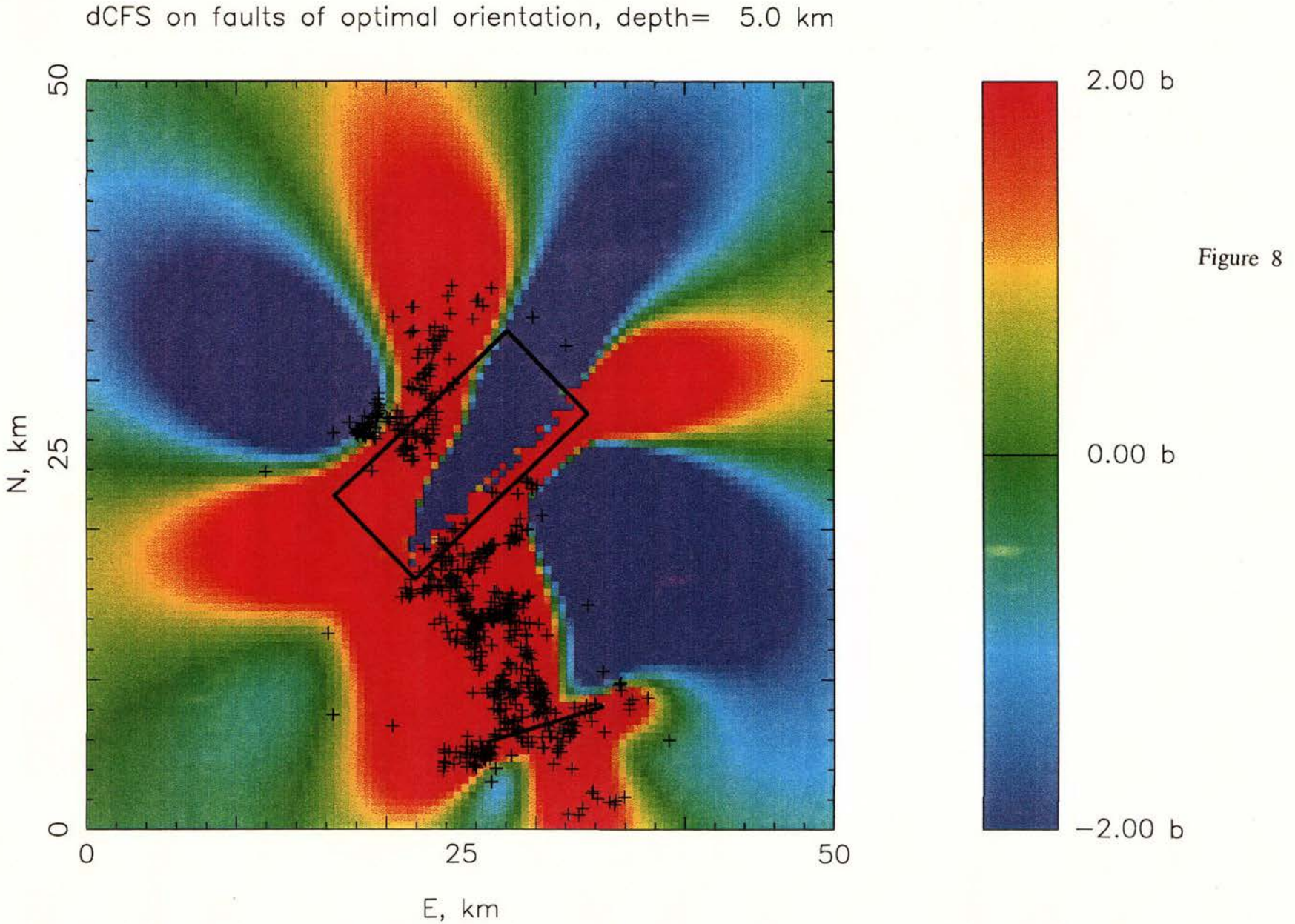
dCFS on faults of optimal orientation, depth= 5.0 km
50
25
0
N, km
0
25
50
E, km
2.00 b
0.00 b
−2.00 b

Figure 8

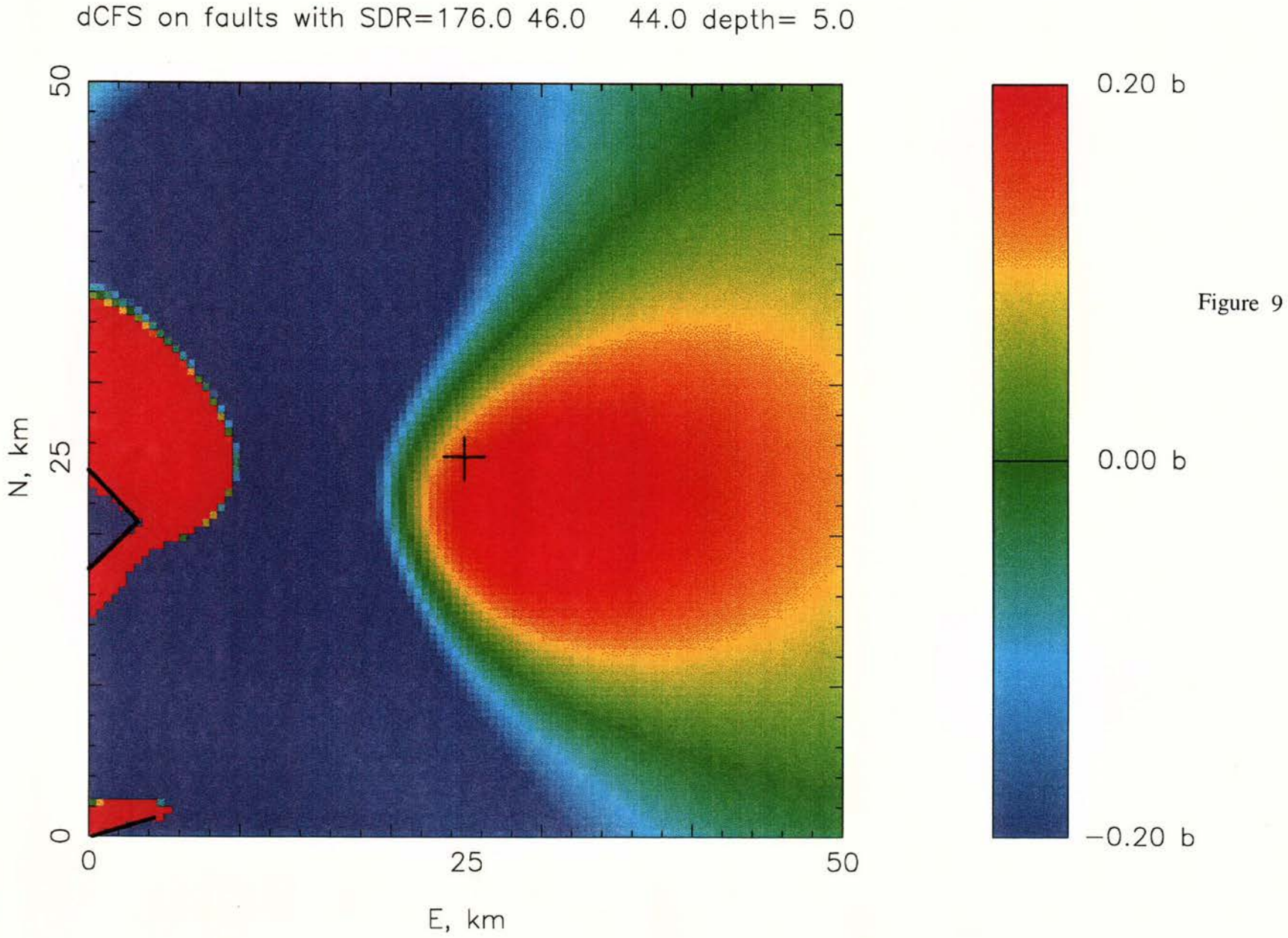
dCFS on faults with SDR=176.0 46.0 44.0 depth= 5.0
50
25
0
N, km
0
25
50
E, km
0.20 b
0.00 b
−0.20 b

Figure 9

APPENDIX

Progress report from analysis of GPS data for the Earthquake Commission. December 1995.

Project title: Seismotectonics of the Arthur's Pass earthquake of 18 June, 1994.

Provider; Dr. Thora Arnadottir

Funding: NZ$17,167

Objectives from analysis of GPS data:

(1) Use geodetic data determined from GPS surveys in December 1992, July 1994 and February 1995 to improve models of interseismic deformation.

(2) Calculate coseismic displacements from the GPS surveys in 1992, 1994 and 1995.

(3) Complete analysis of GPS data and estimation of the dislocation model which gives the best fit to the coseismic displacements.

Introduction

The Mw6.7 18 June 1994, Arthur's Pass earthquake occurred within a network of Global Positioning System (GPS) stations. Figure 1 shows the location and the Harvard Centroid Moment Tensor (CMT) solution for the main shock (beach ball), the two largest aftershocks (stars) and location of the first three days of aftershocks (crosses). The locations of GPS stations are shown with triangles. The network was first measured using GPS in December 1992 as part of a study of plate boundary deformation across the South Island of New Zealand (Pearson et al., 1995). In July 1994, in the 3 weeks following the earthquake, a resurvey of 32 stations was conducted. In February of 1995 the whole network was surveyed again and a number of new stations added (black triangles in Figure 1). The GPS surveys were conducted by a group of scientists from the Institute of Geological and Nuclear Sciences (GNS), Victoria University of Wellington, the University

of Otago, the Department of Survey and Land Information (DOSLI) and Columbia University, USA (see Beavan, 1995)

The GPS data from the three surveys was analyzed with the University of Bern software (Rothacher et al., 1993) and precise satellite orbits determined from the world wide tracking network by the Centre for Orbit Determination in Europe (CODE). See Pearson et al. (1995) and Arnadottir et al. (1995) for more details on the data analysis. The final station coordinates and covariances were estimated using a network adjustment software. We define a Pacific-fixed reference frame by holding the coordinates of station 5508 (Christchurch) fixed (see insert in Figure 1). We assume that station 5508 was not influenced by the earthquake. The station displacements were then calculated by differencing the station coordinates between the different surveys.

Results

Displacements of GPS stations

The station displacements were calculated as three dimensional vector changes in station coordinated from December 1992 to July 1994 and December 1992 to February 1995. Figure 2 shows the displacements with 95% confidence ellipses. The 1992-1994 displacements are shown with gray arrows and the 1992-1995 displacements are shown with black arrows. The difference in the station displacements is mostly due to the different amount of interseismic deformation for the two time periods.

Interseismic deformation

In order to obtain an estimate of the coseismic signal we first need to estimate the interseismic signal caused by plate boundary deformation in the study area. One way of estimating the interseismic signal is to difference the station coordinates between the July 1994 and February 1995 surveys. and assume that there is no post-seismic deformation in

1994 and February 1995 surveys, and assume that there is no post-seismic deformation in the area. Scaling the displacements thus obtained to represent the interseismic deformation during the appropriate time period (e.g. December 1992 to February 1995), and subtracting from the measured displacements shown in Figure 2, then gives the coseismic displacements, assuming that the rate of deformation is constant in time between earthquakes. Figure 3 shows the displacements obtained by differencing the July 1994 and February 1995 measurements, i.e. the interseismic deformation during that time. Note that the displacements are small (on the order of a few cm), and the 2 sigma uncertainty in the data are an appreciable portion of the signal in the epicentral area.

Dislocation modeling of interseismic signal

We model the interseismic displacements using a rectangular dislocation source in an elastic half-space (Okada, 1985). The dislocation geometry (fault strike, dip, length along strike, down-dip width, depth and location) and slip parameters that provide the best fit to the data are estimated using a nonlinear inversion technique (Arnadottir and Segall, 1994).

The low signal to noise ratio of the 1994-1995 data makes solution convergence difficult unless we constrain some of the model parameters. Therefore we fix the fault dip to 50° SE, and the strike, location and depth to center so that the model lies in the plane of the Alpine Fault, and estimate the remaining parameters. Figure 4 shows the observed (black arrows and 95% confidence ellipses) and calculated (gray arrows) displacements for the best fit model obtained by the nonlinear inversion. The broad gray line in Figure 4 shows the surface projection of the upper edge of the model. The top of the model is at 8.5 km depth, with 56 mm of right-lateral slip and 14 mm of normal motion below that depth. This equates to 96 mm/yr strike-slip and 24 mm/yr normal slip below 8.5 km on the Alpine fault. This slip rate is significantly higher than the estimated 36 mm/yr strike-slip and 18 mm/yr reverse motion estimated by Pearson et al. (1995) by resolving the NUVEL1A plate motion (DeMets et al., 1990, 1994) on the Alpine fault. The sense of dip-

model we obtain has normal rather than reverse motion. Pearson et al. (1995) found that the fault normal contraction (γ_1) estimated by their model gave poor fit to the observed strain rate across the Alpine fault. They concluded that crustal shortening is not taken up by dip-slip motion on the Alpine fault. Our results from modeling the interseismic signal supports their finding. However the high strike-slip rate we obtain would predict a much higher fault parallel component of stress (γ_2) than observed by Pearson et al. (1995). The GPS data we fit in the inversion are the station displacements relative to station 5508. The displacement at that station was not constrained in the inversion, and it is therefore possible that the high slip rates obtained on the Alpine Fault from the inversion are biased. GPS observations over a longer time period will help to resolve the discrepancy in the interseismic model.

We also investigated models allowing slip on the Hope fault as well as the Alpine fault. However, this did not improve the fit to the GPS data. The station distribution is such that the constrains on the Hope fault are poor, since almost all the stations are south of the Hope fault. We therefore conclude that slip on the Hope fault can not be determined from these GPS data.

Linear NUVEL1A interseismic model

There are some problems with using the measurements between July 1994 and February 1995 as the interseismic deformation. One is that not all stations were measured in July 1994 so the interseismic deformation at a number of stations is missing when we consider the 1992 - 1995 dataset. Another problem is to assume that the 1994-1995 data contains only interseismic deformation. There is some indication that there is postseismic deformation at stations close to the epicenter (particularly station 1416, see Figure 3). We therefore also estimate the interseismic deformation by assuming that the stations on the West Coast move at a full NUVEL1A plate velocity, and the velocity decreases linearly to zero towards southeast (assume zero velocity at station 5104). This allows us to calculate

the interseismic deformation at all stations, for the appropriate time period. Figure 5 shows the interseismic deformation for 1 year estimated from the scaled 1994-1995 data (black arrows with 95% confidence ellipses), the calculated displacements from the best fit inversion model (dark gray arrows) and the displacements from a linearly decreasing velocity model based on NUVEL1A (light gray arrows). From this we see that the interseismic displacements predicted by a linearly decreasing velocity model are very similar to the estimation from the best fit inversion model, and within the estimated error in the data for most stations. We choose to use the simple linearly decreasing velocity model to approximate the interseismic deformation because of the above mentioned problems with using the 1994-1995 data. The coseismic deformation in the epicentral area is much larger than the interseismic signal, and errors in the interseismic model are thus not likely to significantly influence the coseismic model.

Coseismic deformation

The coseismic deformation obtained by subtracting the interseismic model (linearly decreasing velocity) from the December 1992 to February 1995 displacements is shown with 95% confidence ellipses in Figure 6. We also calculate the coseismic displacement by subtracting the 1994-1995 data (velocities scaled to 1.6 years) from the 1992-1994 data. The resulting displacements are shown in Figure 7 with gray arrows. Also shown in Figure 7 are the coseismic displacements obtained by subtracting the linearly decreasing interseismic velocity model from the 1992-1994 data. The displacements agree within the data uncertainty for all but a few stations. Comparison of Figures 6 and 7 shows that the coseismic displacements are essentially the same for the different time periods and interseismic models. We therefore use the data shown in Figure 6 (1992-1995 coseismic deformation) in the dislocation modeling, since that dataset includes the most stations. We add data for station 1417 that was measured in January 1994, to the dataset used in the inversion. We also use measurements from January 1994 at station 1416 because of a

large uncertainty in the 1992 measurements at this station. We reject the data from station 1422 because of anomolously large displacements relative to nearby stations considering its distance from the main shock epicentre. Data from station 1422 was found spurious in the 1992 GPS data analysis (J. Beavan, personal communication, 1995). We also do not include data from station 1403 because the benchmark was destroyed by lightning, although the mark could be repaired during the 1995 survey. There are far more stations to the east of the main shock epicentre (along the trans-Alpine Highway 73) than to the west particularly in Otira Gorge. In order not to bias the solution we do not include all the stations along SH73 in the inversion. The fit to all these stations is calculated from the best fit models. We find that not including them in the inversion does not significantly alter the solution, but affects the residual for the final model slightly.

Dislocation modeling of coseismic signal

As in the interseismic modeling, we use the nonlinear inversion method to estimate the fault geometry (fault strike, dip, length along strike, down-dip width, depth and location) and slip parameters for a dislocation model that provides the best fit to the coseismic displacements. We find that a single dislocation with uniform slip does not provide a good fit to the data. We then allow the fault to have two slip patches, keeping the other fault parameters the same. The best fit model is a NNW-trending dislocation, 8 km wide and 36 km long dipping 50 degrees to the WSW. The calculated displacements for this model are shown in Figure 8 with gray arrows and the 1992-1995 coseismic displacements are shown with black arrows and 95% confidence ellipses. The surface projection of the model is shown with gray blocks. The model has about 5 meters of sinstral and 1 metre of reverse motion on the northern most 12 km of the fault in the main shock hypocentral area (light gray block), but only 0.5 meters and 0.3 meters of sinstral and reverse motion respectively on the southern 25 km (dark gray block). The geodetic moment for this model is about 1.4 10^{19} Nm, which agrees well with the estimated seismic moment for the

main shock of 1.3 10^{19} Nm. The best fit model for the 1992-1994 dataset is very similar, except it has about 20 degree steeper dip, and 1 km wider fault than the best fit model for the 1992-1995 dataset (Arnadottir et al., 1995). This is due to the additional stations west of the hypocentre in the 1992-1995 dataset, providing a better constraint for the fault dip.

We also investigated models with two separate faults. Inversion of body wave data by T. Webb (pers. communication, 1995) indicates that the main shock ruptured a NE striking, NW dipping reverse fault. To assess whether such a model would agree with the GPS data, we fixed the fault dip, strike and rake of one fault to the parameters found by Webb (dip = 47°, strike = 213°, rake= 90°), and estimated the remaining 15 parameters. The best fit two fault model with these constraints is shown in Figure 9. The NNW striking fault has similar parameters to the single fault with two slip patches, but has 1.3 meters of sinstral and 0.1 metre of normal motion. The NE striking fault has 1.2 meters of pure reverse motion. The geodetic moment for the two models is about 1.9 10^{19} Nm, which is somewhat higher than the seismic moment for the main shock, but not unreasonably so. If we allow the two fault model to be unconstrained we find a best fit model with the NE fault striking more northerly, and less partitioning between pure reverse slip on one fault and more strike-slip on the other. This model is shown in Figure 10. However, the distribution of GPS stations in the area is not adequate to allow us to reject the more complicated two fault models, nor distinguish between them.

Conclusions

We use GPS data from July 1994 and February 1995 to estimate models of interseismic deformation in the Arthur's Pass area. The best fit model obtained by nonlinear inversion of the GPS data estimates 96 mm/yr right-lateral strike-slip and 20 mm/yr normal motion below 8.5 km depth on the Alpine Fault. These slip rates are significantly higher than rates obtained from NUVEL1A plate motion. We therefore choose to use the more conservative estimates from a simple linearly decreasing velocity model using NUVEL1A plate rates as

the model for interseismic deformation. The interseismic signal in the epicentral area is very small compared to the coseismic signal, so an error in the interseismic model should not significantly bias the coseismic model.

We calculate the coseismic displacements for the 1994 Arthur's Pass earthquake by subtracting the interseismic model from the displacements obtained by differencing the December 1992 to February 1995 station locations. The simplest best fit dislocation model we obtain has two slip patches on a single surface striking NNW, dipping 50° WSW. The model has about 5 meters of sinstral and 1 metre of reverse slip in the hypocentral region and less slip to the south. The geodetic moment for the model agrees well with the seismic moment estimated for the main shock. The GPS data can also be fit with more complex models with two dislocations. In particular, we can fit the GPS data with a model that agrees with the body wave CMT solution obtained by T. Webb (pers. communication, 1995), but the GPS data require two faults rupturing almost at right angles, rather than one fault, and the resulting moment is larger than the estimated seismic moment. We feel that the GPS station coverage in the epicentral area is not dense enough to distinguish more complicated models and additional constraints, such as aftershock locations, are needed to further constrain the source mechanism of the 1994 Arthur's Pass earthquake.

References

Arnadottir, T.; Beavan, J.; Pearson, C., Deformation associated with the 18 June, 1994, Arthur's Pass earthquake, New Zealand. New Zealand Journal of Geology and Geophysics, in press, 1995.

Arnadottir, T.; Segall, P., The 1989 Loma Prieta earthquake imaged from inversion of geodetic data. Journal of Geophysical Research, 99, 21,835-21,855, 1994.

Beavan, R. J., Kinematics of the New Zealand Plate Boundary: Field Report on the 1995 GPS Survey of the Christchurch to Hokitika Network, IGNS report 95/15, 1995.

DeMets, C; Gordon, R. G.; Argus, D. F.; Stein, S.; Current plate motions, Geophysical Journal, 101, 425-478, 1990.

DeMets, C; Gordon, R. G.; Argus, D. F.; Stein, S.; Effect of recent revisions to the geomagnetic reversal time scale on estimates of current plate motions, Geophysical Research Letters, 21, 2191-2194, 1994.

Okada, Y., Surface deformation due to shear and tensile faults in a half-space, Bulletin of the Seismological Society of America, 75, 1135-1154, 1985.

Pearson, C.; Beavan, R. J.; Darby, D. J.; Blick, G. H.; Walcott, R. I.: Strain distribution across the Australian-Pacific plate boundary in the central South Island, New Zealand, from 1992 GPS and earlier terrestrial observations, Journal of Geophysical Research, 100, 22,071-22,081, 1995.

Rothacher, M., Beutler, G; Gurtner, W; Schildknecht, T.; Wild, U.: Documentation for Bernese GPS software version 3.4., Astronomical Institute, University of Bern, Bern, 1993.

Figure Captions

Figure 1. Location of the June 18, 1994, Mw6.7 Arthur's Pass earthquake. The main shock location is shown with the Harvard CMT solution. The two largest aftershocks are shown with stars, and the location of aftershocks from June 25 to June 27, 1994 are shown with crosses. The major faults (PPAFZ stands for Porters-Pass Amberly Fault Zone) and geographic locations in the area are labeled, and the Trans-Alpine Highway 73 is shown. The GPS station locations are shown with triangles, with different outlines and shading depicting when they were surveyed. The location of station 5508 in Christchurch is shown in the inset.

Figure 2. GPS station displacements with 95% confidence ellipses are shown for two time periods, December 1992 to July 1994 (gray), and December 1992 to February 1995 (black). The difference in displacements is mostly due to the different amount of interseismic deformation for the two periods.

Figure 3. GPS station displacements for July 1994 to February 1995, with 95% confidence ellipses. Note that the magnitude of displacement in the epicentral area for this period is much smaller than in Figure 2.

Figure 4. Observed and modelled displacements for the July 1994 to February 1995 period. Black arrows with ellipses are the data and gray arrows are the model. The model is the best fit dislocation lying in the plane of the Alpine Fault. It is slipping at a rate of 56 mm of right-lateral strike slip and 14 mm of normal motion below 8.5 km depth The bold gray line shows the surface projection of the top of the dislocation model.

Figure 5. Comparison of two interseismic models and the GPS data (black arrows). The dark gray arrows show the best fit dislocation model from inversion (shown in Figure 4), and the light gray arrows are a simple linearly decreasing velocity model with the stations on the West Coast moving at the full NUVEL1A plate rate, and linearly decreasing to zero at station 5104.

Figure 6. Coseismic displacements for the time period December 1992 to February 1995 calculated by subtracting a linearly decreasing velocity model from the observed displacements for the time period.

Figure 7. Coseismic displacements for the time period December 1992 to July 1994 calculated using two different interseismic models. The gray arrows are the 1992-1994 data subtracted by the 1994-1995 data, and the black arrows are the 1992-1994 data subtracted by a linearly decreasing velocity model.

Figure 8. Observed (black arrows) and best fit dislocation (gray) displacements for a dislocation model with two slip patches. The light gray block is the area of high slip (5 meters sinstral and 1 meter reverse), and the dark gray block is the area of lower slip (0.5 meters of sinstral and 0.3 meters of reverse motion.

Figure 9. Two dislocation models. The NE striking fault is constrained to fit a body wave CMT solution (strike, dip, rake).

Figure 10. Best fit two dislocation model, unconstrained.

The June 18, 1994, Arthur's Pass Earthquake

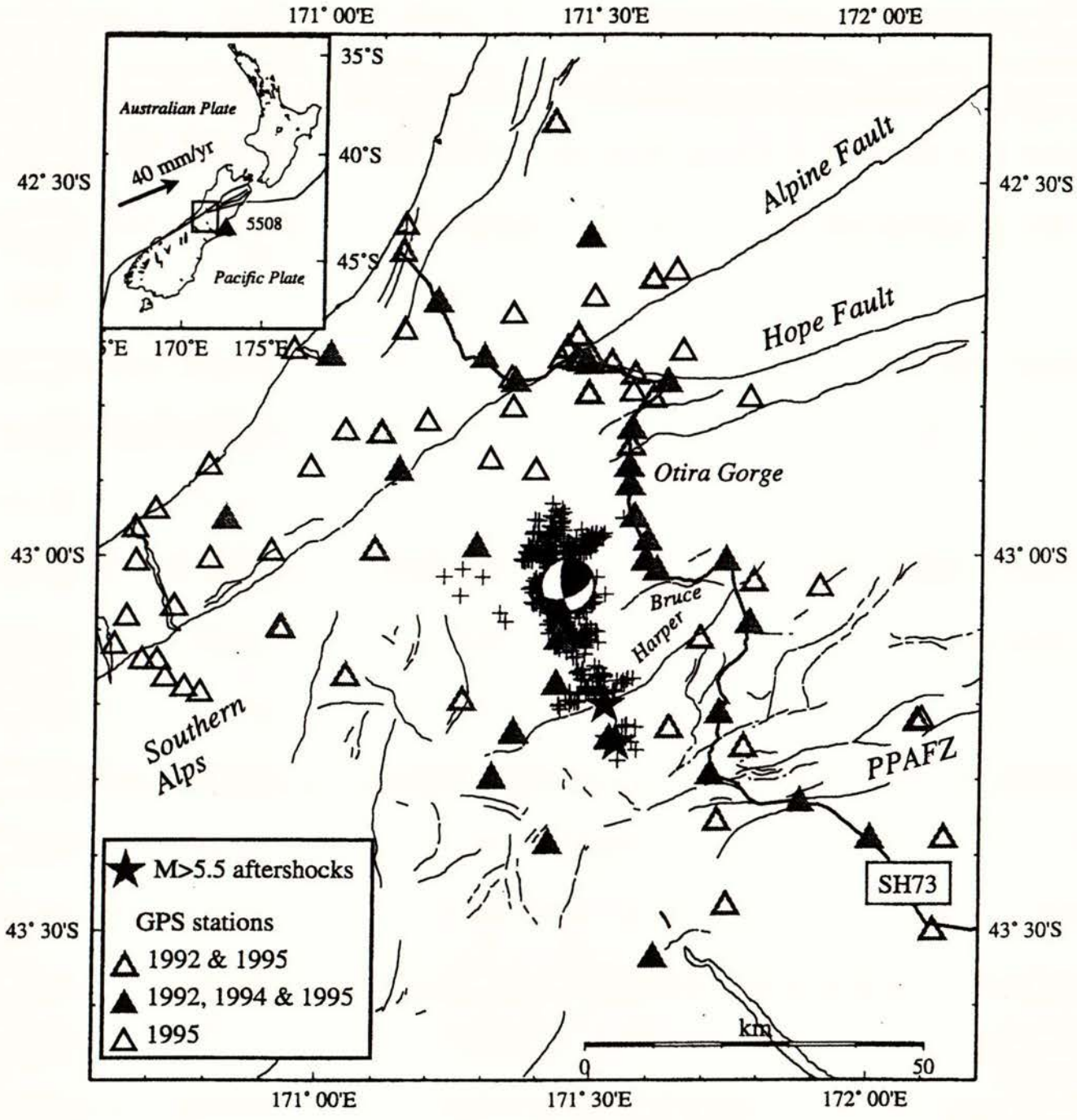

Figure 1

Measured Displacements

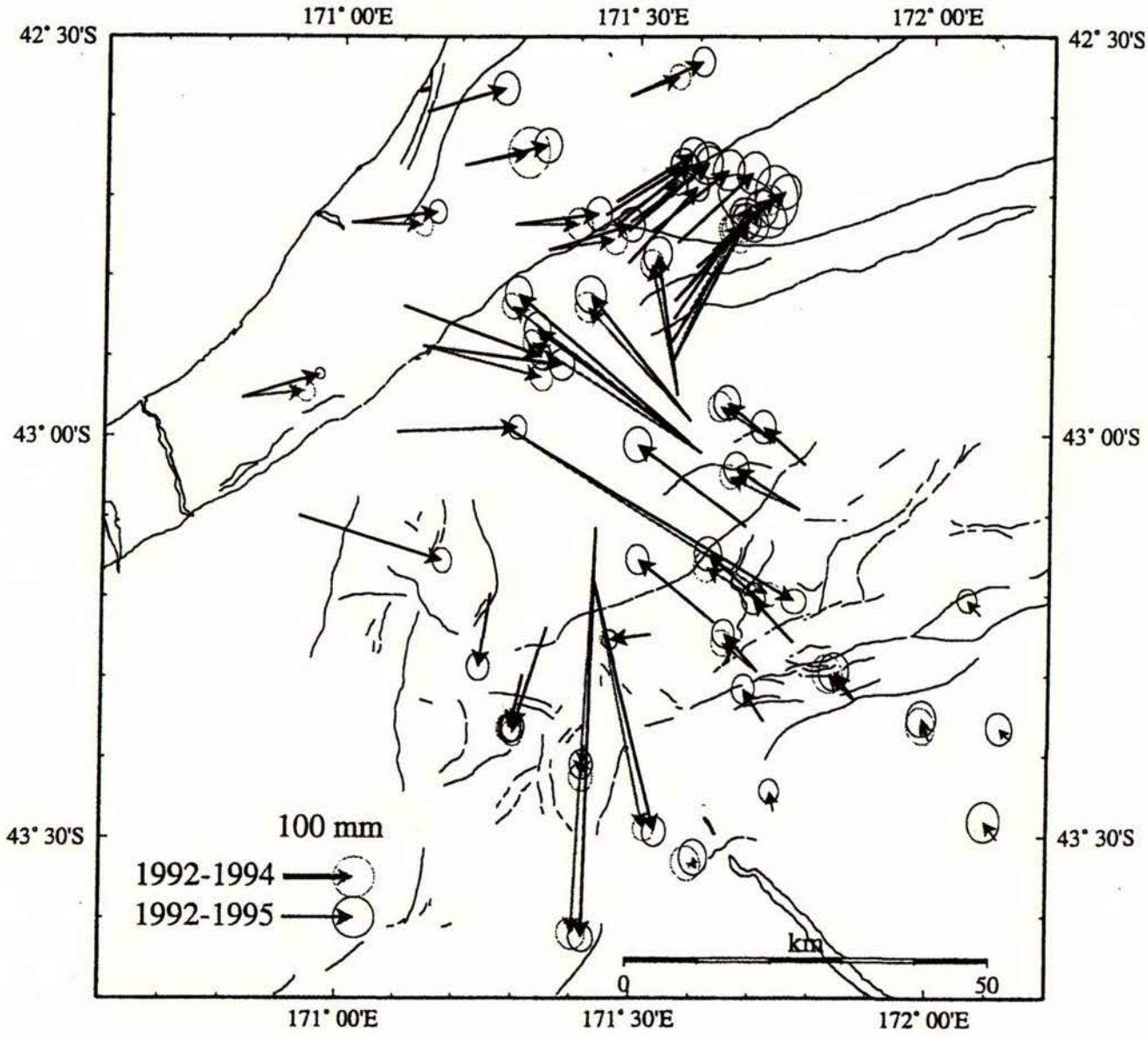

Figure 2

Measured Displacements 1994 - 1995

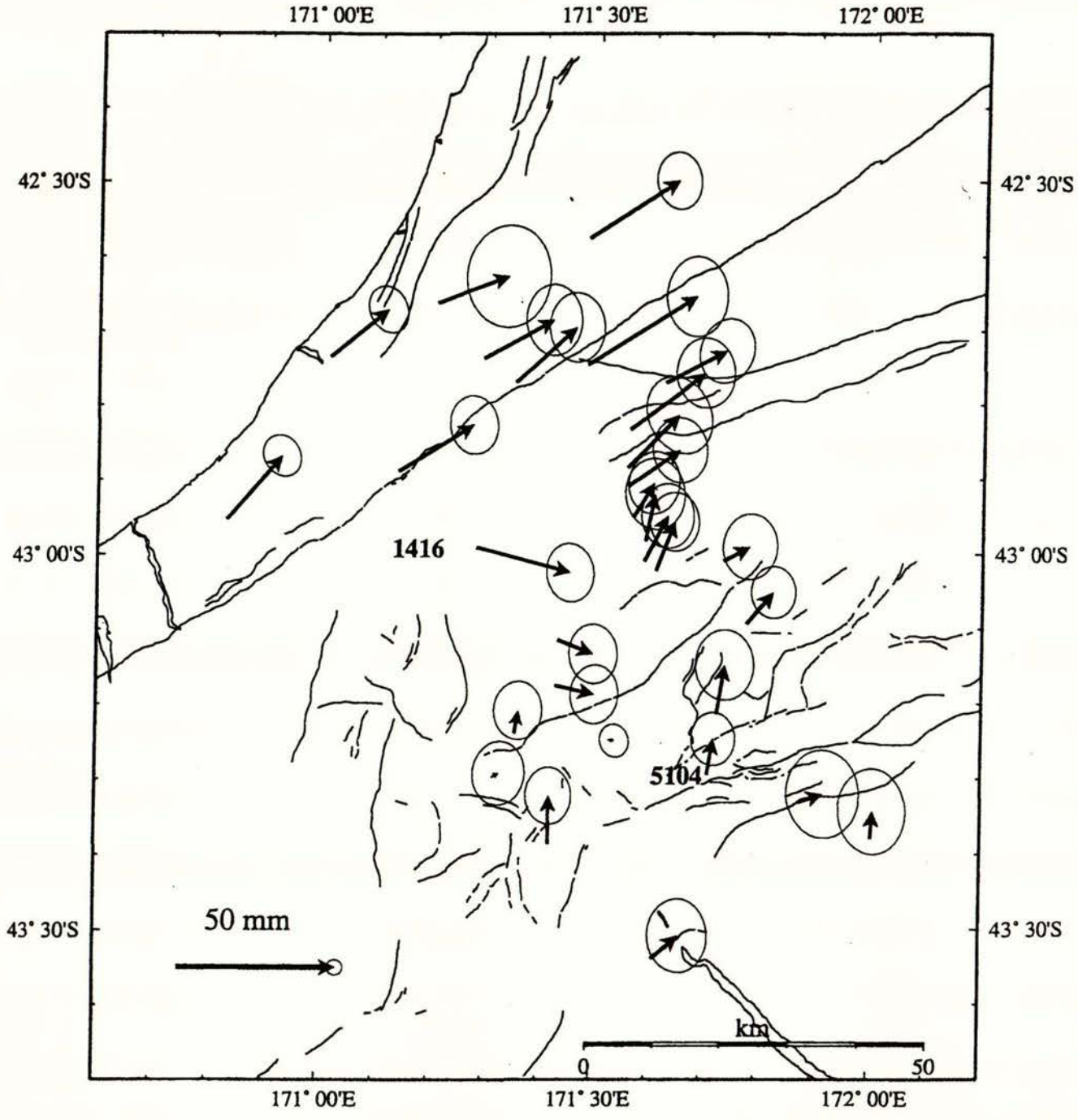

Figure 3

Interseismic Displacements Data and Model

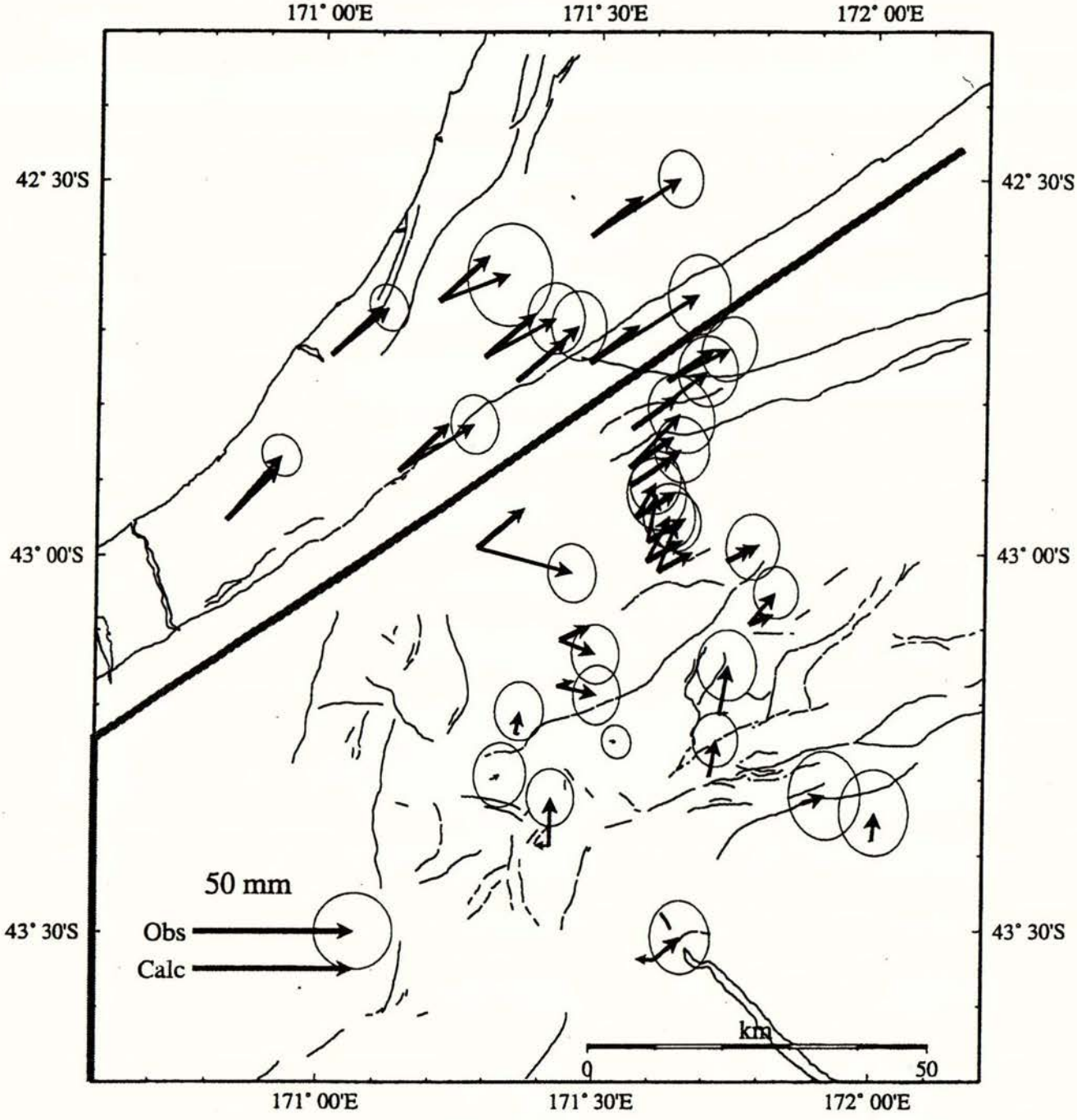

Figure 4

Model of Interseismic Displacements During 1 Year

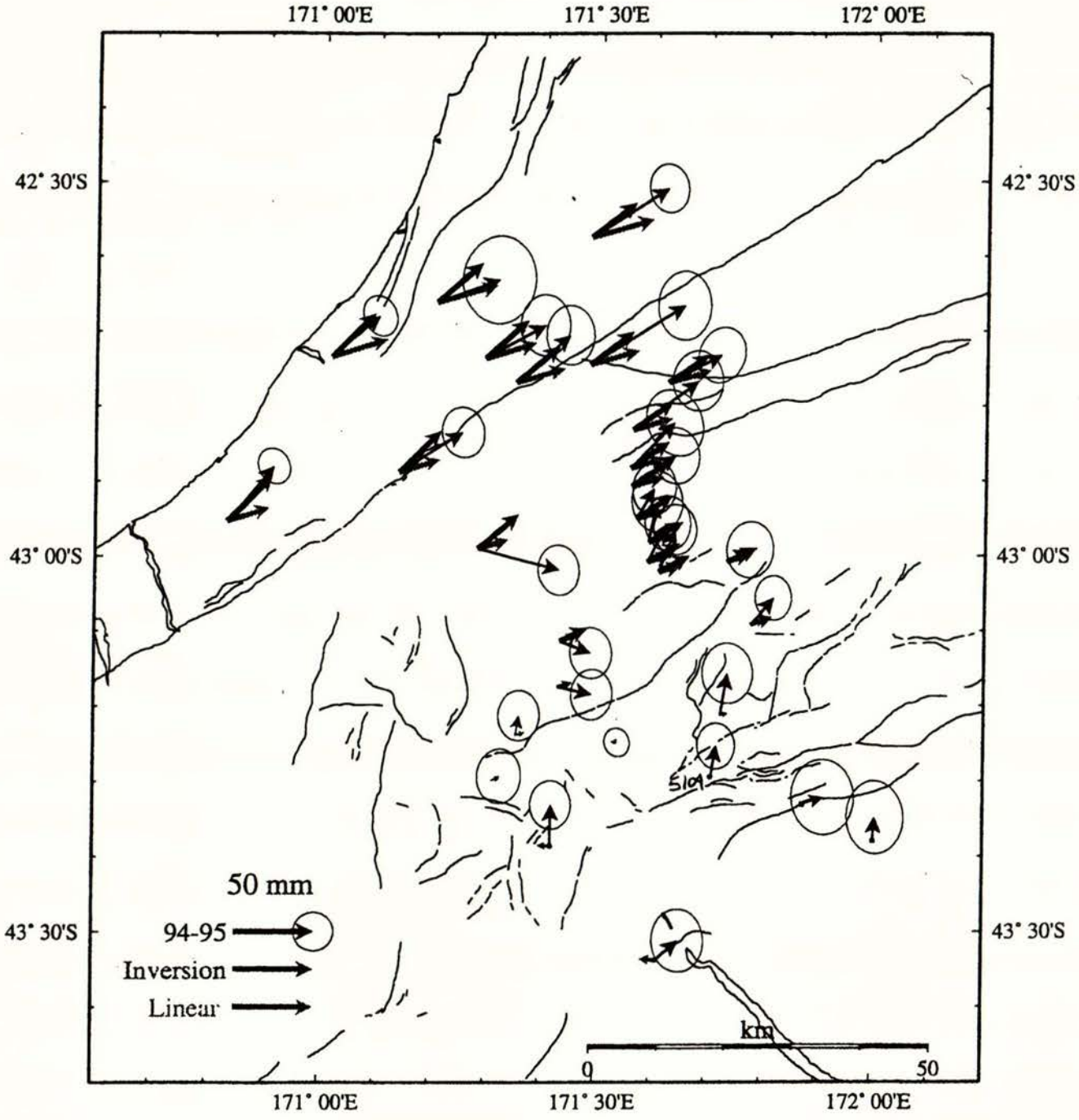

Figure 5

Coseismic Displacements 1992-1995

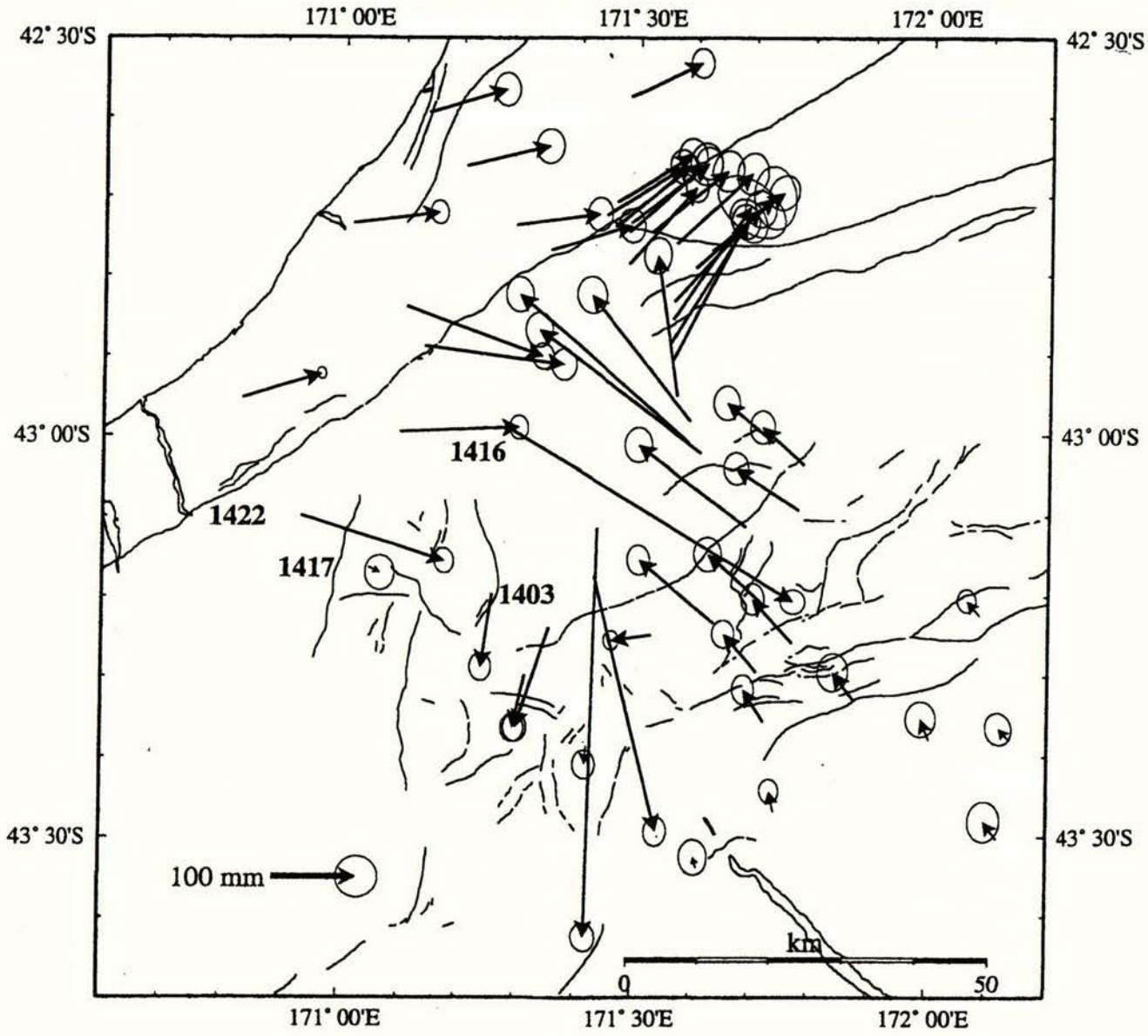

Figure 6

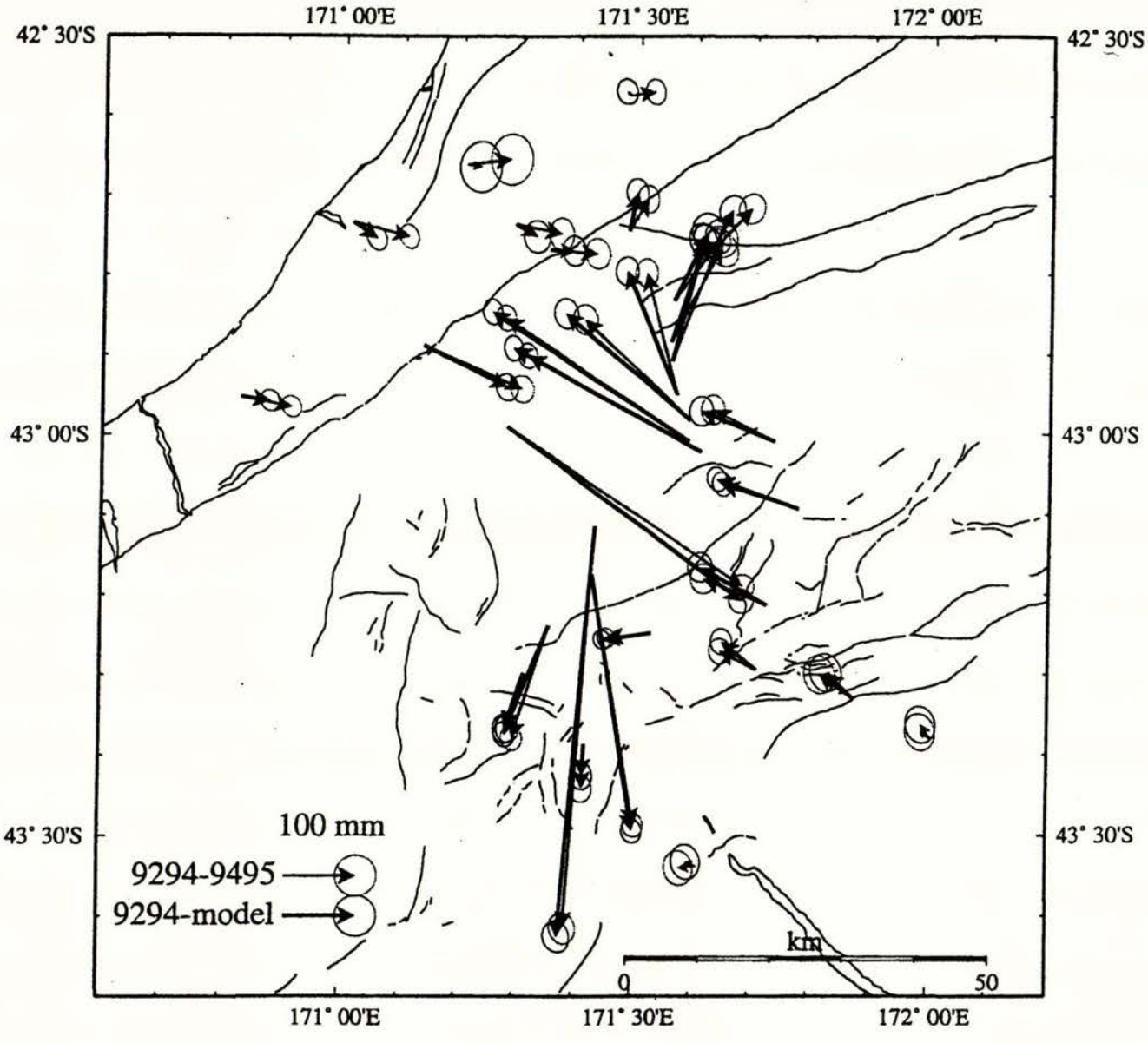
Coseismic Displacements
171° 00'E
171° 30'E
172° 00'E
42° 30'S
43° 00'S
43° 30'S
100 mm
9294-9495
9294-model
km
0
50

Figure 7

Observed and Calculated Coseismic Displacements 1992 - 1995

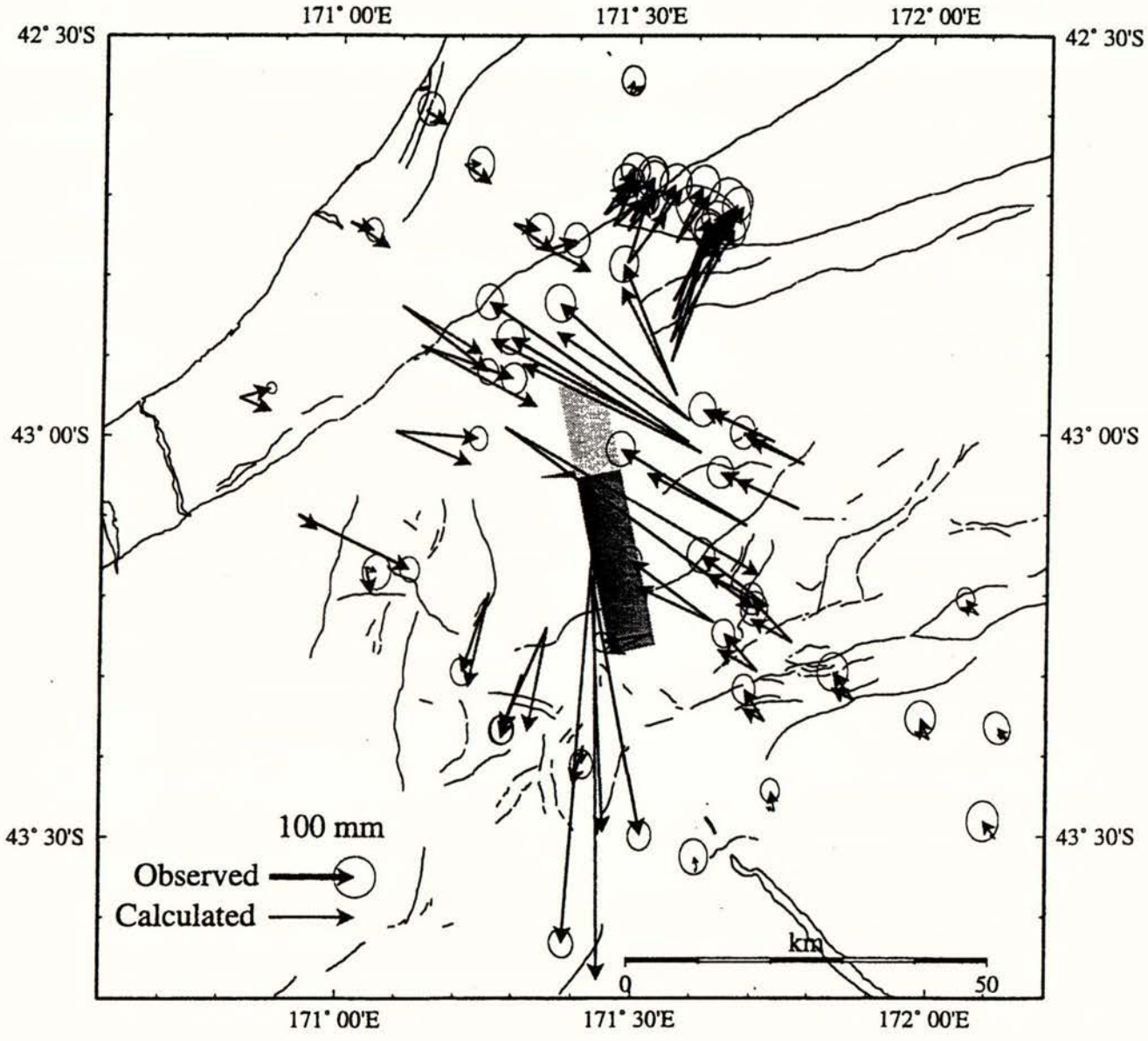

Figure 8

Best Fit Model Constrained by Body Wave Inversion

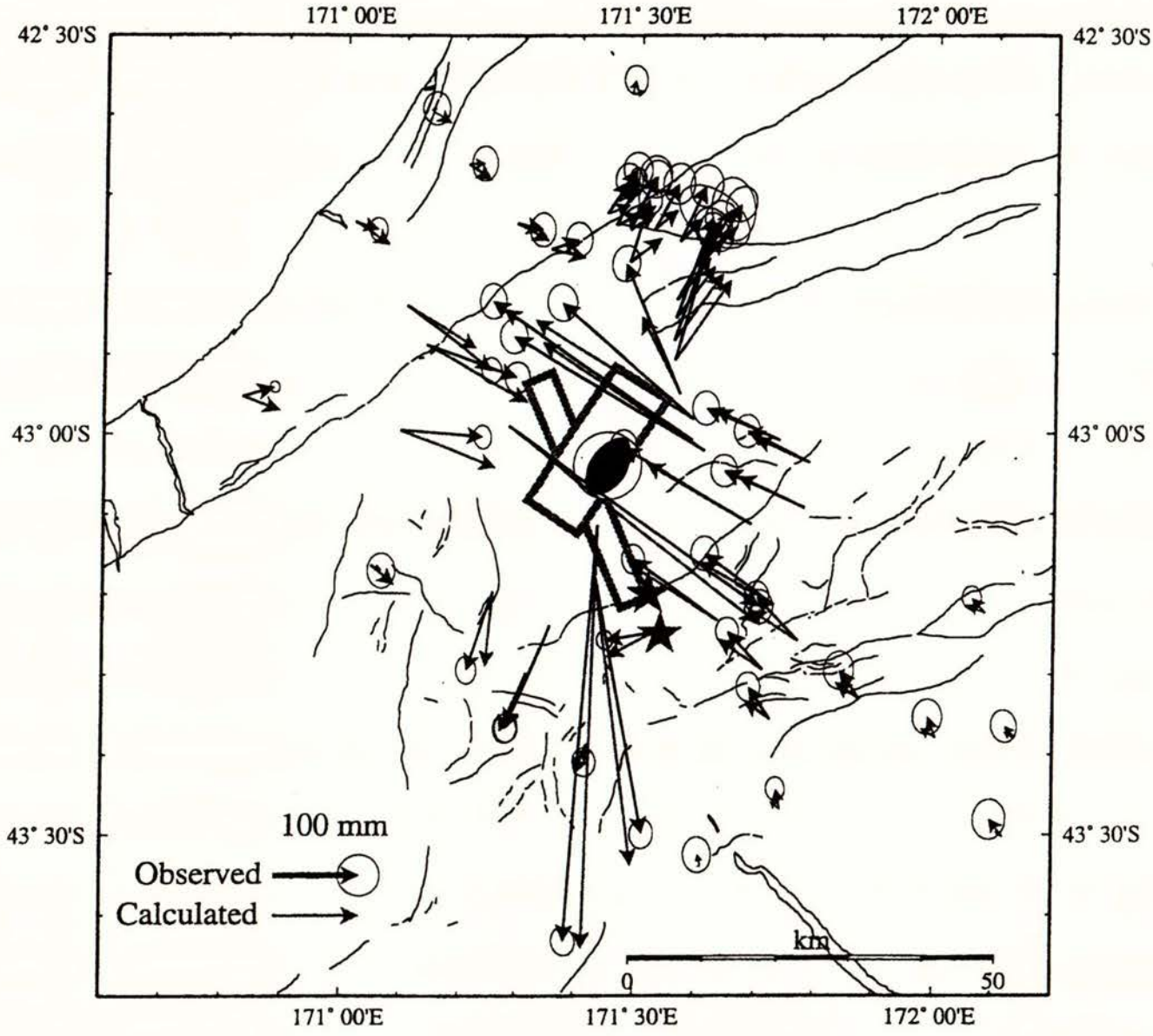

Figure 9

Best Fit Two Fault Model

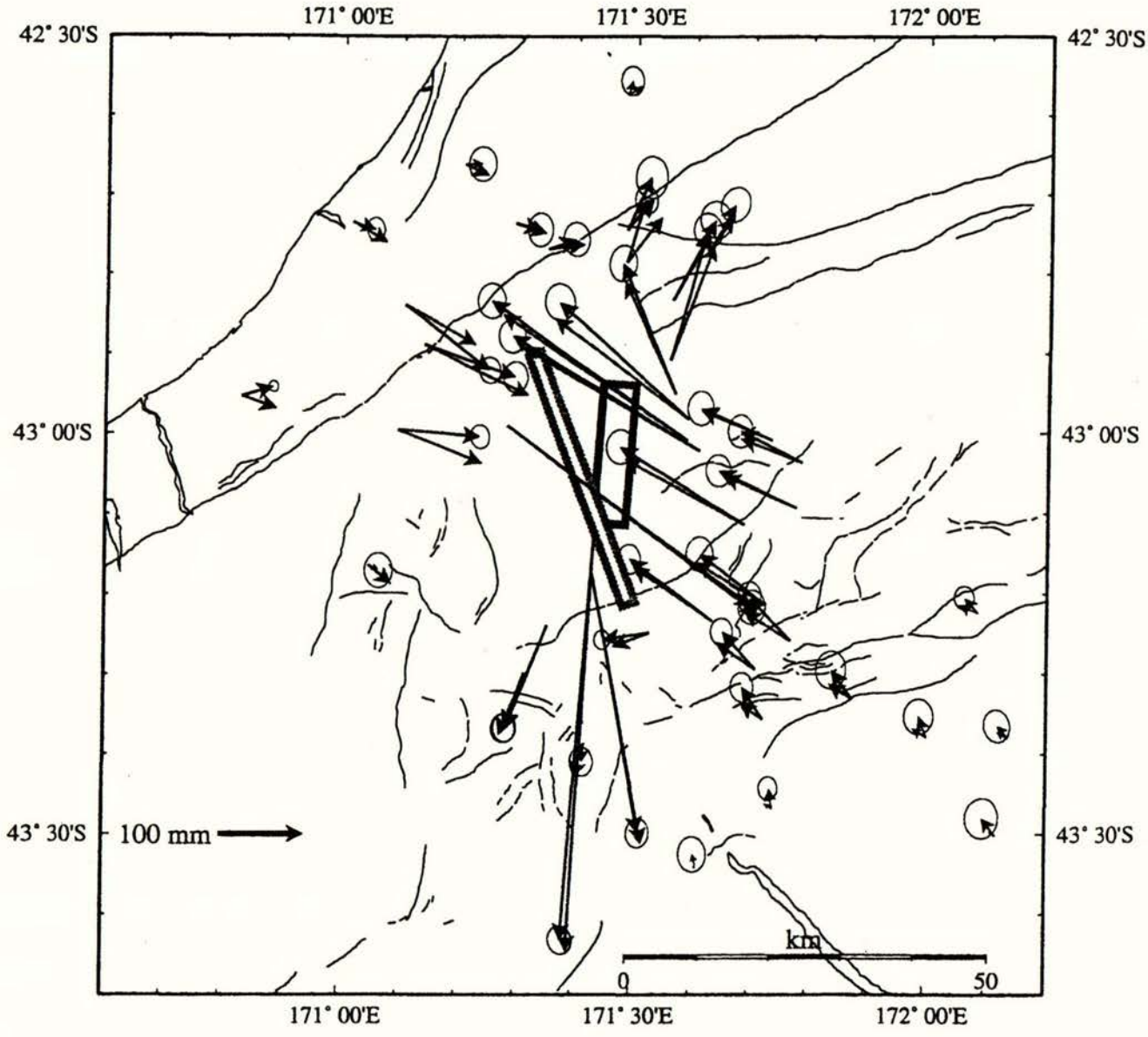

Figure 10

INSTITUTE OF GEOLOGICAL & NUCLEAR SCIENCES LIMITED

Corporate Services
69a Gracefield Road
PO Box 30368
Lower Hutt
New Zealand
Phone +64-4-570 1444
Fax +64-4-569 0600

30 Gracefield Road
PO Box 31 312
Lower Hutt
New Zealand

Phone +64-4-569 0637
Fax +64-4-569 0657

State Insurance Building
Andrews Avenue
PO Box 30 368
Lower Hutt
New Zealand
Phone +64-4-569 9059
Fax +64-4-569 5016

32 Salamanca Road
Kelburn
PO Box 1320
Wellington
New Zealand
Phone +64-4-473 8208
Fax +64-4-471 0977

Wairakei Research Centre
State Highway 1, Wairakei
Private Bag 2000
Taupo
New Zealand
Phone +64-7-374-8211
Fax +64-7-374 8199

Crown Research Dunedin
764 Cumberland Street
Private Bag 1930
Dunedin
New Zealand
Phone +64-3-477 4050
Fax +64-3-477 5232